

ABSTRACT

Title of Document:

NEW MEASURES FOR THE STUDY OF
DISTRIBUTIVE MIXING IN CONTINUOUS
CREEPING FLOWS

Jason Robert Nixon, Master of Science, 2014

Directed By:

Associate Professor David I. Bigio
Department of Mechanical Engineering

New mathematical measures are developed for the investigation of fluid-fluid mixing in continuous laminar flows as a function of mechanisms of mixing, namely the eigenvectors of the rate of deformation tensor. Previous theoretical work in this field has shown that interfacial reorientation and chaotic advection produce improved mixing over deterministic mixing. However, these previous approaches have failed to explore the nature of the mechanisms of mixing present in the continuously spatially varying flow fields.

Four new measures are presented to relate the deformation of an infinitesimal material element to the eigenvectors of the rate of deformation tensor. These expressions characterize material deformation as a function of the spatial relationship between material and the eigenvectors in a variety of general flows. The application of these measures is shown using CFD simulations for three steady flows, the Couette channel, the diverging channel, and the steady state lid driven cavity. These measures improve

the understanding of mixing in the various flow field models and produce new insight into the nature of mixing in continuous flow fields.

NEW MEASURES FOR THE STUDY OF DISTRIBUTIVE
MIXING IN CONTINUOUS CREEPING FLOWS

By

Jason Robert Nixon

Thesis submitted to the Faculty of the Graduate School of the
University of Maryland, College Park, in partial fulfillment
of the requirements for the degree of
Master of Science
2014

Advisory Committee:

Professor David I. Bigio, Chair
Professor Henry W. Haslach Jr.
Professor Amir Raiz

©Copyright by

Jason Robert Nixon

2014

Acknowledgements

I would first like to give my sincerest gratitude and appreciation to my advisor, Dr. Bigio. His guidance, support, and contribution to my development as a scientist throughout my undergraduate and graduate education has proved invaluable. Throughout this experience, I have learned the value of not only doing, but also the value of the completion and acknowledgment of ones accomplishments. I would also like thank my committee members, Dr. Riaz and Dr. Haslach for their contributions to my knowledge as a student and all the work they have done with my on my thesis.

Finally, I would like to thank my family for their endless support throughout my time at the University of Maryland. Without the endless guidance that you've given, I never would have made it through the difficulties of research.

Contents

Acknowledgements	ii
Table of Contents	iii
List of Figures	v
List of Nomenclature	viii
1 Introduction	1
1.1 Motivation	1
1.2 Study	3
1.3 Organization of Thesis	3
2 Background	5
2.1 Mixing	5
2.2 Kinematics	6
2.3 Continuum Mechanics	9
2.4 Chaos	10
3 Theory	13
3.1 Continuum Mechanics	13
3.1.1 Coordinate Descriptions	13
3.1.2 Material Derivative	15
3.1.3 Flow Descriptions	16
3.1.4 Interface Growth	17
3.1.5 Principal Directions of \mathcal{D}	18
3.2 Material Derivative of \mathbf{d}_i	20
3.3 Equilibrium Orientations	23
3.4 Orientation Factor	26
4 Numerical Modeling	32
4.1 Velocity Field Solution Generation	33
4.1.1 Couette Channel	33
4.1.2 Diverging Channel	35
4.1.3 Lid Driven Cavity	37
4.2 Interface Tracking	43
4.2.1 Couette and Diverging Channel	43
4.2.2 Lid Driven Cavity	43
5 Results	46
5.1 Semi-Infinite Couette Channel	46
5.2 Semi-Infinite Diverging Channel	52
5.3 Lid-Driven Cavity	59

5.3.1	Inner Streamline ($y_0 = 0.45$)	63
5.3.2	Outer Streamline ($y_0 = 0.23$)	75
5.3.3	Twirl and Streamline Curvature Fields	85
6	Conclusions	89
6.1	Conclusions	89
6.2	Recommendation for Future Work	93
A	Twirl Tensor Derivation	95
B	Supplementary Figures	98
B.1	Diverging Channel with $\theta \rightarrow \alpha$	98
B.2	Lid Driven Cavity Inner Streamline ($y = 0.23$)	99
B.2.1	Upward Flight	99
B.2.2	Downward Flight	103
B.3	Lid Driven Cavity Outer Streamline ($y = 0.23$)	107
B.3.1	Upward Flight	107
B.3.2	Downward Flight	111
C	Code	115
C.1	Couette Channel	115
C.1.1	Master Code	115
C.1.2	Material Tracking Module	116
C.2	Diverging Channel	117
C.2.1	Master Code	117
C.2.2	Material Tracking Module	119
C.2.3	ODE45 Equation Module	123
C.3	Lid Driven Cavity	123
C.3.1	Master Code	123
C.3.2	Velocity Field Generation Module	126
C.3.3	Material Tracking Module	128
C.3.4	Runge-Kutta Module	132
C.3.5	Streamline Curvature Module	133
	References	134

List of Figures

2.1	Illustration of Distributive and Dispersive Mixing [28]	6
3.1	Lagrangian to Eulerian Coordinate Transformation	15
4.1	Couette Flow Model	34
4.2	Diverging Channel Flow Field Model	35
4.3	Diverging Channel Sample Velocity Profile	37
4.4	High Aspect Ratio Lid Driven Cavity Flow Field Model	38
4.5	Central Finite Difference Stencil (in Nodal Coordinates)	40
4.6	Lid Driven Cavity Centerline Velocity Profile Comparison	43
5.1	Couette Channel First Interface Orientation Factor vs. Time	48
5.2	Couette Channel Second Interface Orientation Factor vs. Time	49
5.3	Couette Channel First Velocity Orientation Factor vs. Time	50
5.4	Couette Channel Second Velocity Orientation Factor vs. Time	51
5.5	Diverging Channel Material Vector Position (Radial) vs. Time	53
5.6	Diverging Channel Material Stretch vs. Time	54
5.7	Diverging Channel First Interface Orientation Factor vs. Time	55
5.8	Diverging Channel Second Interface Orientation Factor vs. Time	56
5.9	Diverging Channel First Velocity Orientation Factor vs. Time	57
5.10	Diverging Channel Second Velocity Orientation Factor vs. Time	59
5.11	Lid Driven Cavity Regions	60
5.12	Lid Driven Cavity Interface Path for $y_0 = 0.45$	63
5.13	Lid Driven Cavity Square Orientation Plot for \mathbf{p} and \mathbf{d}_1 for $y_0 = 0.45$	64
5.14	Lid Driven Cavity Material Stretch for $y_0 = 0.45$	66
5.15	Lid Driven Cavity Normalized Material Stretching Rate for $y_0 = 0.45$	67
5.16	Lid Driven Cavity Maximum Normalized Material Stretching Rate for $y_0 = 0.45$	69
5.17	Lid Driven Cavity First Interface Orientation Factor for $y_0 = 0.45$	70
5.18	Lid Driven Cavity Second Interface Orientation Factor for $y_0 = 0.45$	71
5.19	Lid Driven Cavity First Velocity Orientation Factor for $y_0 = 0.45$	73
5.20	Lid Driven Cavity Second Velocity Orientation Factor for $y_0 = 0.45$	74
5.21	Lid Driven Cavity Interface Path for $y_0 = 0.23$	75
5.22	Lid Driven Cavity Square Orientation Plot for \mathbf{p} and \mathbf{d}_1 for $y_0 = 0.23$	76
5.23	Lid Driven Cavity Material Stretch for $y_0 = 0.23$	78
5.24	Lid Driven Cavity Normalized Material Stretch Rate for $y_0 = 0.23$	79
5.25	Lid Driven Maximum Normalized Material Stretching Rate for $y_0 = 0.23$	80
5.26	Lid Driven Cavity First Interface Orientation Factor for $y_0 = 0.23$	81
5.27	Lid Driven Cavity Second Interface Orientation Factor for $y_0 = 0.23$	83
5.28	Lid Driven Cavity First Velocity Orientation Factor for $y_0 = 0.23$	84
5.29	Lid Driven Cavity Second Velocity Orientation Factor for $y_0 = 0.23$	85
5.30	Lid Driven Cavity Upward Flight Twirl Contour	86
5.31	Lid Driven Cavity Upward Flight Streamline Curvature Contour	87
5.32	Lid Driven Cavity Upward Flight Twirl and Streamline Curvature Comparison	88

B.1	Diverging Channel First Interface Orientation Factor for Streamline Angle $\theta = 4.00^\circ$, $\theta = 4.25^\circ$, $\theta = 4.50^\circ$, and $\theta = 4.75^\circ$	98
B.2	Lid Driven Cavity Upward Flight Square Orientation Plot for \mathbf{p} and \mathbf{d}_1 for $y_0 = 0.45$	99
B.3	Lid Driven Cavity Upward Flight Material Stretch for $y_0 = 0.45$	99
B.4	Lid Driven Cavity Upward Flight Normalized Material Stretch Rate for $y_0 = 0.45$	100
B.5	Lid Driven Cavity Upward Flight Maximum Normalized Material Stretching Rate for $y_0 = 0.45$	100
B.6	Lid Driven Cavity Upward Flight First Interface Orientation Factor for $y_0 = 0.45$	101
B.7	Lid Driven Cavity Upward Flight Second Interface Orientation Factor for $y_0 = 0.45$	101
B.8	Lid Driven Cavity Upward Flight First Velocity Orientation Factor for $y_0 = 0.45$	102
B.9	Lid Driven Cavity Upward Flight Second Velocity Orientation Factor for $y_0 = 0.45$	102
B.10	Lid Driven Cavity Downward Flight Square Orientation Plot for \mathbf{p} and \mathbf{d}_1 for $y_0 = 0.45$	103
B.11	Lid Driven Cavity Downward Flight Material Stretch for $y_0 = 0.45$	103
B.12	Lid Driven Cavity Downward Flight Normalized Material Stretch Rate for $y_0 = 0.45$	104
B.13	Lid Driven Cavity Downward Flight Maximum Normalized Material Stretching Rate for $y_0 = 0.45$	104
B.14	Lid Driven Cavity Downward Flight First Interface Orientation Factor for $y_0 = 0.45$	105
B.15	Lid Driven Cavity Downward Flight Second Interface Orientation Factor for $y_0 = 0.45$	105
B.16	Lid Driven Cavity Downward Flight First Velocity Orientation Factor for $y_0 = 0.45$	106
B.17	Lid Driven Cavity Downward Flight Second Velocity Orientation Factor for $y_0 = 0.45$	106
B.18	Lid Driven Cavity Upward Flight Square Orientation Plot for \mathbf{p} and \mathbf{d}_1 for $y_0 = 0.23$	107
B.19	Lid Driven Cavity Upward Flight Material Stretch for $y_0 = 0.23$	107
B.20	Lid Driven Cavity Upward Flight Normalized Material Stretch Rate for $y_0 = 0.23$	108
B.21	Lid Driven Cavity Upward Flight Maximum Normalized Material Stretching Rate for $y_0 = 0.23$	108
B.22	Lid Driven Cavity Upward Flight First Interface Orientation Factor for $y_0 = 0.23$	109
B.23	Lid Driven Cavity Upward Flight Second Interface Orientation Factor for $y_0 = 0.23$	109
B.24	Lid Driven Cavity Upward Flight First Velocity Orientation Factor for $y_0 = 0.23$	110

B.25 Lid Driven Cavity Upward Flight Second Velocity Orientation Factor for $y_0 = 0.23$	110
B.26 Lid Driven Cavity Downward Flight Square Orientation Plot for \mathbf{p} and \mathbf{d}_1 for $y_0 = 0.23$	111
B.27 Lid Driven Cavity Downward Flight Material Stretch for $y_0 = 0.23$. .	111
B.28 Lid Driven Cavity Downward Flight Normalized Material Stretch Rate for $y_0 = 0.23$	112
B.29 Lid Driven Cavity Downward Flight Maximum Normalized Material Stretching Rate for $y_0 = 0.23$	112
B.30 Lid Driven Cavity Downward Flight First Interface Orientation Factor for $y_0 = 0.23$	113
B.31 Lid Driven Cavity Downward Flight Second Interface Orientation Fac- tor for $y_0 = 0.23$	113
B.32 Lid Driven Cavity Downward Flight First Velocity Orientation Factor for $y_0 = 0.23$	114
B.33 Lid Driven Cavity Downward Flight Second Velocity Orientation Fac- tor for $y_0 = 0.23$	114

Nomenclature

Notes of general nomenclature.

- Non-bolded, non-calligraphic characters denote scalar-valued parameters.
- Bolded, non-calligraphic characters denote vector-valued parameters.
- Calligraphic characters denote tensor-valued parameters.
- Uppercase characters denote parameters in the Lagrangian configuration.
- Lowercase characters denote parameters in the Eulerian configuration. (See section 3.1.1)
- Characters with an overhead dot (\dot{a} , $\dot{\mathbf{a}}$, $\dot{\mathcal{A}}$) denote the material derivative of that parameter, as defined in (3.1.3), (3.1.4), and (3.1.5). Likewise, (\ddot{a} , $\ddot{\mathbf{a}}$, $\ddot{\mathcal{A}}$) denote the second material derivative of a parameter.
- Characters followed by a superscript prime symbol (\mathbf{a}' , \mathcal{A}') denote parameters which have undergone a coordinate rotation.

A	-	An interfacial area
A_i	-	The initial interfacial area
A_f	-	The final interfacial area
A_R	-	Lid driven cavity aspect ratio
\mathbf{d}_i	-	Eigenvectors (principal directions) of \mathcal{D}
ds	-	An infinitesimal material vector magnitude (Eulerian)
dS	-	An infinitesimal material vector magnitude (Lagrangian)
$d\mathbf{x}$	-	An infinitesimal material vector (Eulerian)
$d\mathbf{X}$	-	An infinitesimal material vector (Lagrangian)
\mathcal{D}	-	The rate of deformation tensor
\mathcal{D}'	-	\mathcal{D} in its principal orientation
e_L	-	Mixing efficiency measure (Ottino et. al.)
F	-	Scaled radial velocity term (diverging channel)
\mathcal{F}	-	Deformation tensor
G	-	Non-dimensional radial velocity term (diverging channel)
h_0	-	Initial starting height
H_0	-	Channel height
\mathcal{I}	-	The identity tensor
\mathcal{L}	-	The gradient of \mathbf{u}
O_p	-	First interface orientation factor
\dot{O}_p	-	Second interface orientation factor
O_u	-	First velocity orientation factor
\dot{O}_u	-	Second velocity orientation factor
O	-	First orientation factor
\dot{O}	-	Second orientation factor

- \boldsymbol{p} - An infinitesimal unit material vector
- R - An numerical over-relaxation parameter
- Re - Reynolds number
- \mathcal{T} - The twirl tensor
- \mathcal{W} - The vorticity tensor
- \boldsymbol{u} - A fluid velocity field
- U_0 - Characteristic boundary velocity
- α - The diverging channel divergence angle
- γ - Shear
- $\dot{\gamma}$ - Shearing rate
- $\dot{\epsilon}$ - Maximum normalized stretching Rate
- $\ddot{\epsilon}$ - Rate of change of the maximum normalized stretching rate
- η_L - Infinitesimal line stretching efficiency
- λ_i - Eigenvalues (principal values) of \mathcal{D}
- μ - Dynamic fluid viscosity
- ν - Kinematic fluid viscosity
- ξ - Normalized material stretching rate
- ρ - Fluid density

Chapter 1: Introduction

1.1 Motivation

Descriptions of high viscosity fluid-fluid mixing have gone through several evolutions, beginning with early Lagrangian kinematical studies and later with application of continuum mechanics principles. Due to viscous considerations, flow is constrained to the laminar regime. Most recently, chaotic mixing techniques have been introduced to achieve a greater degree of mixing than previously possible in the laminar regime. Movement of fluid elements in laminar flow is along streamlines. The most efficient types of mixing induce controlled fluid-fluid interface reorientation along streamlines, thereby enhancing interface growth rates. Alternatively, they induce streamline hopping, which produces similar enhancements in growth rate by a different mechanism. These phenomena have led to a number of different mixing machine designs including batch mixers, single-screw extruders and twin-screw extruders, all of which attempt to fluid elements both in the field and with respect to the field. In industry, the analysis of mixing regard mixing machines as black boxes. Mixing in these black boxes is usually described by the observable output, which can be expressed with bulk material properties or material property distribution. While this is suited to these types of machines due to difficulty of actively sampling local mixing mid-process, the actual physics of the mixing in time remain unexplored. Indeed, industry has generally relied on trial and error in the generation of new mixing geometries and process.

In distributive laminar mixing, chaotic or not, improvements to mixing are achieved by repeatedly altering the relationship between the fluid-fluid interface and the velocity field in order to maximize interface deformation. In early experiments focused on exploring this phenomenon, reorientation was artificially induced by cutting, rotating, and replacing these interface elements by hand. In this case, reorientation is a discrete phenomenon, and the mechanisms leading to improved interface stretching

in continuous flow fields are effectively hidden. Recently, with the development of easily available, high capability, and relatively low cost computing systems, scientists and engineers have been able to calculate velocity fields for a wide variety of mixing domains, allowing for the exploration of fluid transport phenomena without the use of complicated and costly laboratory experiments. However, the ability to generate mixing domain velocity fields does not guarantee an understanding of mixing, and therefore more investigation is required. Indeed, a combination of the kinematical approach (which is rooted in the Lagrangian specification) and the continuum mechanics approach is needed to fully explore mixing. Using the continuum mechanics approach, velocity fields and relevant mixing related properties can be calculated for the mixing domain. However, the application of continuum mechanics does not lend itself easily to the study of the deformation of material particles in the Eulerian domain. Therefore, a combination of these approaches for the study of mixing must be used to explore mixing in complex continuous domains.

In this work, the objective was to develop new measures to be applied to the general continuous laminar mixing domain to examine mixing and mixing potential as a function of properties of the underlying velocity field. Further, the work centered mixing on the study of the rate-of-deformation tensor, a commonly used velocity field for the description of the local deformation of a material interface in a fluid field. Furthermore, the comparison of mixing utilized the most relevant coordinate system, the rate-of-deformation tensor eigenvectors (also denoted as the principal directions). These measures were applied to a number of flow fields including pure shear, pure extensional, mixed shear-extensional, and in spatially variant flows (defined as any region in the velocity field where the rate-of-deformation tensor material derivative is non-zero).

1.2 Study

This study sought to derive new measures for the study of distributive laminar mixing. The derivation and demonstration of these measures was done with several goals in mind.

- Derive new measures incorporating the effects of changes in fluid interface relative to the flow field as, well as changes in eigenvectors of the rate of deformation tensor \mathcal{D} into the study of interfacial reorientation in distributive laminar mixing.
- Relate these new measures to existing mixing measures to demonstrate that existing and new knowledge could be gained from their application.
- Apply these measures to a series of 2D flow field models to explore their effectiveness in identifying flow field characteristics for optimum mixing.
- Identify any new phenomenon that were illuminated through the application of these measures.

1.3 Organization of Thesis

This thesis is presented in six chapters. Chapter 2 presents a semi-chronological review of the background literature on laminar mixing theory, including developments in the kinematic study of flow, the application of continuum mechanics to flow studies, and developments in chaotic flows.

Chapter 3 begins with a review of continuum mechanics, which will serve as the foundation for the theoretical analysis of mixing in this work, with a special focus on the eigenvalue/eigenvector decomposition of the rate-of-deformation tensor \mathcal{D} as well as measures of mixing which have been derived by other authors. Following this, theoretical development for the twirl tensor \mathcal{T} and orientation factors will be discussed. These parameters are the main theoretical contribution of this work.

Chapter 4 presents the flow field models used to demonstrate the functionality of the newly derived measures in the idealized flow field models. Procedures used for attaining velocity field solutions are discussed. Fluid-fluid interface tracking within the flow field domains is also discussed.

Chapter 5 reports on the application of the new measures applied to fundamental stretching regimes. Interface stretching, stretching rate, orientation, principal direction orientation, velocity orientation, swirl magnitude, first interface/velocity orientation factor, and second interface/velocity orientation factor are studied in these flow field models.

Chapter 6 summarizes conclusions drawn from the theoretical and numerical work in previous chapters. A discussion is presented on the effectiveness of these new theoretical measures for describing distributive laminar mixing and possible future directions for this work.

Chapter 2: Background

This chapter presents a semi-chronological development of the measurement and characterization of distributive mixing. First, definitions for mixing are presented, followed by the developments for kinematical measures of mixing and a brief review of the contributions of continuum mechanics to mixing. A more detailed exploration of continuum mechanics follows in Chapter 3. Finally, a discussion on chaotic advection in mixing, which has proven to be the most effective type of mixing in the laminar flow regime, is discussed.

2.1 Mixing

Tadmor and Gogos present a good description of the two mixing types in *Principles of Polymer Mixing* [28]. The first type of mixing, termed distributive (also laminar- or extensive-) mixing, refers to mixing accomplished by the spatial distribution of a minor component into a major, both of which lack cohesive character. Ideal mixing in the distributive type leads to a homogeneous spatial distribution of the minor component (in this case a fluid with equivalent properties to the major component) in the major component to scales at which molecular diffusion has relevance. The second type of mixing, termed dispersive (or intensive) mixing, involves the reduction in size of the minor component immersed in the major component. In dispersive mixing, the shared boundary between major and minor components has cohesive character. Cohesive character arises in the mixing of solid agglomerates, non-compatible fluid species, and gaseous bubbles in the major component. The cohesive character take the form of van der Waals forces, elastic properties, or surface tensions. Furthermore, while the mechanisms for distributive and dispersive mixing differ, the end result of both types converges to the complete homogenous spatial distribution of the smallest possible units of the minor component in the major component.

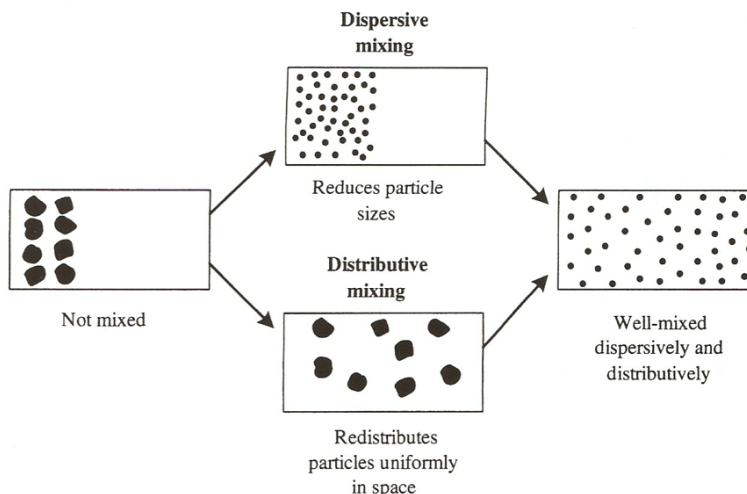


Figure 2.1: Illustration of Distributive and Dispersive Mixing [28]

2.2 Kinematics

The core of this study focuses exclusively on distributive mixing. Descriptions and characterization schemes for the quality of distributive mixing have been proposed by a number of authors. The first author to do this for distributive mixing was Brothman [3], who recognized the relationship between the area shared between two immiscible fluid species and the quality of mixing. Spencer and Wiley [27] then advanced this model to a two-parameter metric based on the shared intermaterial (interface area) area between fluid components as well as the the distribution of the intermaterial area in the mixing domain. An alternate approach proposed by Danckwerts [7] classifies distributive growth with a related two-parameter metric based on the intensity of segregation and the scale of segregation. The former parameter, the intensity of segregation, is a measure of the deviance of local volumetric ratio of major and minor components to the global volumetric ratio. The latter parameter, the scale of segregation, is a measure of the striation thickness, which is inversely related to intermaterial area. In both cases, both a measure of the shared area and distribution of the area play critical roles in expressing mixing quality. These measures retain significance

in a variety of mixing fields including both deterministic and chaotic mixing and are therefore the preferred definition for mixing in this work.

Early kinematical descriptions of mixing were proposed by Spencer and Wiley [27] and later by Lewis Erwin. The first studies of laminar flow were based on interface area growth in simple shear. Spencer and Wiley considered the deformation of an interface element in simple shear. As stated before, the improvement in mixing depended on the creation of interface area and the improvement of the area distribution of the mixing domain. In this study, Spencer and Wiley found interfacial area growth to be a function of the magnitude of the shearing rate and the initial orientation of the interface. It was determined that in a deterministic flow field (a mixing domain in which deformation can be exactly calculated at any time with an initial state), knowledge of the initial state and shearing rate is sufficient to exactly calculate the deformed state at any time t later. Spencer and Wiley found a simple expression for area growth under strain:

$$\frac{A}{A_i} = \sqrt{1 - 2(\dot{\gamma}t) n_1 n_2 + (\dot{\gamma}t)^2 n_1^2} \quad (2.2.1)$$

where final interfacial area A is a function of initial area A_i , strain rate $\dot{\gamma}$, imparted strain $\dot{\gamma}t$, and the normal area orientation $\mathbf{n} = \{n_1, n_2, n_3\}$. In general, for mixing processes involving polymers or other high viscosity fluids, high imparted shear γ is preferred to improve the generation and distribution of intermaterial area. Under these conditions (2.2.1) reduces to:

$$\frac{A}{A_i} = (\dot{\gamma}t) n_1 \quad (2.2.2)$$

Equation (2.2.2) shows that intermaterial area growth in simple shear flow is approximately linear with respect to time t for large imparted strain $\dot{\gamma}t$, resulting in a linear relationship between imparted shear and interface area growth. For a period of about 25 years, the field of mixing assumed that material stretching was

limited by the imparted shear. Therefore, the task of an engineer was to improve $\dot{\gamma}t$ by seeking higher shear rates $\dot{\gamma}$ to keep production time and mixer size reasonable. Mohr, Saxson, and Jepson published several papers on the topic of high viscosity mixing using simple shear [18, 19]. While Spencer and Wiley were able to calculate exactly interface growth in simple shear, most other types of flow become quickly intractable, and only with the advent of high power computational fluid dynamics has the analytical calculation of mixing parameters in these domains become possible.

Later, in the late 1970's, Lewis Erwin [10] defined an upper bound for the increase in the length of an interface in shear flow for large deformations and showed the importance of the orientation of the interface with respect to the principal directions of the deformation tensor [8]. In this work, Erwin derived an equation for the growth of interface surface area with respect to an arbitrary three-dimensional local shear of finite magnitude.

$$\frac{A_f}{A_i} = \sqrt{\frac{\cos^2 \beta_1}{\lambda_1^2} + \frac{\cos^2 \beta_2}{\lambda_2^2} + \frac{\cos^2 \beta_3}{\lambda_3^2}} \quad (2.2.3)$$

where the direction cosine terms $\cos^2 \beta_i$ represent the relative projection between the components of the vector normal to the material area and the principal directions of the strain tensor, and λ terms represent the magnitude of the principal extension ratios (eigenvalues of the rate of deformation tensor), a function of the local shear. The most intriguing result of this work showed that a mixer which optimized interface orientation with respect to the principal triad at all times would impart maximum possible interface growth, and that this growth would exhibit an exponential rate, the bounding rate for streamline mixing. He went on to explore several classes of flow including shear flow, pure extensional flow, and plane extensional flow, and found that in the case of pure extension, interface stretching was maximized, although in practice these stretching rates can rarely be realized. Erwin [9] also explored the effect of forced interfacial reorientation relative to a fixed shear flow. This experiment revealed that the ratio of the area A to initial area A_i was a function of both shearing

rate $\dot{\gamma}$ and the number of reorientations N .

$$\frac{A}{A_i} = \left[\frac{\dot{\gamma}t}{N} \right]^N \quad (2.2.4)$$

Furthermore, in extensional flows, with a large number of reorientations and good choice in initial orientation, the growth rate of the interface can asymptotically approach an exponential value, resulting in a higher than linear rate typically found in shear flows. This property is the reason for the paddles, fins, vanes, etc. in batch mixers and the various geometries of mixing elements found in ram-type extruders.

Many interfacial growth measurement schemes rely on the kinematical approach to measure mixing by the study of the interface growth history with respect to time. While this technique can describe changes in fluid interfaces in time, it fails to explore the underlying mechanisms that induce these deformations. Ultimately this technique is limited in its ability to explain observed mixing phenomenon and cannot be effectively used for the generation of new mixing geometries.

2.3 Continuum Mechanics

Ottino, Ranz and Macasko [23, 24] proposed the first application of continuum mechanics to describe fluid-fluid mixing. This framework provides the mathematical foundation necessary to describe the mechanisms by which fluid deformation is induced. A more complete description of continuum mechanics is introduced in Chapter 3. In the continuum mechanics framework, Ottino, Ranz, and Macasko derived an expression for mixing efficiency e_L by noting an upper bound on the instantaneous normalized rate of stretching of the rate of deformation tensor \mathcal{D} and the unit interface orientation vector \mathbf{m} .

$$\xi = \frac{d\dot{s}}{ds} = \mathbf{m} \cdot \mathcal{D} \cdot \mathbf{m} \leq \sqrt{\mathcal{D} : \mathcal{D}} \quad (2.3.1)$$

The mixing efficiency e_L is therefore a ratio of the instantaneous normalized

stretching rate to the maximum instantaneous normalized stretching rate.

$$e_L = \frac{\xi}{\sqrt{\mathcal{D} : \mathcal{D}}} \quad (2.3.2)$$

This measure of the efficiency of mixing was used by Ottino and Chella [4, 5, 20] to evaluate different classes of cavity flow.

With the development of powerful numerical techniques and computing hardware, the study of mixing with numerical simulation using computation fluid dynamics (CFD) produced a number of insights into fluid deformation in flows otherwise unachievable by experimental means. Furthermore, numerical modeling of mixing processes has provided a low cost and time efficient method for exploring the effects of design and processing conditions on mixing performance without the need for complex experimental setups. However, while the numerical domain may allow improvement over "guess and check" methods, there are still limitations on accuracy and the potential for computational artifacts generated that must be considered when using CFD.

2.4 Chaos

The concept of chaotic mixing was introduced by Hassan Aref [1]. In his 1984 publication, Aref reports on complex stretching patterns leading to greater than expected mixing using two co-rotating periodically blinking vortices (or more formally a piecewise-constant stirring motion) in a circular cavity. In this experiment, the flow field was assumed to be steady state at all times. The fluid was assumed to instantaneously achieved state during vortex switching. Aref found that in this flow field model, the phenomenon denoted chaotic advection, produced a stochastic response in the Lagrangian sense through discontinuous growth resulting from the streamline hopping that occurs during vortex switching for certain combinations of vortex blinking frequency and vortex amplitude. Vortex switching refers to the periodic

activation/de-activation of the two vortices in the flow. Spencer and Wiley had previously described this chaotic quality as a result of a randomizing factor, which changed an arbitrary fluid parcel configuring with respect to the streamlines, that can produce greater mixing than typically found in deterministic mixing.

Chien, Rising, and Ottino [6] went on to examine chaotic mixing of lines and area elements in several classes of cavity flow. (These types of cavity flows were previously studied by Chella and Ottino [5].) In their work, the authors presented an experimental apparatus to produce approximately 2D cavity flow driven by wall motion over a range of Reynolds numbers and cavity aspect ratios for steady and periodic flows. They experimented with a number of steady flows (single moving wall (Type I), two opposing walls moving with same velocities (Type II), two opposing walls with opposite velocities (Type III)) and found three distinct streamline patterns. A fourth condition was also explored that had alternating motion on two opposing walls, which was verified to produce chaotic advection. Again, chaotic deformation was found to be very sensitive to the frequency of wall velocity reversal, wall velocity amplitude, material location and orientation, and cavity geometry. Ultimately, it was found that periodic cavity flow ($f > 0$) was a more efficient mixer than steady cavity flows ($f = 0$). Leong and Ottino [15] went on to develop an experimental apparatus to physically demonstrate these cavity flows.

Ottino [20] in particular found that all 2D chaotic mixers involved two building blocks, hyperbolic points and elliptic points. In flow, fluid elements are attracted towards hyperbolic point when approaching from one direction and repelled when approaching from another direction. Fluid elements circulate about elliptic points. Using these building blocks, all two dimensional chaotic flow can be characterized. Movement of fluid parcels in fluid flows with these points is the indicator of chaos. For example, in an arbitrary velocity field configuration, the fluid parcel will have a trajectory towards, away, or rotating about a point, and have a completely different

trajectory in a different velocity field configuration due to changes in the periodic conditions, leading to chaotic advection. Ottino [21] provides a comprehensive review of chaos and the connections to turbulent mixing.

Chapter 3: Theory

3.1 Continuum Mechanics

In previous works, the understanding of mixing has been progressed in two ways, first from the kinematical description and later with the application of continuum mechanics. The kinematical approach for the description of mixing, discussed in more detail in Chapter 2, defines material stretching as a function of the stretching history of a Lagrangian particle. The latter approach applies continuum mechanics principles to explore the mechanisms of mixing using Eulerian flow field properties, which can be used to quantify how and why mixing is occurring but cannot easily describe the mixing itself. This approach has become increasingly popular with the development of computational fluid dynamics (CFD) techniques. In this work, the analysis of mixing is conducted using the principal directions (or more formally the eigenvectors) of relevant continuum mechanics parameters and how these mechanisms act on a intermaterial interface in the flow. First, a framework will be presented on the parameters and definitions for the continuum mechanics used in this work. Next, the expression and meaning for the new parameter "twirl" will be introduced. Finally, new measures are derived for expressing material deformation in a continuous flow field.

The continuum mechanics principles used follow those given in *Nonlinear Solid Mechanics: A Continuum Approach for Engineering* [14], *Introduction to the Mechanics of a Continuous Media* [16], *Mixing and Compounding of Polymers* [17], and *Incompressible Flow* [25].

3.1.1 Coordinate Descriptions

Within fluid mechanics, a continuum of fluid can be described using a number of different coordinate systems. In this thesis, only two coordinate systems will be used.

The first coordinate system is the Eulerian description, which describes fluid motion in space and time relative to a origin at an arbitrary spatial position. All other positions are described relative to that position by the vector \mathbf{x} and time t , where $\mathbf{x} = \{x_1, x_2, x_3\}$. The second coordinate system of interest is the Lagrangian system. This coordinate system fixes a coordinate system to an arbitrary particle moving in the continuum and describes all other positions relative to this reference state by the vector \mathbf{X} and time t , where $\mathbf{X} = \{X_1, X_2, X_3\}$. In general, lower case characters refer to parameters in the Eulerian description and upper case characters refer to parameters in the Lagrangian description. An analogy to relate these coordinate systems is to imagine oneself at a theme park, an observer waiting in line watching a roller coaster is in the Eulerian coordinate description whereas an observer on the roller coaster looking out is in the Lagrangian coordinate description.

Because both Eulerian and Lagrangian coordinate systems are in the same continuum, it is necessary to relate one to the other in order to relate properties described in the Eulerian system to a particular particle in the Lagrangian system. If both coordinate systems are of the cartesian type, then they can be related as follows:

$$d\mathbf{x} = \mathcal{F} \cdot d\mathbf{X} \tag{3.1.1}$$

Choose \mathbf{X} to represent the initial (or undeformed) Lagrangian coordinate at $t_0 = 0$, then the deformation gradient tensor \mathcal{F} transforms the material vector $d\mathbf{X}$ into a deformed spatial vector $d\mathbf{x}$ at some later time ($t > 0$) at the Eulerian coordinate \mathbf{x} . Conversely, this expression can be rewritten to express the transformation from the deformed state $d\mathbf{x}$ to the undeformed state $d\mathbf{X}$ as follows:

$$d\mathbf{X} = \mathcal{F}^{-1} \cdot d\mathbf{x} \tag{3.1.2}$$

Figure 3.1 is a representation of the transformation from the undeformed Lagrangian state $d\mathbf{X}(\mathbf{X}, t_0)$ to the deformed Eulerian state $d\mathbf{x}(\mathbf{x}, t_0 + \Delta t)$.

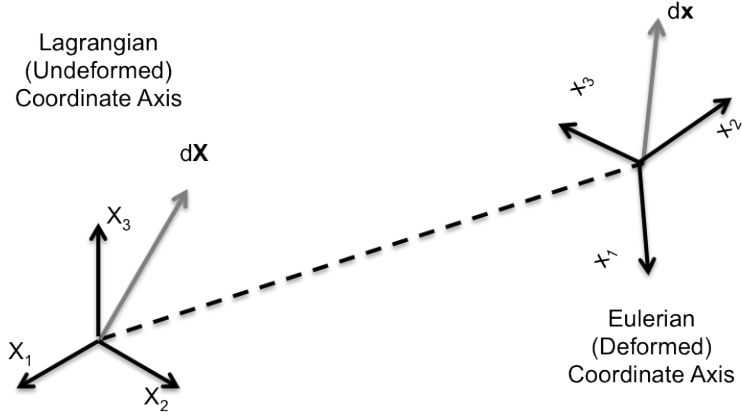


Figure 3.1: Lagrangian to Eulerian Coordinate Transformation

3.1.2 Material Derivative

Depending on the coordinate system used in the definition of a given parameter, it is preferred to perform some operations in the Lagrangian configuration, while for others, in the Eulerian configuration. An operation used extensively in future discussion is the material derivative of a spatial quantity. This operation relates the material and local time derivatives. The material derivative, for a Eulerian scalar-valued parameter a , vector-valued parameter \mathbf{a} , and tensor-valued parameter \mathcal{A} are defined as follows:

$$\dot{a} = \frac{Da}{Dt} = \frac{\partial a}{\partial t} + (\mathbf{u} \cdot \nabla) a \quad (3.1.3)$$

$$\dot{\mathbf{a}} = \frac{D\mathbf{a}}{Dt} = \frac{\partial \mathbf{a}}{\partial t} + (\mathbf{u} \cdot \nabla) \mathbf{a} \quad (3.1.4)$$

$$\dot{\mathcal{A}} = \frac{D\mathcal{A}}{Dt} = \frac{\partial \mathcal{A}}{\partial t} + (\mathbf{u} \cdot \nabla) \mathcal{A} \quad (3.1.5)$$

Note that $(\mathbf{u} \cdot \nabla) \mathbf{a}$ is a vector and $(\mathbf{u} \cdot \nabla) \mathcal{A}$ is a tensor because the operator $\mathbf{u} \cdot \nabla$ is scalar and operates on each terms of \mathbf{a} and \mathcal{A} independently.

3.1.3 Flow Descriptions

In general, it is easier to express a fluid velocity field in the Eulerian system rather than the Lagrangian system. An example is the velocity fields obtained through solutions to the Navier-Stokes equations which is a function of the spatial velocity field $\mathbf{u} = \mathbf{u}(\mathbf{x}, t)$, where $\mathbf{u} = \{u_1, u_2, u_3\}$.

Furthermore, while the velocity field \mathbf{u} is sufficient to describe the movement of a fluid parcel in a flow domain, it is not sufficient on its own to describe the local deformation of that fluid parcel. To express the mechanisms for local fluid deformation, the local gradient of the velocity is also needed. This is expressed using the velocity gradient tensor \mathcal{L} , which is defined as follows:

$$\mathcal{L} = \nabla \otimes \mathbf{u} \quad (3.1.6)$$

The velocity gradient tensor can be decomposed into the sum of its symmetric and skew-symmetric components, the rate of deformation tensor \mathcal{D} (also known as the strain rate tensor or strain tensor) and the vorticity tensor \mathcal{W} (also known as the rotation tensor) respectively.

$$\mathcal{L} = \mathcal{D} + \mathcal{W} \quad (3.1.7)$$

The rate of deformation tensor \mathcal{D} is the mechanism for deformation and stretching. The vorticity tensor \mathcal{W} is the mechanism for rotation. Formally, \mathcal{D} and \mathcal{W} are expressed as:

$$\mathcal{D} = \frac{\mathcal{L} + \mathcal{L}^T}{2} \quad (3.1.8)$$

$$\mathcal{W} = \frac{\mathcal{L} - \mathcal{L}^T}{2} \quad (3.1.9)$$

In the 2D case, the form of the rate of deformation tensor \mathcal{D} can be simplified using dilatation. Dilatation e is equivalently zero for all flows because fluids are considered to be incompressible. Using the definition provided by Malvern, $e \equiv \text{tr}(\mathcal{D})$. Under incompressibility, the on-diagonal elements (also known as the unit strains) of \mathcal{D} are

found to be related by $\mathcal{D}_{11} = -\mathcal{D}_{22}$. By the definition of the rate of deformation tensor \mathcal{D} , the off diagonal terms (also known as the shear strains) are related by $\mathcal{D}_{12} = \mathcal{D}_{21}$.

3.1.4 Interface Growth

The growth of a fluid-fluid interface is approximated using an infinitesimal element of the interface represented by the material vector $d\mathbf{x} = ds\mathbf{p}$ which is locally tangent to the fluid-fluid interface at all points along the interface. ds and \mathbf{p} are the magnitude and unit orientation of $d\mathbf{x}$ respectively. The square rate of change of the length can be described as follows:

$$\frac{d}{dt}(ds^2) = 2d\mathbf{x} \cdot \mathcal{D} \cdot d\mathbf{x} \quad (3.1.10)$$

This can be expressed in the alternate form:

$$\xi = \frac{d\dot{s}}{ds} = \mathbf{p} \cdot \mathcal{D} \cdot \mathbf{p} \quad (3.1.11)$$

Note that ξ is the interface stretching rate scaled by the interface stretch. It is important to note that this expression is valid only for small deformations. In the interest of improving mixing by increasing stretch, it is potentially better to express stretching in Lagrangian coordinate description. Said differently, the Lagrangian description expresses the deformation history of a fluid parcel while the Eulerian description expresses the strain history of a local region. However, the assumption is made that $d\mathbf{x}$ is infinitesimally small, such that even under a large stretch ds , the interface is still infinitesimally small and only dependent on the local strain conditions.

The material derivative of the material vector $d\mathbf{x}$ is:

$$d\dot{\mathbf{x}} = (\mathcal{D} + \mathcal{W}) \cdot d\mathbf{x} \quad (3.1.12)$$

The material derivative of the unit material vector \mathbf{p} is:

$$\dot{\mathbf{p}} = (\mathcal{D} + \mathcal{W}) \cdot \mathbf{p} - \frac{d\dot{s}}{ds} \mathbf{p} \quad (3.1.13)$$

Note that temporal derivatives of $d\mathbf{x}$ and \mathbf{p} in (3.1.12) and (3.1.13) are not included because of the steady state assumption. While the fluid can still accelerate spatially, the fluid velocity at a particular point does not change with respect to time. In future work using transient flow field models, the inclusion of temporally dependent terms is necessary.

3.1.5 Principal Directions of \mathcal{D}

As stated before, the rate of deformation tensor is the means of describing for stretching and deformation in a fluid. Since \mathcal{D} is a 3D, symmetric, real valued tensor, it possess three real valued eigenvalue/eigenvector pairs, also known as the principal values and principal directions. λ_i are the eigenvalues of \mathcal{D} , and \mathbf{d}_i are the corresponding eigenvectors. These eigenvector-eigenvalue pairs are defined by the following definition:

$$\mathcal{D} \cdot \mathbf{d}_i = \lambda_i \mathbf{d}_i \quad (3.1.14)$$

Note that eigenvalues λ_1 , λ_2 , and λ_3 and corresponding eigenvectors \mathbf{d}_1 , \mathbf{d}_2 , and \mathbf{d}_3 are ordered from largest to smallest ($\lambda_1 > \lambda_2 > \lambda_3$). After solving for the eigenvalue-vector pairs using (3.1.14), the rate of deformation tensor can be diagonalized using a rotation tensor \mathcal{A} composed of the three eigenvectors such that $\mathcal{A} = \{\mathbf{d}_1, \mathbf{d}_2, \mathbf{d}_3\}$. Rotation of the rate of deformation tensor \mathcal{D} by the rotation tensor \mathcal{A} yields:

$$\mathcal{D}' = \mathcal{A}^{-1} \cdot \mathcal{D} \cdot \mathcal{A} \quad (3.1.15)$$

Since \mathcal{D} is real and symmetric, \mathcal{D}' will be diagonal with elements equal to the

three eigenvalues in the principal coordinates.

$$\mathcal{D}' = \begin{bmatrix} \lambda_1 & 0 & 0 \\ 0 & \lambda_2 & 0 \\ 0 & 0 & \lambda_3 \end{bmatrix} \quad (3.1.16)$$

Under this configuration, interface stretching will resemble extensional stretching. In the extensional stretching regime, any interface parallel to one of the eigenvector experiences the greatest amount of growth (at an exponential rate) relative to other nearby orientations. As a result of the ordering of eigenvector values, an interface parallel to \mathbf{d}_1 grows at a larger rate than \mathbf{d}_2 will grows at a greater rate than \mathbf{d}_3 . All other orientations experience a stretch rate between zero and exponential. [10]

The incompressible continuity equation ($\nabla \cdot \mathbf{u} = 0$), implicitly states that the summation of eigenvalues must be zero.

$$\lambda_1 + \lambda_2 + \lambda_3 = 0 \quad (3.1.17)$$

At this point, special consideration will be given to the 2D case. In 2D, the third eigenvalue and its corresponding eigenvector are $\lambda_3 = 0$ and $\mathbf{d}_3 = \{0, 0, 0\}$. In the 2D case, (3.1.17) proves to be very useful. Application of the conversation of mass relationship using (3.1.17) reveals that $\lambda_1 = -\lambda_2$. In this case, we find that the normalized stretching rate is bounded between $\lambda_1 < \xi < \lambda_2$. Furthermore, the maximum stretching rate $\dot{\epsilon}$, which is equivalent to λ_1 , is a function of the magnitude of \mathcal{D} .

$$\dot{\epsilon} = \sqrt{\frac{\mathcal{D} : \mathcal{D}}{2}} \quad (3.1.18)$$

Returning to the generalized 3D case, the normalized rate of infinitesimal line growth ξ , given in (3.1.11), is shown to be bounded by the Cauchy-Schwartz inequality.

$$\xi = \frac{d\dot{s}}{ds} \leq \sqrt{\mathcal{D} : \mathcal{D}} \quad (3.1.19)$$

Maximum material vector stretching ($\xi = \lambda_1$) occurs when the vector is parallel to \mathbf{d}_1 at a rate of λ_1 . Minimum stretching occurs when the orientation is parallel to \mathbf{d}_3 , at a rate of λ_3 . Again, the order of the eigenvalues is chosen such that $\lambda_3 < \lambda_2 < \lambda_1$. Two measures have been proposed by Ottino and Chella [22], and Ottino respectively to measure the efficiency of material stretching using the normalized material stretching rate ξ of a material vector and the rate of deformation tensor magnitude $\sqrt{\mathcal{D} : \mathcal{D}}$

$$e_L = \frac{\xi}{\sqrt{\mathcal{D} : \mathcal{D}}} \quad (3.1.20)$$

Ottino and Chella also defined a second measure to measure efficiency by comparing the ratio of normalized stretching rate ξ by the maximum eigenvalue λ_1 . This proved necessary because the e_L is always less than one, so the meaning of efficiency becomes somewhat lost.

$$\eta_L = \frac{\xi}{\lambda_1} \quad (3.1.21)$$

These two expressions of stretching efficiency are functions of the alignment between material vector and maximum principal direction. The line stretch efficiency e_L , proposed by Ottino, is found to always be less than the Cauchy-Schwartz inequality unless all eigenvalues are equivalently zero ($\lambda_1 = \lambda_2 = \lambda_3 = 0$), and is therefore not useful for the indication of optimal stretching. Alternatively, the latter parameter η_L , proposed by Ottino and Chella, is bounded by the largest eigenvector and not the magnitude of \mathcal{D} and therefore indicates optimal stretching ($\xi = \lambda_1$) when $\eta_L = 1$. In the 2D case, these measures are related as follows:

$$\frac{\eta_L}{e_L} = \sqrt{2} \quad (3.1.22)$$

3.2 Material Derivative of \mathbf{d}_i

Previous authors have developed expressions for the rate of change of the unit material vector \mathbf{p} . The derivation of this term is shown earlier in this chapter in equation

(3.1.13). In order to examine changes in the relative relationship between the material vector \mathbf{p} and the maximum eigenvector \mathbf{d}_1 , both the rate of change of the material vector $\dot{\mathbf{p}}$ and the rate of change of the maximum eigenvector, denoted by $\dot{\mathbf{d}}_1$ are needed. Later in this chapter, expressions will be derived that utilize the rate of change $\dot{\mathbf{p}}$ projected onto \mathbf{d}_1 and the rate of change $\dot{\mathbf{d}}_1$ projected onto \mathbf{p} . In the literature, little attention has been given to the material derivative of the rate of deformation tensor \mathcal{D} eigenvectors. Earlier authors [24] have incorrectly defined the rate of change of the the eigenvectors $\dot{\mathbf{d}}_i$ as follows:

$$\dot{\mathbf{d}}_i = \mathcal{W} \cdot \mathbf{d}_i \quad i = 1, 2, 3 \quad (3.2.1)$$

Consideration of a fluid element on a streamline in uniform shear readily shows this relationship does not hold. In uniform shear, the eigenvectors of \mathcal{D} remain fixed at all times, 45° to the shearing direction [2]. However, for a non-zero shearing rate, vorticity is also non-zero. Therefore, (3.2.1) would indicate a constant non-zero rotation of the eigenvector set $\{\mathbf{d}_1, \mathbf{d}_2, \mathbf{d}_3\}$ through space. Therefore, there is need for a new parameter to properly describe the rotation of the eigenvectors \mathbf{d}_i . This tensor-valued parameter will be denoted as the twirl tensor \mathcal{T} . The twirl tensor is skew-symmetric. It should be noted that this tensor has a symmetric counterpart, but this will not be discussed in this thesis. The twirl tensor is then defined as the mapping of the eigenvector \mathbf{d}_i to its material derivative $\dot{\mathbf{d}}_i$.

$$\dot{\mathbf{d}}_i = \mathcal{T} \cdot \mathbf{d}_i \quad i = 1, 2, 3 \quad (3.2.2)$$

Building off the work by Guo and Liang [12, 13] for the derivation of the material derivative of the 3D deformation tensor eigenvectors, a new 2D tensor for the expression of the rotation of the rate-of-deformation eigenvectors has been derived. The step-by-step derivation of the twirl tensor can be found in Appendix A. Presented below is a brief discussion detailing the major steps required to to find the value of

twirl. Starting an expression for the deformation tensor:

$$\mathcal{D} = \sum_{a,b} \lambda_a \delta_{ab} \mathbf{d}_a \otimes \mathbf{d}_b \quad (3.2.3)$$

Denote the rate of deformation tensor material derivative and twirl tensor:

$$\dot{\mathcal{D}} = \sum_{a,b} \dot{\mathcal{D}}_{ab} \mathbf{d}_a \otimes \mathbf{d}_b \quad (3.2.4)$$

$$\mathcal{T} = \sum_{a,b} \mathcal{T}_{ab} \mathbf{d}_a \otimes \mathbf{d}_b \quad (3.2.5)$$

Application of a identity shown in the appendix to these definitions then yields:

$$\mathcal{T}_{ab} = \frac{\dot{\mathcal{D}}_{ab} - \dot{\lambda}_a \delta_{ab}}{\lambda_b - \lambda_a} \quad (3.2.6)$$

Following more manipulation and simplification of expression (3.2.6) yields the final form of twirl tensor \mathcal{T} , which is a function of the rate-of-deformation tensor \mathcal{D} , the material derivative of the rate-of-deformation tensor $\dot{\mathcal{D}}$, and the maximum local stretching rate $\dot{\epsilon}$ (under the assumptions $\lambda_1 = \dot{\epsilon}$ and $\lambda_2 = -\dot{\epsilon}$).

$$\mathcal{T} = \frac{\dot{\mathcal{D}} \cdot \mathcal{D} - \mathcal{D} \cdot \dot{\mathcal{D}}}{4\dot{\epsilon}^2} \quad (3.2.7)$$

The twirl tensor is a spatial tensor that can be calculated at all points where the rate-of-deformation tensor is defined and non-zero. A new term, spatial variance, is used to describe regions in which the magnitude of twirl is non zero. Regions in which the magnitude of twirl is non zero are critical to improved material stretching. First, regions of spatial variance can generate rapid changes in the rate of interface stretching with little change in the interface orientation, resulting in regions of greater-than-linear growth rates in continuous velocity fields. Second, spatial variance allows for the transition of interface rotation behavior from shear-like to extensional-like behavior in continuous flow fields, resulting in a change in the equilibrium behavior of a material interface. Interestingly, following a similar procedure used to derive

(3.2.7), the rate of change of the maximum normalized stretching rate is shown to take the following form (for the 2D incompressible case where $\lambda_1 = -\lambda_2 = \dot{\epsilon}$):

$$\ddot{\epsilon} = \frac{\dot{\mathcal{D}} : \mathcal{D}}{2\dot{\epsilon}^2} \quad (3.2.8)$$

Given (3.1.13) and (3.2.7), new measures relating material orientation to the eigenvectors of the rate of deformation tensor can be derived.

3.3 Equilibrium Orientations

In any given flow, there can exist orientations along which a material vector does not rotate. This orientation is defined by angle θ , which is the angle between the material vector and the positive horizontal axis. These are called equilibrium orientations. The concept of these orientations is described in Charles L. Tuckers chapter [17]. In this work, two types of equilibrium orientations are defined; stable equilibrium orientations and unstable equilibrium orientations. As a material element approaches stable equilibrium, a material vector asymptotically approaches this orientation as time goes to infinity. Alternatively, an unstable equilibrium orientation has a zero rotation rate (as does the stable equilibrium orientation as a material element fully aligns) but is not an orientation to which a material element will asymptotically approach. To determine stable and unstable equilibrium orientations, $\ddot{\theta}$ is needed.

Numerous authors have shown the equilibrium orientation in simple shear flow is parallel to the shearing direction, which results in poor material stretching. In extensional flow, the equilibrium orientation is parallel to the maximum eigenvector orientation. Equilibrium orientations are found by solving the material derivative of a unit material vector for the angle at which it will not rotate. To do this, begin by

defining the material vector with components $S = \sin(\theta(t))$ and $C = \cos(\theta(t))$.

$$\mathbf{p} = \begin{Bmatrix} C \\ S \end{Bmatrix} \quad (3.3.1)$$

Then expand the material derivative of the material vector (3.1.13) into its component form using (3.3.1):

$$\begin{Bmatrix} -\dot{\theta}S \\ \dot{\theta}C \end{Bmatrix} = \begin{Bmatrix} \mathcal{D}_{11}C + \mathcal{D}_{12}S + \mathcal{W}_{12}S - (\mathcal{D}_{11}C^2 + 2\mathcal{D}_{12}CS + \mathcal{D}_{22}S^2)C \\ \mathcal{D}_{12}C + \mathcal{D}_{22}S + \mathcal{W}_{21}C - (\mathcal{D}_{11}C^2 + 2\mathcal{D}_{12}CS + \mathcal{D}_{22}S^2)S \end{Bmatrix} \quad (3.3.2)$$

Multiplication of $-\dot{\theta}S$ by $-S$, $\dot{\theta}C$ by C , substituting $\mathcal{D}_{22} = -\mathcal{D}_{11}$, and $\mathcal{W}_{21} = -\mathcal{W}_{12}$ yields.

$$\begin{Bmatrix} \dot{\theta}S^2 \\ \dot{\theta}C^2 \end{Bmatrix} = \begin{Bmatrix} -\mathcal{D}_{11}CS - \mathcal{D}_{12}S^2 - \mathcal{W}_{12}S^2 + (\mathcal{D}_{11}C^2 + 2\mathcal{D}_{12}CS - \mathcal{D}_{11}S^2)CS \\ \mathcal{D}_{12}C^2 - \mathcal{D}_{11}CS - \mathcal{W}_{12}C^2 - (\mathcal{D}_{11}C^2 + 2\mathcal{D}_{12}CS - \mathcal{D}_{11}S^2)CS \end{Bmatrix} \quad (3.3.3)$$

Adding these two equations yields:

$$\dot{\theta} = -2\mathcal{D}_{11}CS + \mathcal{D}_{12}(1 - 2S^2) - \mathcal{W}_{12} \quad (3.3.4)$$

Expanding this equation in terms of the unit strain and shear strain yields:

$$\dot{\theta} = -2\dot{\epsilon}CS - \dot{\gamma}_x S^2 + \dot{\gamma}_y C^2 \quad (3.3.5)$$

where $\dot{\epsilon}$ is the unit strain equivalent to \mathcal{D}_{11} , $\dot{\gamma}_x$ is the shear strain in the x direction equivalent to \mathcal{D}_{12} , and $\dot{\gamma}_y$ is the shear strain in the y direction equivalent to \mathcal{D}_{21} .

This general equation can be simplified in the presence of several simple stretching regimes. In simple shear with velocity in the horizontal direction, $\dot{\epsilon} = 0$, $\dot{\gamma}_x = \dot{\gamma}$, $\dot{\gamma}_y = 0$. Under these conditions, (3.3.5) reduces to:

$$\dot{\theta} = -\dot{\gamma} \sin^2(\theta) \quad (3.3.6)$$

In this flow regime, it can be shown that the interface $d\mathbf{x}$ is not rotating when the material vector is at $\theta = 0^\circ$ or $\theta = 180^\circ$ (parallel or anti-parallel to the velocity orientation). However, depending on the initial angle θ of the material vector \mathbf{p} , only one of these orientations is stable, and the other is unstable. Along a stable orientation, the rotation due to vorticity and the rate of deformation tensor are in balance. Conversely, at the unstable orientation, rotation due to vorticity and rotation due to the rate of deformation tensor are not in balance. Alternatively, in extensional flow, $\dot{\epsilon} = \dot{\epsilon}$, $\dot{\gamma}_x = \dot{\gamma}_y = 0$. (3.3.5) then reduces to:

$$\dot{\theta} = -2\dot{\epsilon} \sin(\theta) \cos(\theta) = -\dot{\epsilon} \sin(2\theta) \quad (3.3.7)$$

In the extensional flow regime, the interface experiences zero rotation at the four locations, $\theta = 0^\circ$, $\theta = 90^\circ$, $\theta = 180^\circ$, and $\theta = 270^\circ$. Again, not all of these orientations are stable.

One final consideration of the equilibrium orientation expressions is during a flow situation where both normal strain and shear strain are considered. The general equation takes the form:

$$\dot{\theta} = -\dot{\epsilon} \sin(2\theta) - \dot{\gamma}_x \sin^2(\theta) + \dot{\gamma}_y \cos^2(\theta) \quad (3.3.8)$$

This situation arises when a material element is traveling along a curved streamline. Solving this expression for $\dot{\theta} = 0$ provides the equilibrium orientations for a general 2D incompressible flow. However, not all combinations of arbitrarily chosen $\{\dot{\epsilon}, \dot{\gamma}_x, \dot{\gamma}_y\}$ will produce equilibrium orientations. As shown before, for simple flow conditions, some terms can be neglected, which aids in finding equilibrium positions. One example of a situation under which no equilibrium position exists is a point vortex where the velocity profile is given by $\mathbf{u} = -y\hat{i} + x\hat{j}$. Under this velocity profile, horizontal shear strain is $\dot{\gamma}_x = -1$ and vertical shear strain is $\dot{\gamma}_y = 1$. (3.3.8) then becomes $\dot{\theta} = 1$.

3.4 Orientation Factor

This focus of this work is to explore the stretching of a fluid-fluid interface element in continuous velocity fields using the eigenvectors of the rate of deformation tensor \mathcal{D} . In order to explore this relationship, expressions for the relation of material stretching of a material vector in terms of the eigenvectors of \mathcal{D} are necessary. These expressions are derived in terms of the material vector \mathbf{p} , the maximum eigenvector \mathbf{d}_1 , the rate of deformation tensor \mathcal{D} , the vorticity tensor \mathcal{W} , and the new tensor twirl \mathcal{T} , which was derived earlier.

As discussed in previous sections, available kinematic measures are not sufficient to express mechanisms of deformation across the entirety of the velocity field domain. Alternatively, continuum mechanics measures can describe the mechanisms of deformation across the velocity field domain but are not sufficient to describe the deformation of a fluid element within the velocity field. Therefore, measures must be developed that use the only relevant coordinate system available, the eigenvectors $\{\mathbf{d}_1, \mathbf{d}_2, \mathbf{d}_3\}$ of the rate-of-deformation tensor \mathcal{D} , as a coordinate system to explore mixing as a function of these parameters along streamlines. Two sets of measures are derived in this coordinate system. The first set of expressions, the interface orientation factor measures, which are denoted by O_p and \dot{O}_p , study changes of the fluid-fluid interface element \mathbf{p} as a function of the local velocity field. Substitution of these measure into previously discussed kinematical measure provides additional insight into the driving mechanisms behind deformation in these measures, shifting the perspective from an arbitrary spatial coordinate system to a more physically relevant coordinate system. This permits the analysis of a variety of incompressible laminar regime flows, provided that the flow fields being studied remain continuous in space and in time.

The second set of expressions, the velocity orientation factor measures denoted by

\dot{O}_u and \dot{O}_v , study the shear-equilibrium behavior of an interface. Expressed differently, the velocity orientation factor measures interface behavior as if the interface is parallel to the velocity (or shearing direction in a pure shear flow). These measures are useful for exploring interface stretching as a function of the mixing potential of the velocity field in a shear alignment, the alignment that is commonly found at long times in flows with non-zero shearing. These measures can be especially useful in cases where the behavior of an arbitrarily aligned interface is not useful and the potential of a velocity field for interface stretching is still needed.

The first measure of each set, denoted as the first interface orientation factor O_p and the first velocity orientation factor O_u , are functions of the respective material orientation and the maximum eigenvector \mathbf{d}_1 . In the general case, the first orientation factor is defined as the inner product of the maximum eigenvector \mathbf{d}_1 and an arbitrary material vector $\boldsymbol{\phi}$. This expression is:

$$O(\boldsymbol{\phi}) = \boldsymbol{\phi} \cdot \mathbf{d}_1 \quad (3.4.1)$$

At a fundamental level, the first orientation factor O_ϕ illuminates the relative spatial relationship between the maximum eigenvector \mathbf{d}_1 and an arbitrary material vector $\boldsymbol{\phi}$. With this relationship, the rate of material stretching relative to the maximum rate of material stretching can be directly demonstrated. The first specific form of the first orientation factor is the first interface orientation factor O_p , which is derived by substituting $\boldsymbol{\phi} = \mathbf{p}$ into (3.4.1),

$$O_p = O(\mathbf{p}) = \mathbf{p} \cdot \mathbf{d}_1 \quad (3.4.2)$$

(3.4.2) relates the relative spatial relationship of the material vector \mathbf{p} , which represents a infinitesimal element along a fluid-fluid interface, and the maximum stretching orientation. Using the orthogonality property of the principal directions ($\mathbf{d}_1 \cdot \mathbf{d}_2 = 0$), the value of the first interface orientation can be used to express the

stretching present in the fluid field. When the material vector is parallel ($O_p = 1$) or anti-parallel ($O_p = -1$) to the maximum eigenvector \mathbf{d}_1 , the material experiences the maximum possible local stretching. When the interface is perpendicular ($O_p = 0$) to the maximum eigenvector (parallel to the minimum eigenvector), the material vector experiences the maximum possible local contraction. Note that the value of the first interface orientation factor is always bound by $-1 \leq O_p \leq 1$.

There is opportunity to express established stretching expressions as a function of the first interface orientation factor. Shown below is a common line stretch expression used by a number of authors:

$$\frac{d\dot{s}}{ds} = \mathbf{p} \cdot \mathcal{D} \cdot \mathbf{p} = \dot{\epsilon} (1 - 2O_p) \quad (3.4.3)$$

Using the first interface orientation factor, the instantaneous local stretch equation can be expressed as a function of the alignment between the principal directions and the interface element, expressing stretching as a function of the alignment between material and principal directions.

Another measure, defined as the mixing efficiency (e_L), was originally put forth by Ottino [23, 24] as a natural bound on local mixing. Ottino found that the local instantaneous rate of stretch for viscous fluids is related to the local viscous dissipation.

$$e_L = \frac{\mathbf{p} \cdot \mathcal{D} \cdot \mathbf{p}}{\sqrt{\mathcal{D} : \mathcal{D}}} = (1 - 2O_p) \quad (3.4.4)$$

This relationship holds for both Newtonian and power law fluids, but becomes more complicated for fluids with other constitutive equations. Mixing efficiency was then used by Chella and Ottino [4, 5, 22] to describe the efficiency of intermaterial stretching in a variety of mixing domains for the identification of good and bad mixing. By substituting in the first material orientation factor, the measure can be reduced to a function of the spatial relationship between interface and eigenvector orientation.

The second specific form of the first general orientation measure, denoted as the

first velocity orientation factor (O_u), is defined by substituting the unit velocity orientation \mathbf{u} into (3.4.1).

$$O_u = O(\mathbf{u}) = \mathbf{u} \cdot \mathbf{d}_1 \quad (3.4.5)$$

Unlike the first interface orientation factor, the first velocity orientation factor is entirely a function of spatial parameters. In one respect, this measure can be seen as an expression for the potential mixing available in a flow at a particular point. As discussed, in simple deterministic flows, a material element converges to the stable equilibrium orientation. In both extensional and shear stretching regimes, this corresponds to the velocity orientation. Therefore, in these flows, the first velocity orientation factor immediate shows the potential for long time stretching in the local regime. Even in complex flows where stable equilibrium orientations do not lie parallel to the velocity orientation or do not exist, the material parallel or asymptotically approaching parallel to the velocity gives some indication to the imparted stretch for material elements which have converged to a shear-like orientation. This allows for an exploration of stretching potential independent of knowledge of the material element.

The first interface and first velocity orientation factor measures provide insight about the relationship between interface/velocity orientation relative to the maximum eigenvector of the rate of deformation tensor. However, it is also necessary to understand how these values are changing during material deformation in order to characterize changes in stretching regime and possible sources of material reorientation during flow. Again, a focus of this thesis is to identify reorientation phenomena in continuous flow fields where artificial reorientation due to piecewise continuous velocity fields are not an option and not physically realistic. Two more measures can be defined which express the rate of change of the first interface and first velocity orientation factors, which will be noted the second interface and second velocity orientation factors. Derivation begins with the material derivative of the first general orientation factor with the substitution of (3.1.13) and (3.2.7) for $\dot{\phi}$ and $\dot{\mathbf{d}}$ respectively.

$$\dot{O}(\boldsymbol{\phi}) = \mathbf{d}_1 \cdot \dot{\boldsymbol{\phi}} + \dot{\mathbf{d}}_1 \cdot \boldsymbol{\phi} \quad (3.4.6)$$

$$\dot{O}(\boldsymbol{\phi}) = \mathbf{d}_1 \cdot [\mathcal{D} - (\boldsymbol{\phi} \cdot \mathcal{D} \cdot \boldsymbol{\phi})\mathcal{I} + \mathcal{W}] \cdot \boldsymbol{\phi} + \boldsymbol{\phi} \cdot \mathcal{T} \cdot \mathbf{d}_1 \quad (3.4.7)$$

The above expression makes use of the first principal direction \mathbf{d}_1 , the rate of deformation tensor \mathcal{D} , the vorticity tensor \mathcal{W} , the twirl tensor \mathcal{T} and the identity tensor \mathcal{I} . The magnitude of the second orientation factor has contributions from two sources; the change in the vector of interest (the local interface orientation or the unit velocity orientation) projected onto the first principal direction and the change in the principal direction projected onto the local material interface orientation. The latter of these terms includes twirl, generating a wealth of information on the effects of spatially varying (non-zero twirl) velocity fields on interface growth. As the sum of these two relative motions, the second orientation factor expresses the rate of change of the first orientation factor, allowing for the characterization of regions of rapid stretching rate change. With this, deformation mechanisms present in a velocity field can now be characterized with the addition of twirl, indicating regions of potentially rapid interface stretching rate change with little observable effect in local interface orientation

Two specific forms of the second orientation factor are of interest, the second interface orientation factor (\dot{O}_p) and the second velocity orientation factor (\dot{O}_u). The second interface orientation factor is derived through the substitution of the unit interface orientation \mathbf{p} into (3.4.7). Note that this expression has been condensed from the form presented above.

$$\dot{O}_p = \mathbf{d}_1 \cdot [\mathcal{D} - (\mathbf{p} \cdot \mathcal{D} \cdot \mathbf{p})\mathcal{I} + \mathcal{W} - \mathcal{T}] \cdot \mathbf{p} \quad (3.4.8)$$

Similarly, the second velocity orientation factor is derived through the substitution

of the local unit velocity orientation \mathbf{u} into(3.4.7).

$$\dot{O}_u = \mathbf{d}_1 \cdot [\mathcal{D} - (\mathbf{u} \cdot \mathcal{D} \cdot \mathbf{u}) \mathcal{I} + \mathcal{W} - \mathcal{T}] \cdot \mathbf{u} \quad (3.4.9)$$

While the first orientation factor measures ((3.4.2) and (3.4.5) respectively) provide insight into the spatial relationship between the interface and the principal directions, the true effectiveness of twirl becomes apparent using the second orientation factor measures. In a spatially varying velocity field (velocity fields with non-trivial twirl), there is potential for the principal directions to change without significant change in the orientation of the velocity, resulting in a change in stretching regime without a change in interface rotation (assuming the interface has already converged to some well behaved orientation), resulting in different growth regimes for little apparent change in stretching. Using these measures, these changes can be explored in a variety of velocity fields.

Chapter 4: Numerical Modeling

The application and subsequent analysis of the orientation factor measures derived earlier was done computationally. Computational fluid dynamics (CFD) presents an opportunity to study these measures in new flow field models and operating conditions through rapid implementation of new code. Using these results, the effectiveness of these measures for the description of mixing mechanisms can be evaluated. Numerical modeling of material deformation was accomplished in two stages. First, a steady state velocity field was generated for the flow field model. The technique used to generate the velocity field solutions varies between flow field models. Velocity field solutions were validated against the literature. Once an acceptable solution was generated which satisfied literature comparisons and convergence criteria (when applicable), an interface-tracking scheme was applied to simulate material deformation in the velocity field. Velocity field solution techniques are discussed in this chapter. The results of material deformation in these velocity fields is discussed in the following chapter.

All code and numerical modeling was done in MATLAB 2012a. In general, generated data was exported to separate files for later use.

Flow field models were chosen because of the wide range of material stretching regimes they collectively contain. Three flow field models were chosen to cover the spectrum of deterministic laminar stretching regimes, the Couette channel, the diverging channel, and the lid driven cavity. The flow field models contain pure shearing, pure extensional and mixed shear-extensional, and pure extensional, non-spatially variant mixed shear-extensional, and spatially variant mixed shear-extensional respectively. Again, spatial variance refers to regions of space where $||\mathcal{T}|| \neq 0$ along a streamline. The study of spatial variance is important because of the potential for rapid material vector orientation change with little change in the principal directions,

or alternatively little change in the material vector orientation with rapid changes in the principal directions.

In each flow field model, continuous stretching (in time and space) is studied. While experiments on discontinuous stretching have been performed in the past [9, 8, 10, 11] and are informative regarding the nature of interfacial reorientation, they do not adequately reflect the mechanisms found in real world (continuous) mixing operations. The following flow field models are constrained to two dimensions. Fluid species are incompressible, immiscible, with homogeneously distributed material properties throughout the domain enclosed by the velocity field. Fluid viscosity is assumed high, with a correspondingly low Reynolds number. All velocity fields are assumed to be steady state. All solid boundaries are considered impermeable and are therefore assumed to have no-slip conditions.

4.1 Velocity Field Solution Generation

4.1.1 Couette Channel

The Couette channel flow field model was one of the first models studied for mixing. However, continuous interface orientation in this flow field model is poor and therefore not used in mainstream industrial mixing applications.

Flow in the Couette channel is constrained by two non-permeable boundaries at the top and bottom of the channel. The vertical spatial coordinate is bounded with $0 < y < H$, where H is the channel height and y is the vertical height in the channel. The vertical spatial origin ($y = 0$) is fixed at the bottom boundary. Position in the horizontal direction in the channel is arbitrary because all points along a streamline in the down channel or up-channel direction appear identical to a Lagrangian particle traveling on a streamline. Therefore the horizontal location of material element does not need to be defined for deformation analysis. The top wall has a constant non-zero

velocity of $\mathbf{u}(x, H) = \{U_0, 0\}$ in the rightward direction (down channel). The bottom wall is fixed, $\mathbf{u}(x, 0) = \{0, 0\}$. The geometry of the flow field model is shown below.

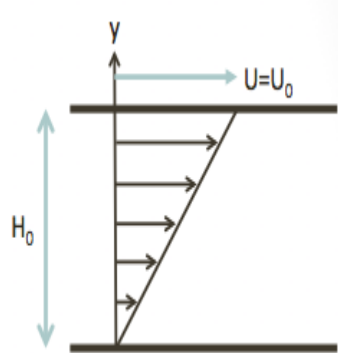


Figure 4.1: Couette Flow Model

The velocity profile generated in this can be found exactly as:

$$\mathbf{u}(x, y) = \left\{ \frac{U_0 y}{H}, 0 \right\} \quad (4.1.1)$$

Note that all streamlines are in the down channel direction, also known as the shearing direction, as a result of the velocity profile.

In the couette channel, the rate of deformation tensor, the vorticity tensor, and the twirl tensor can be given in closed form.

$$\mathcal{D} = \begin{bmatrix} 0 & \dot{\gamma} \\ \dot{\gamma} & 0 \end{bmatrix} \quad (4.1.2)$$

$$\mathcal{W} = \begin{bmatrix} 0 & \dot{\gamma} \\ -\dot{\gamma} & 0 \end{bmatrix} \quad (4.1.3)$$

$$\mathcal{T} = \begin{bmatrix} 0 & 0 \\ 0 & 0 \end{bmatrix} \quad (4.1.4)$$

4.1.2 Diverging Channel

Material stretching in the diverging channel flow field model is much preferable to the pure shear stretching present in the Couette channel, but is very difficult to produce in real world applications. The diverging channel uses a polar ($r - \theta$) coordinate system, with the origin ($r = 0$) located at the intersection of the two boundary walls. There is an angle of 2α between the channel boundaries, where α is defined as the divergence angle. The flow field model geometry is shown below.

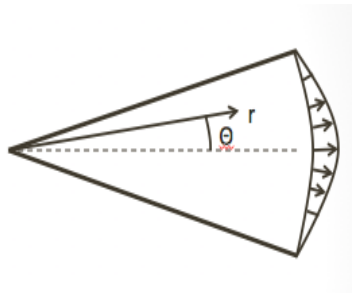


Figure 4.2: Diverging Channel Flow Field Model

The velocity profile for a fixed value of r is calculated using a third order non-linear differential equation produce by simplifying the Navier-Stokes equation. To derive the most useful form of this expression, several substitutions are required. First, define the scaled velocity parameter $F(\theta)$, which is a function of the channel radius as the radial velocity u_r and radial displacement r .

$$F(\theta) = u_r(r, \theta) r \quad (4.1.5)$$

The Navier-Stokes equation can then be expressed in terms of $F(\theta)$:

$$F''' + \frac{2}{\nu} F F' + 4F' = 0 \quad (4.1.6)$$

Second, introduce the non-dimensional scaled velocity parameter $G(\theta)$ which

scales the F parameter by its centerline value $F_0 = F(\theta)$.

$$G(\theta) = \frac{F(\theta)}{F_0} = \frac{u_r r}{F_0} \quad (4.1.7)$$

Substitution of $G(\theta)$ into (4.1.6) reduces the Navier-Stokes equations to the following form:

$$G''' + \frac{2\rho\alpha^2 F_0}{\mu} G G' + 4\alpha^2 G' = 0 \quad (4.1.8)$$

The above expressions are functions of the dynamic fluid viscosity μ , fluid density ρ , the scaled centerline velocity parameter f_0 , and divergence angle α . The $G(\theta)$ field profile was solved using the ODE45 package in MATLAB. The velocity profile can be found by reversing the substitutions used to generate the dimensionless equation.

$$\mathbf{u} = \left\{ \frac{GF_0}{r}, 0 \right\} \quad (4.1.9)$$

Note that the velocity is zero in the angular direction, and all streamlines radiate from the origin in the radial direction.

$$G(\theta) = \frac{F(\theta)}{F_0} = \frac{u_r r}{F_0} \quad (4.1.10)$$

Figure 4.3 is a sample $F(\theta)$ profile generated for a set of operating parameters $\{F_0, \alpha, \mu, \rho\} = \{0.1, 5^\circ, 10, 1000\}$. Note that the choice of simulation parameters was made to ensure that the velocity profile remained approximately parabolic.

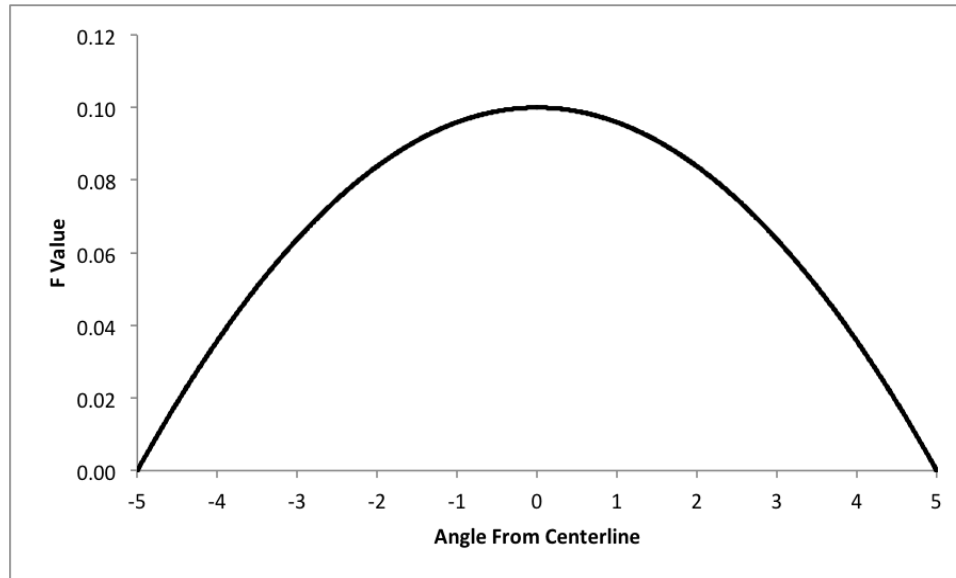


Figure 4.3: Diverging Channel Sample Velocity Profile

More information concerning the velocity profile solution in the diverging channel can be found in [29].

4.1.3 Lid Driven Cavity

The last 2D velocity field presented was the lid driven cavity flow, an approximation of the commonly used single screw extruder (SSE) used extensively in the polymer processing industry. The driven cavity is a well-explored CFD problem with a number of well-known solution techniques and was one of the first cavity models to demonstrate chaotic advection [6]. More information concerning this flow field model can be found in [26]. Transformation between SSE and driven cavity places a coordinate system attached to the screw of the SSE such that the stationary boundary walls in the velocity field (left, bottom, and right) are the sides (flights) of the screw and the moving boundary wall (top) represents the extruder barrel surface. In the 3D case, the top wall would move diagonally with velocity components in the down-channel (depth) direction and horizontally (a result of the moving screw). In the 2D case, the down channel component is neglected such that the top boundary speed is in the

horizontal direction with a value of $\mathbf{u} = \{U_0, 0\}$.

The cavity chosen has a height $H = 1$ and width $A_r H = 15$, where A_r is the aspect ratio (ratio of channel height to width) of the cavity. Figure 4.4 is a diagram of the lid driven cavity flow field model with streamlines.

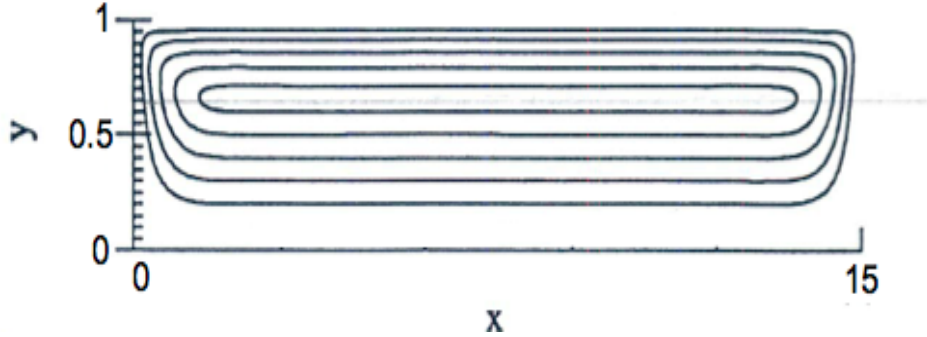


Figure 4.4: High Aspect Ratio Lid Driven Cavity Flow Field Model

The velocity field for the 2D lid driven cavity flow field model is obtained using the stream-vorticity formulation of the Navier-Stokes equation and vorticity equation to solve for the stream function ψ and vorticity ω in the cavity. This approach reduces meshing considerations immensely with respect to the pressure-velocity formulation which requires two staggered meshes. Note that the fluid is incompressible and that fluid viscosity and density are constant throughout the velocity field domain. Furthermore, $Re \ll 1$ due to the highly viscous nature of the polymers typically processed in these machines. The equations (4.1.11) and (4.1.12) are the stream-vorticity form of the Navier-Stokes and vorticity equations which need to be solved.

$$\frac{\partial \omega}{\partial x} \frac{\partial \psi}{\partial y} - \frac{\partial \psi}{\partial x} \frac{\partial \omega}{\partial y} = \frac{1}{Re} \left(\frac{\partial^2 \omega}{\partial x^2} + \frac{\partial^2 \omega}{\partial y^2} \right) \quad (4.1.11)$$

$$\frac{\partial^2 \psi}{\partial x^2} + \frac{\partial^2 \psi}{\partial y^2} = -\omega \quad (4.1.12)$$

Reynolds number for this flow field model is defined as:

$$\text{Re} = \frac{\rho U_0 A_r H}{\mu} \quad (4.1.13)$$

Where ρ is the fluid density, μ is kinematical fluid viscosity, H is the cavity height, A_r is the cavity aspect ratio, and U_0 is the top wall velocity. The velocity field in the cavity is considered to be fully developed. For this reason, transient terms were neglected in this formulation.

The fully developed stream-vorticity formulation of the driven cavity problem was solved analytically using a second order accurate finite difference scheme. Figure 4.5 shows the second order stencil patterns for the first and second derivatives in the \hat{i} and \hat{j} directions. First order derivatives are approximated using a first order, second order accurate, central difference. An example of a first derivative in the x direction by a second order finite difference approximation is shown below in Equation (4.1.14). Second order derivatives are approximated using a second order, second order accurate, central difference. An example of a second derivative in the x direction by a second order finite difference approximation is shown below in Equation (4.1.15). Figure 4.5 are the stencils used for this scheme. Nodal spacing s_p is equal in the vertical and horizontal directions, producing a square meshing. Therefore the distance between nodes in the vertical and horizontal directions is $\delta = s_p$. Nodes are categorized into two groups, boundary nodes and interior nodes. Interior nodes are solved using the cross stencil. Boundary nodes require a separate solution technique which incorporate boundary conditions along the walls.

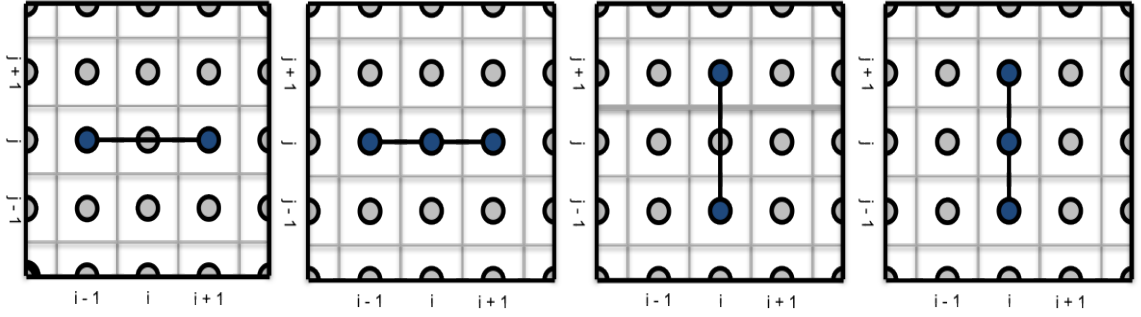


Figure 4.5: Central Finite Difference Stencil (in Nodal Coordinates)

$$\frac{\partial \phi}{\partial x} = \frac{\phi(x + s_p, y) - \phi(x - s_p, y)}{2s_p} \quad (4.1.14)$$

$$\frac{\partial^2 \phi}{\partial x^2} = \frac{\phi(x + s_p, y) - 2\phi(x, y) + \phi(x - s_p, y)}{s_p^2} \quad (4.1.15)$$

A three step iterative procedure is used to solve the stream function and vorticity fields until both fields have satisfied predefined convergence criteria. First, vorticity ω is solved at all interior nodes using the stream-vorticity relationship expressed in (4.1.12). Second, the stream function ψ is solved at all interior nodes using the Navier-Stokes equation in (4.1.11). Finally, the boundary conditions for ω and ψ are updated along all walls using the modified finite difference patterns. This iterative scheme is repeated until solution convergence criteria have been met. In general, the solution for a node at (x, y) will use nodal values for nodes at $(x - \delta, y)$, $(x + \delta, y)$, $(x, y - \delta)$, and $(x, y + \delta)$.

Velocity vector \mathbf{u} can then be extracted from ψ using the vector potential definition for velocity:

$$\mathbf{u} = \nabla \times \psi = \left\{ \frac{\partial \psi}{\partial y}, -\frac{\partial \psi}{\partial x} \right\} \quad (4.1.16)$$

Boundary values for both ψ and ω are required for all four boundary walls. ψ is

identically zero along all four boundaries. ω must be calculated from (4.1.12) at the start of each solution iteration using a phantom node approach for ψ . The following process is used to specify the ω value along the left boundary. A similar process will be used to specify the velocity at the top, right, and bottom boundaries. A solution can be derived by solving the first order centered finite difference expansion in terms of $\psi(0 - \delta, y)$, which is outside of the domain.

$$\psi(0 - \delta, y) = \psi(0 + \delta, y) - u_1(0, y)\delta \quad (4.1.17)$$

Equation (4.1.12) is then expanded in the horizontal direction. Note that the vertical terms are dropped because ψ is identically zero along all boundaries.

$$\omega(0, y) = - \left(\frac{\psi(0 + \delta, y) - 2\psi(0, y) + \psi(0 - \delta, y)}{\delta^2} \right) \quad (4.1.18)$$

Using $\psi(0, y) = 0$, $u_1(0, y) = 0$, and substituting (4.1.17) into (4.1.18) yields:

$$\omega(0, y) = - \frac{\psi(0 + \delta, y)}{\delta^2} \quad (4.1.19)$$

Similar boundary conditions are found for the right and bottom boundaries:

$$\omega(A_r H, y) = - \frac{\psi(A_r H - \delta, y)}{\delta^2} \quad (4.1.20)$$

$$\omega(x, 0) = - \frac{\psi(x, 0 + \delta)}{\delta^2} \quad (4.1.21)$$

Application of the ω boundary node calculation technique on the moving boundary (top) incorporating wall speed U_0 yields:

$$\omega(x, H) = - \frac{\psi(x, H - \delta) + 2U_0\delta}{\delta^2} \quad (4.1.22)$$

An over-relaxation scheme with relaxation parameter R was implemented along the boundaries. Due to the low Reynolds number, a relaxation parameter of $R = 1$ was chosen. For a different set of operational parameters (or with the inclusion of a time dependent terms), a relaxation parameter of $R < 1$ may be required. The

implementation of this scheme to the left boundary is shown below.

$$\omega(0, y) = \omega(0, y) + R \left(-\frac{\psi(0 + \delta, y)}{\delta^2} - \omega(0, y) \right) \quad (4.1.23)$$

A final note on boundary nodes is that the wall velocity of the top-left corner boundary node can be specified as both $\mathbf{u}(0, y) = \{0, 0\}$ and $\mathbf{u}(x, h) = \{U_0, 0\}$, as a result of the left and top wall boundary conditions. The wall velocity at the top-right corner can be specified in a similar way. Therefore, ω can be defined in two different ways depending on the value of horizontal velocity chosen at these points. This will result in a singularity at these two nodes, which is not conducive to a proper simulation. However, in the case where an interior node solution technique is used, the value at these nodes can be ignored because the finite difference stencil never uses these corner values.

Solution convergence (using stream function values) is checked by two methods. First, the infinity norm of the full vorticity field is compared every 50 iterations for solution convergence/divergence as the scheme progresses. Sufficiently small nodal spacing is used to guarantee accurate solution generation near the wall. Second, the high-iteration solution is compared to the analytical solution at $Re = 0$ for a high aspect ratio lid driven cavity to Tadmor and Gogos [28] who found an exact velocity profile given by.

$$u(y) = \frac{y}{H} \left(\frac{3y}{H} - 2 \right) \quad (4.1.24)$$

This proves to be a valid comparison due to the low Reynolds number used in this flow field model. Figure 4.6 is a sample centerline velocity comparison using the operating parameter set $\{Re, H, A_r, U_0, s_p\} = \{0.001, 1, 15, 1, 0.005\}$ compared against Tadmor and Gogos exact solution.

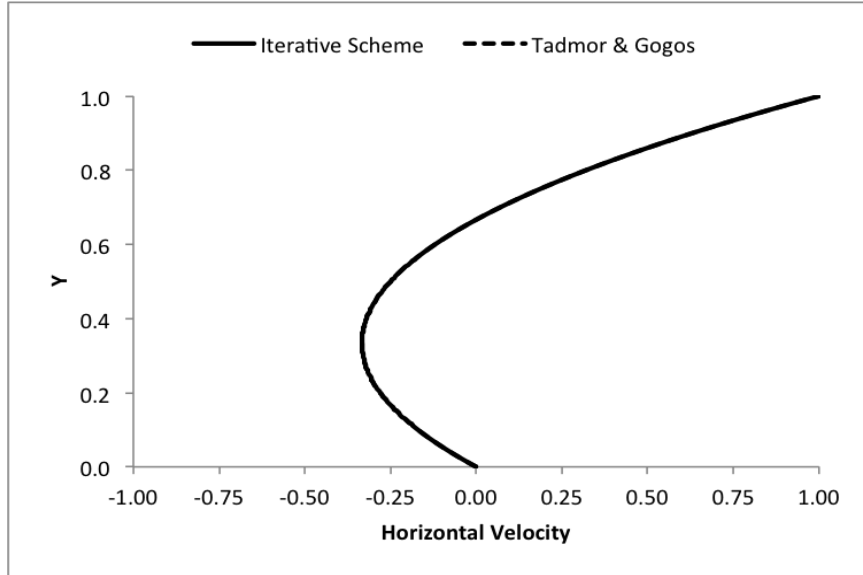


Figure 4.6: Lid Driven Cavity Centerline Velocity Profile Comparison

For the chosen mesh and operating parameters, the centerline velocity profile generated using in-house model and the $Re = 0$ exact solution provided by Tadmor and Gogos align very closely.

4.2 Interface Tracking

4.2.1 Couette and Diverging Channel

Interface deformation within the Couette channel model and diverging channel model can be easily calculated as a function of the velocity field and its gradients. Deformation along these streamlines is not subject to spatial variance. Therefore, the calculation of deformation in these flow field models is easily calculable.

4.2.2 Lid Driven Cavity

As stated earlier, in the 2D case, a fluid-fluid interface can be approximated at a point along the interface by an material vector $d\mathbf{x}$ which is tangent to the interface at that point. The tracking of this material vector as it travels about the flow field allows for

local deformation calculation at that instant. $d\mathbf{x}$ has magnitude ds and orientation \mathbf{p} . Movement of material vectors in the velocity domain are along streamlines. This is a result of the deterministic nature of steady state continuous laminar flow.

Forward time stepping of the interface is accomplished using the 2-D 4th order Runge-Kutta scheme with a sufficiently small time step to step the interface forward in the horizontal and vertical directions in the cavity. The forward stepping scheme applied to the horizontal direction.

$$x_{n+1} = x_n + \frac{1}{6}\delta_t (k_1 + 2k_2 + 2k_3 + k_4) \quad (4.2.1)$$

$$t_{n+1} = t_n + \delta_t \quad (4.2.2)$$

$$k_1 = u(t_n, x_n) \quad (4.2.3)$$

$$k_2 = u\left(t_n + \frac{1}{2}\delta_t, x_n + \frac{1}{2}\delta_t k_1\right) \quad (4.2.4)$$

$$k_3 = u\left(t_n + \frac{1}{2}\delta_t, x_n + \frac{1}{2}\delta_t k_2\right) \quad (4.2.5)$$

$$k_4 = u(t_n + \delta_t, x_n + \delta_t k_3) \quad (4.2.6)$$

Deformation of the interface in time is accomplished by expanding (3.1.12) using the first-order forward finite difference approximation. Time step δ_t is chosen to ensure that the total percent difference between initial stream value $\psi(t=0)$ and final stream value $\psi(t=t_f)$ is less than 0.5% over the time interval of the simulation. For each simulation, a runtime of 1000s was chosen to ensure that data are well within this streamline divergence requirement. A time step value of $\delta_t = 0.005$ was found to easily satisfy the criteria.

$$\frac{d\mathbf{x}_{n+1} - d\mathbf{x}_n}{\delta_t} = \left(\frac{\mathcal{L}_{n+1} + \mathcal{L}_n}{2} \right) \cdot d\mathbf{x}_n \quad (4.2.7)$$

The error associated with the first order forward finite difference approximation was found to be negligible in these simulations. In general, only the first 100 or less seconds of as simulation are presented in the following chapter, with the exception of

the semi-infinite divergent channel, which presents the first 150 seconds.

Chapter 5: Results

Application of the first and second orientation factor expressions to material deformation in continuous flow field models (specific models are discussed in Chapter 4) are presented. This chapter seeks to present information about material stretching, stretching rates (normalized and maximum normalized), and orientation factor measures characterize the behavior of these measures in the range of material stretching regimes chosen (shear, extensional, mixed, spatially variant), relate orientation factor results to phenomenon described in existing literature, and to characterize new phenomena. Results are presented for the Couette channel, diverging channel, and finally the lid driven cavity. This order was chosen because of the increasing complexity of stretching regimes and because results from the Couette channel and diverging channel are necessary to characterize behavior observed in the lid driven cavity. Results from these simulations indicate that the orientation factor measures provide a basis for intuitive and physically grounded exploration for material stretching in continuous velocity fields.

5.1 Semi-Infinite Couette Channel

Couette channel flow, or more generally simple shear flow, has been studied by numerous authors and is perhaps the most studied flow in early deterministic laminar mixing literature. Erwin and Ng [11] used this flow model for the demonstration of discontinuous interfacial reorientation and the effects on stretching achievable through reorientation. In a steady shear flow, it is well known that a material vector asymptotically converges to the shearing direction (the stable equilibrium orientation), which is parallel to the velocity orientation, resulting in linear material stretching at long times. In the Couette channel, the value of the rate of deformation tensor components are constant and equivalent at all times and locations in the domain. Consequently,

the magnitude of twirl is identically trivial at all points in the velocity field and is therefore neglected in the formulation of the second interface orientation factor. This reduces the form of \dot{O}_p to the material derivative of the material vector \mathbf{p} because twirl is a zero tensor. Simplification to this reduced form of \dot{O}_p was used by Spencer and Wiley, and Erwin in their shear growth expressions. Furthermore, the second velocity orientation factor \dot{O}_u reduces to zero due to the absence of change in velocity orientation and eigenvector orientations along any streamline.

Each figure shows 15 seconds of simulation for each material vector. The Z was chosen to collect sufficient data to comprehensively demonstrate material stretching in a shear stretching regime. Comparison of channels with different wall velocities showed that run time scales linearly with wall speed U_0 and inversely with shear rate $\dot{\gamma}$.

$$\frac{U_0}{\dot{\gamma}} t_{run} = \frac{U_0^2}{H} t_{run} = 15 \quad (5.1.1)$$

Four material elements were simulated in this flow field model, uniquely defined by their initial orientation with respect to the shearing direction. Note that all streamlines experience equivalent shearing rates. The orientations were 0° , 45° , 90° , and 135° , or given in their component forms, $\mathbf{p}_1 = \{1.000, 0.000\}$, $\mathbf{p}_2 = \{0.707, 0.707\}$, $\mathbf{p}_3 = \{0.000, 1.000\}$, and $\mathbf{p}_4 = \{-0.707, 0.707\}$

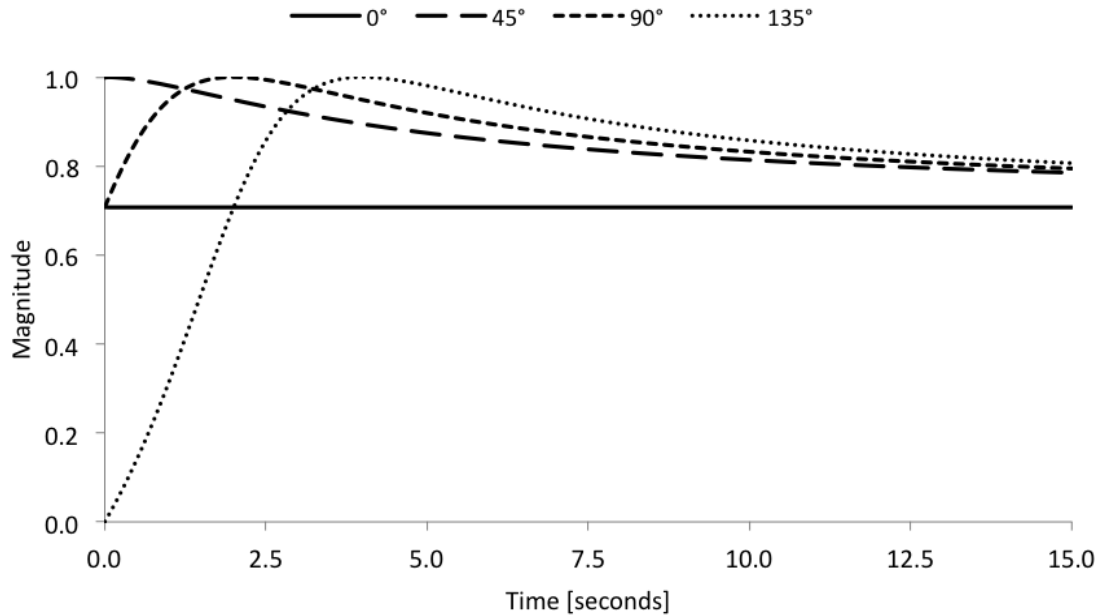


Figure 5.1: Couette Channel First Interface Orientation Factor vs. Time

Figure 5.1 shows the first interface orientation factor plotted against time. Material vector rotation under shear deformation becomes immediately apparent under inspection of this parameter. In time, each material vector rotates towards the stable equilibrium orientation, asymptotically approaching this orientation as $t \rightarrow \infty$. Material vector $d\mathbf{x}_1$, with an initial orientation parallel to the stable equilibrium orientation at $O_p = 0.707$, does not rotate in time. This is because there is no velocity gradient acting on this material element. Material vectors $d\mathbf{x}_2$, $d\mathbf{x}_3$, and $d\mathbf{x}_4$ rotate towards the stable equilibrium orientation over time.

It can be shown that for an appropriate time shift, i.e. shifting first interface orientation factor curves such that $O_p(t = 0) = 1.000$, each material vector rotation history is identical. Note that each interface instantaneously aligns with the maximum eigenvector orientation ($O_p = 1.000$) before asymptotically approaching the stable equilibrium orientation. Note that only $d\mathbf{x}_4$, with an initial angle of 135° , passes the minimum eigenvector orientation ($O_p = -1.000$), during which the in-

terface is experiencing maximum contraction. Note that $d\mathbf{x}_3$ and $d\mathbf{x}_4$ pass the zero growth orientation ($O_p = 0.000$) between the minimum and maximum eigenvector orientations after which all material deformation is positive stretch.

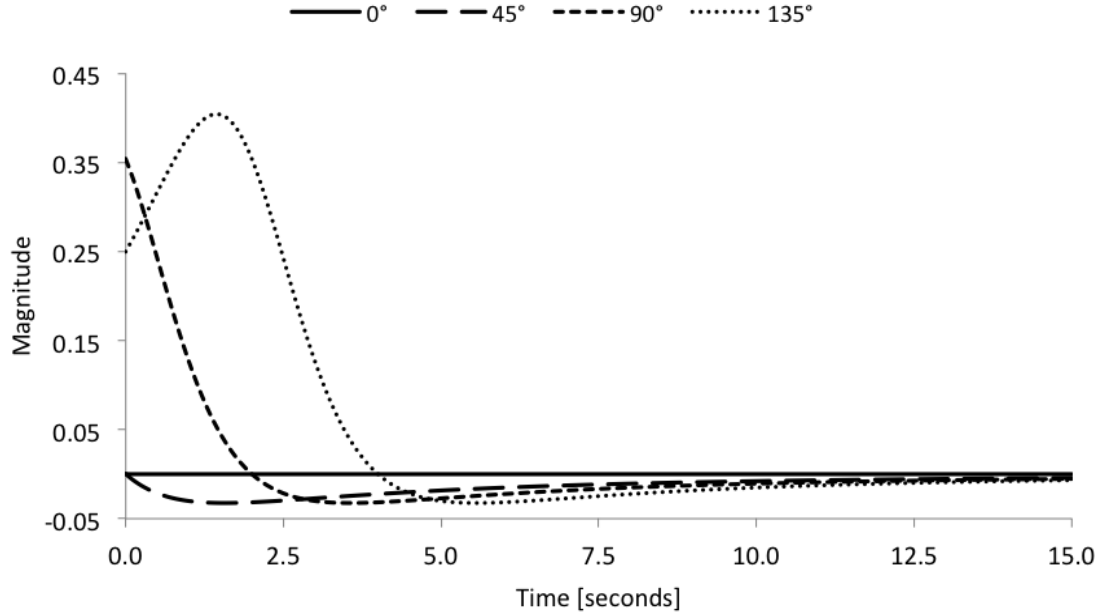


Figure 5.2: Couette Channel Second Interface Orientation Factor vs. Time

Again, in Figure 5.2, it can be shown that with an appropriate time shift, the value of the second interface orientation factor for each material vector is found to follow the same curve towards the stable equilibrium orientation at $\dot{O}_p = 0.000$. For each material vector, at the moment of alignment with the maximum eigenvector orientation, the value of second interface orientation factor undergoes a sign change, indicating that relative to the maximum principal direction, the interface is moving away, whereas before the instantaneous alignment of these orientations, each interface is moving towards the maximum eigenvector orientation. Furthermore, the highest rate of change of the interface orientation factor, with a value of $\dot{O}_p = 0.400$, occurs at the unstable equilibrium orientation which bisects the maximum and minimum eigenvector orientations and is perpendicular to the shearing direction.

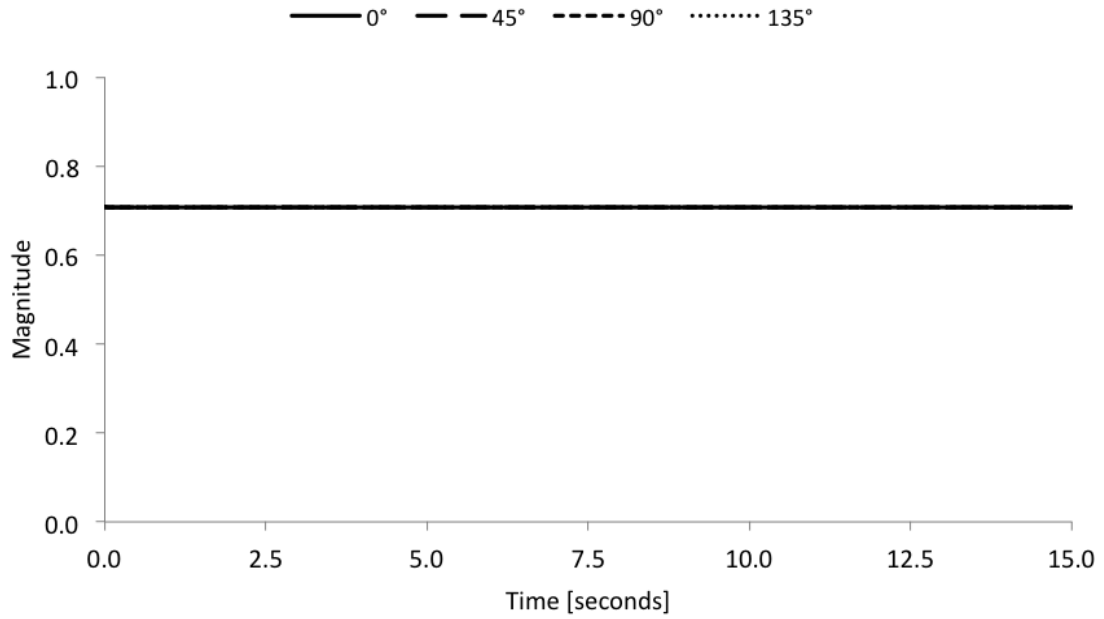


Figure 5.3: Couette Channel First Velocity Orientation Factor vs. Time

Figure 5.3 shows that the first velocity orientation factor remains identically equal to $O_u = 0.707$, corresponding to the stable equilibrium orientation, at all times along any streamline. This value is characteristic of a pure shear stretching regime.

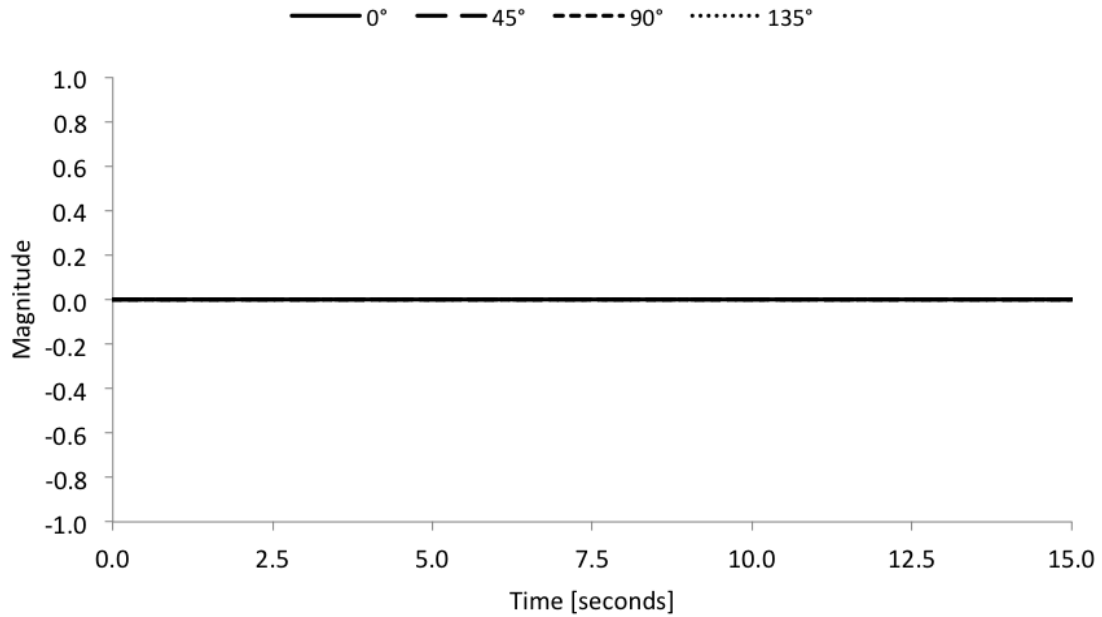


Figure 5.4: Couette Channel Second Velocity Orientation Factor vs. Time

Figure 5.4 shows that the second velocity orientation factor remains identically zero at all times along the streamline. This is consistent with the first velocity orientation factor.

An additional set of simulations was performed involving artificial reorientation. After the run time the interface, with known stretch, was adjusted back to its initial orientation, and was allowed to grow again. This was an idealized numerical reproduction of Lewis Erwin’s experiment on artificial reorientation. Results show that the first interface orientation factor in time was identical for each run time, but the resulting stretch improves with each run because the material elements passed the maximum eigenvector with each successive reorientation. However, at the instant the orientation was reset, the second interface orientation factor becomes infinity due to the instantaneous change in orientation of the interface element. As a result, the ineffectiveness of the orientation factor measure in spatially/temporally discontinuous flows becomes apparent.

5.2 Semi-Infinite Diverging Channel

The divergent channel provides the opportunity to explore two additional laminar stretching regimes, pure-extensional stretching and mixed shear-extensional stretching. Using these regimes and the shear stretching regime from the previous section as quantifiers, the velocity field domain can be divided into three sub-domains based on stretching regime. First, along the center streamline ($\theta = 0$), shear terms in the rate-of-deformation tensor are zero, resulting in a purely extensional flow. In this regime, an interface rotates rapidly to a stable equilibrium orientation which is perpendicular to the velocity orientation. In the second subdomain, defined from $0 < \theta < \beta$, where β is the critical angle at which the extensional rate and the shear rate are equivalent, the extensional terms dominate the shear terms, resulting in an similar stable equilibrium orientation compared to the centerline stable equilibrium orientation configuration (perpendicular to the velocity orientation). The final subdomain, defined from $\beta < \theta < \alpha$, where α is the angle between the centerline and channel wall, the shear deformation dominates extensional deformation. In this sub-domain, interfacial rotation is observed to act in a more shear-like manner, despite the presence of extensional terms in the rate-of-deformation tensor.

As with the Couette channel, there is zero spatial variance along any streamlines. However, there is spatial variance across streamlines. Because of this, the twirl tensor is non-zero. As a result, different streamlines will produce a non-trivial values for the first velocity orientation factor and a trivial value for the second velocity orientation factor. The values found for the first velocity orientation factor will be discussed later in this section.

Interfaces in the semi-infinite diverging channel are defined by three parameters; displacement from the source in the radial direction denoted by r , angular displacement from centerline denoted by θ , and material orientation with respect to the radial

direction (parallel to the streamline) denoted by p . Each interface has identical radial displacement and initial orientation with respect to streamline. In ascending order, the tracer interfaces have angular displacements of $\theta = 0^\circ$, $\theta = 1^\circ$, $\theta = 2^\circ$, and $\theta = 4^\circ$. The first material interface is located along the centerline, which is unique with zero vorticity and therefore will impart pure extensional stretching to a tracer located along this streamline. The second material interface resides within the extensional dominated subdomain of the channel while the third and fourth interfaces reside within the shear-dominated subdomain, although the third material interface only deviates slightly from the pure extensional orientation at equilibrium. Interfaces with negative angular displacement will also be included as a function of symmetry and the effects of vorticity in the channel.

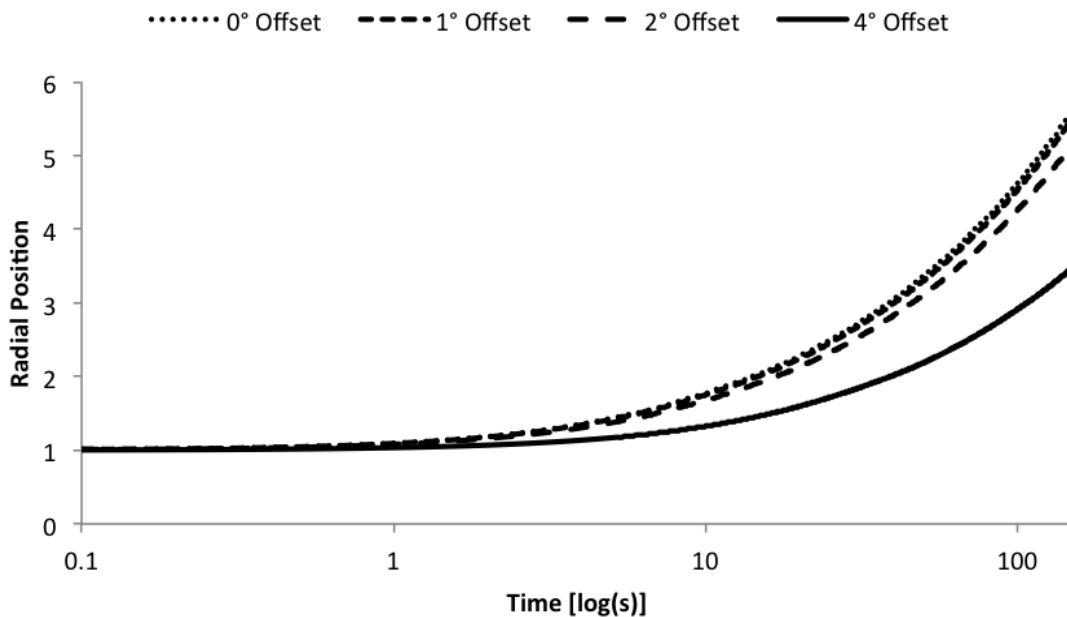


Figure 5.5: Diverging Channel Material Vector Position (Radial) vs. Time

Note that the displacement for the 0° and 1° material vectors is nearly equivalent and difficult to visually distinguish in Figure 5.6 although the 0° material vector does have a higher displacement than the 1° material vector. As the angular displacement

from the centerline increases, the fluid velocity along that streamline relative to the fluid velocity on the centerline decrease. Therefore, material vector displacement in time decreases as the angular displacement increases.

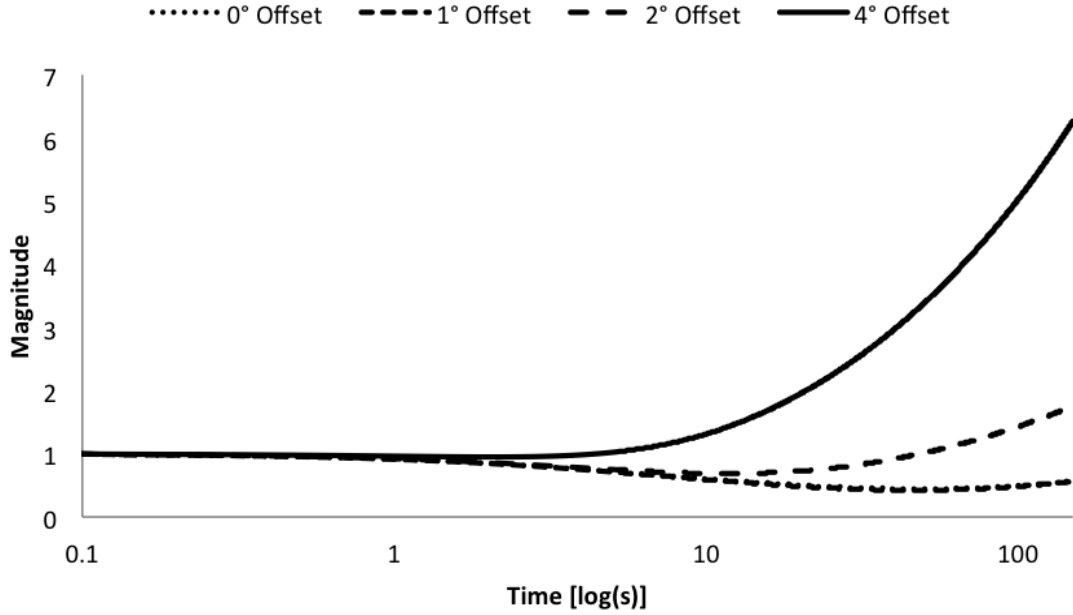


Figure 5.6: Diverging Channel Material Stretch vs. Time

Note that the 0° and 1° streamline material vectors stretch in a very similar fashion and are difficult to distinguish in Figure 5.6. The initial orientation of the each interface is unfavorable relative to the maximum eigenvector of \mathcal{D} , resulting in a decrease in material stretch before rotation into a favorable orientation. The material vectors along the 0° and 1° are transported away from the source point most rapidly and are not located on streamlines with good deformation characteristics, resulting in lower pure-extensional deformation for the 0° streamline and lower mixed shear-extensional deformation for the 1° streamline when compared to streamlines with higher angular displacement from centerline. These material vectors reach their minimum material stretch of $ds_1 = ds_2 = 0.444$ at $t = 48.70$, which can be seen in 5.6. The 1° streamline material vector reaches its minimum stretch of $ds_3 = 0.688$ at

$t = 11.80$. The 4° streamline material vector reaches a minimum stretch of $ds_4 = 0.950$ at $t = 2.10$. Note that at the minimum stretch point, the material vector then orients into a favorable stretching orientation and begins to stretch. At $t = 150s$, the material vectors have acquired stretches of $ds_1 = 0.560$, $ds_2 = 0.566$, $ds_3 = 1.760$, and $ds_4 = 6.272$, respectively. It is interesting to note that the most stretch acquired along the 2° and 4° streamlines.

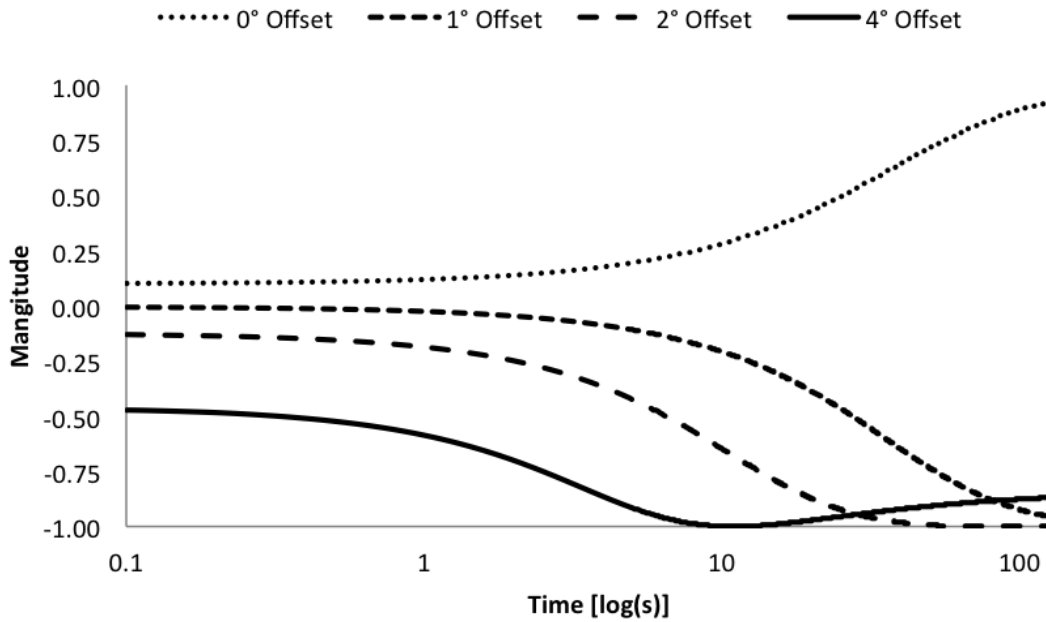


Figure 5.7: Diverging Channel First Interface Orientation Factor vs. Time

The interface orientation factor shows the path to equilibrium position of each interface. Unlike the Couette channel, the final orientation factor value is a function of both rate and extension rate. The first streamline has zero vorticity and is an example of a purely extension stretching regime. Streamlines two, three, and four have both extension rate and shear rate terms, with the shear rate increasing as a linear function of angular displacement θ . For all streamlines with an angular displacement $\theta > 0$, the final orientation factor value is negative, indicating alignment towards the second principal direction. At negative angular displacements, the value

of vorticity is opposite, resulting in a positive equilibrium position in the direction of the first principal direction. As the angular displacement θ increases, the final orientation factor changes from alignment approximately along a principal direction to an approximately shear stretching orientation. The long-time equilibrium position of each interface, taken at $t = 5000$, are $O_p = 1.0000$, $O_p = -0.9956$, $O_p = -0.9758$, $O_p = -0.8402$ respectively. To relate this back to mixing, recall that the stretch of a material interface is proportional to an increase in the mixing in the cavity, so that a long interface between two fluid bodies is indicative of greater mixing. Showing the orientation of the material element that represents the interface is critical to predicting regions of fast and slow stretching. The first interface orientation factor provides this information. Again, the ideal case is a material element parallel to the maximum eigenvector of the rate of deformation tensor, which is found along the streamline.

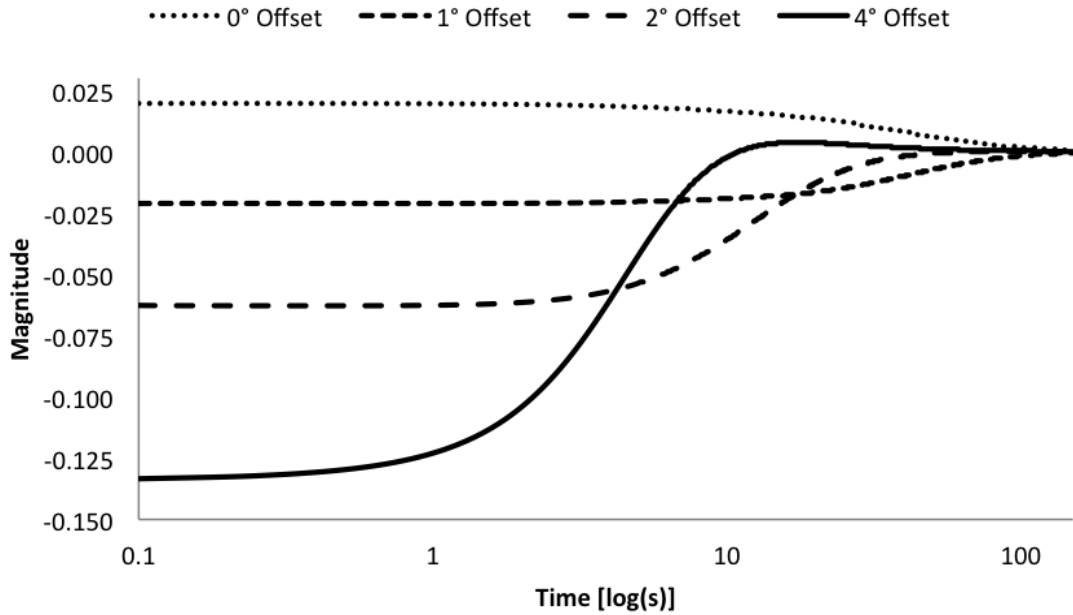


Figure 5.8: Diverging Channel Second Interface Orientation Factor vs. Time

Figure 5.8 shows the rotational rate of the interface in the flow with time, which

is expressed by the second interface orientation factor. . As the displacement angle θ increases, the rate of rotation increases. For the first three interfaces ($\theta = 0^\circ$, $\theta = 1^\circ$, and $\theta = 2^\circ$), the rate of change towards steady state remains positive at all times, although at a decaying rate over time (which is a result of increasing radial displacement from the source over time). The 4th interface however undergoes a sign change much like interfaces with a large angular displacement from equilibrium in the Couette channel, passing through the second principal direction to end at an equilibrium orientation discussed in the Figure 5.7. The rate at which each interface approaches equilibrium increases (resulting in a decreased time spent in a transient state), which is again consistent with the increasing vorticity and relatively constant extension rate as the displacement angle θ increases.

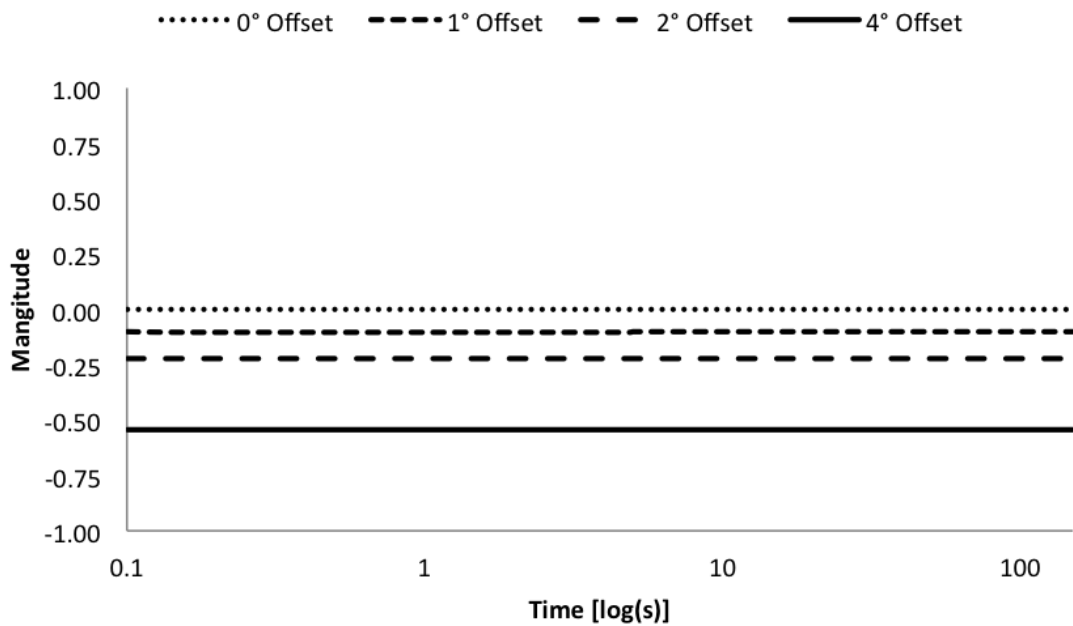


Figure 5.9: Diverging Channel First Velocity Orientation Factor vs. Time

Along each streamline, the value of the first velocity orientation factor remains constant. Therefore, spatial variance is identically zero along an arbitrary streamline in the diverging channel. However, the first velocity orientation factor will have

different values for two different streamlines, resulting in from the change in the ratio between the extensional and shearing terms in the velocity gradient. For the centerline streamline, the first velocity orientation factor has a value of $O_u = 0$, which is the characteristic value for pure-extensional flow. In the diverging channel, the maximum eigenvector is perpendicular to the flow velocity. However, as the angle θ between the centerline and the streamline increase, the value of the first velocity orientation factor begins to change from $O_u = 0$ to $O_u = -0.707$ (very close to the boundary). Values with angular displacements of $-\theta$ were found to range from $O_u = 0$ to $O_u = 0.707$. There is not a discrete boundary between extensional and shear like effects. Instead, the transition happens somewhat continuously over the angular width of the channel. This effect was shown by Vincent and Agassant [30] for the inclusion of fiber fillers into a high viscosity polymer matrix, where approximately extensional regime fiber behavior was observed for angular displacements of $0 < \theta < \beta$, where β is defined as the critical angle bounded by $0 < \beta < \alpha$, and approximately shear regime fiber behavior was observed for angular displacements of $\beta < \theta < \alpha$.

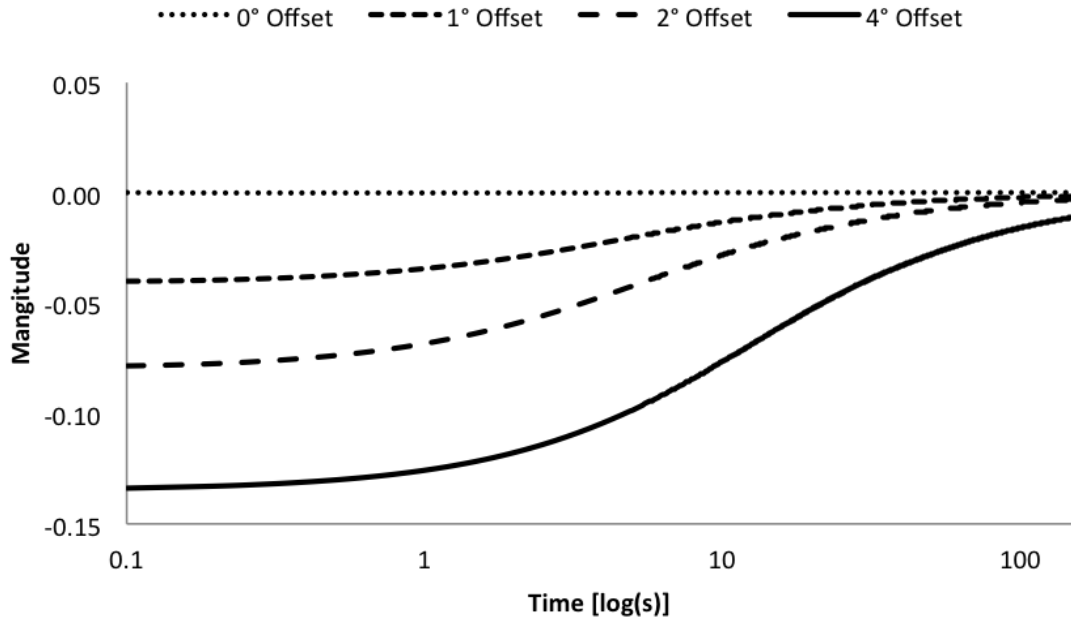


Figure 5.10: Diverging Channel Second Velocity Orientation Factor vs. Time

Examination of the second velocity orientation factor to the diverging channel yields interesting results for mixing. As stated before, the twirl tensor changes because the orientation of the eigenvectors of the rate of deformation tensor are different between different streamlines. This phenomenon, while intriguing, does not appear to effect material stretch along the streamlines.

5.3 Lid-Driven Cavity

Mixing in the 2D lid driven cavity has been studied in depth. [4, 6, 22]

Two objectives were identified for mixing in the 2D driven cavity: characterization of mixing in differing regions of the cavity and characterization of orientation factor behavior in these regions. The lid driven cavity is the most complex flow field presented investigated since it contains regions of pure-shear, pure-extensional, mixed shear-extensional stretching as well as regions with spatial variance ($\|\mathcal{T}\| \neq 0$) along streamlines. In the regions of spatial variance, changes in both the orientation be-

tween the material and eigenvectors as well as the eigenvectors relative to the material are expected, both of which would lead to rapid changes in material stretching.

The lid driven cavity model is divided into four regions, the upward flight (left corner), the downward flight (right corner), the upper steady shear flight (SSF) and lower SSF. An illustration of these regions is shown in Figure 5.11

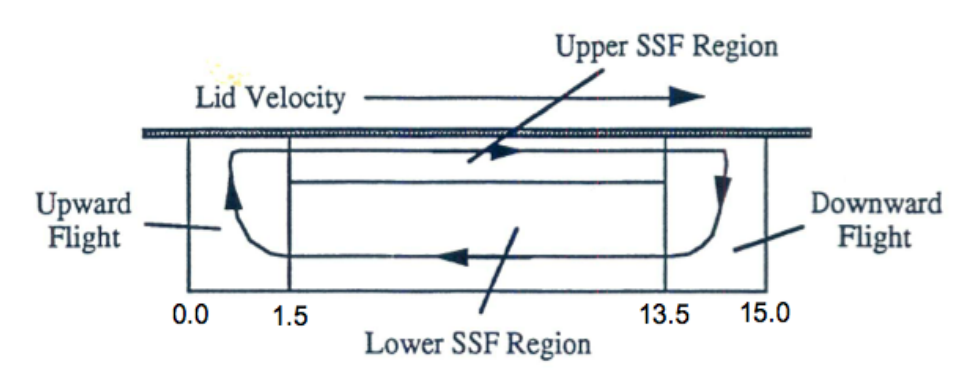


Figure 5.11: Lid Driven Cavity Regions

Fluid in the left corner moves upward and fluid in the right corner moves downward. The upward and downward flights are defined within 1.5 cavity heights H of the left and right walls respectively. This value was chosen so that only shear-like behavior is found in the steady shear regions, and all non-shear like behavior is found in the upward and downward flights. Similarly, using the centerline velocity profile in Figure 4.6, fluid in the upper SSF (top 1/3 of the cavity) is moving in the rightward direction, in the direction of the moving boundary, while fluid in the lower SSF (bottom 2/3 of the cavity) is moving to the left, against the motion of the moving boundary. More formally, each region is bounded by the following dimensions:

	x_{min}	x_{max}	y_{min}	y_{max}
Upward Flight	0.00	1.50	0.00	1.00
Upper Steady Shear Flight	1.50	13.50	0.67	1.00
Lower Steady Shear Flight	1.50	13.50	0.00	0.67
Downward Flight	13.50	15.00	0.00	1.00

Note that the upward and downward flights are chosen so that all spatial variance is contained in these regions. Fluid deformation in the upper and lower steady shear regions is pure shearing.

Material vector deformation was explored on two streamlines with initial spatial coordinates $\mathbf{x}_1 = \{7.50, 0.45\}$ and $\mathbf{x}_2 = \{7.50, 0.23\}$. Both interfaces have identical initial orientations of $\mathbf{p}_1 = \mathbf{p}_2 = \{0, 1\}$, perpendicular to the streamline. The former initial coordinate is denoted as the inner streamline after its position relative to the wall and the zero velocity zone separating the upper and lower steady shear flights. The latter initial coordinate is denoted as the outer streamline.

These two streamlines are chosen to best illustrate the effects of twirl on material deformation in a case where the absolute magnitude of twirl magnitude is relatively small (although still greater than zero) and where the absolute twirl magnitude is relative large. Only two streamlines are necessary to adequately explore the differences between these two effects, because any other streamlines will exhibit similar phenomenon. Material vector deformation was simulated for 300 seconds at a time step length of $\delta_t = 0.005$. However, only 70 seconds of each simulation are presented in the following section. Past this time, material deformation repeats because the material passes through the the channel again. Passage of the material vector through the lower steady shear, upward flight, upper stead shear, and downward flight is presented. Subsequent travel around the cavity beyond the first circuit is stream value versus stream value reference deviation testing. Symmetry is expected between the

upward flight and the downward flight.

For each streamline, two sets of critical times are discussed. These times correspond to the maximum twirl magnitude, termed the peak twirl time, and the maximum streamline curvature. Peak twirl $\|\mathcal{T}\|_{max}$ corresponds to the time at which $\|\mathcal{T}\|$ is maximum in the upward and downward flights. Peak streamline curvature κ_{max} corresponds to the maximum value of curvature κ in the upward and downward flights. These critical times are of interest because of the potential for rapid changes in the material stretching regime due to these reorientations. Streamline curvature is defined as follows:

$$\kappa = \det \left(\frac{\partial \mathbf{x}}{\partial t} \otimes \frac{\partial^2 \mathbf{x}}{\partial t^2} \right) \left\| \frac{\partial \mathbf{x}}{\partial t} \right\|^{-3} \quad (5.3.1)$$

In the lower shear flight, both interfaces rapidly converge to the stable equilibrium orientation (parallel to the shear/velocity and 45° to the principal directions). At the transition from lower steady shear region to the upward flight, the value of O_p approximately converges to first velocity orientation factor. Similarly, the value of second interface orientation factor approximately converges to the second velocity orientation factor. Therefore, while both interface orientation factors and velocity orientation factor figures are presented, they are approximately the same after a small time.

5.3.1 Inner Streamline ($y_0 = 0.45$)

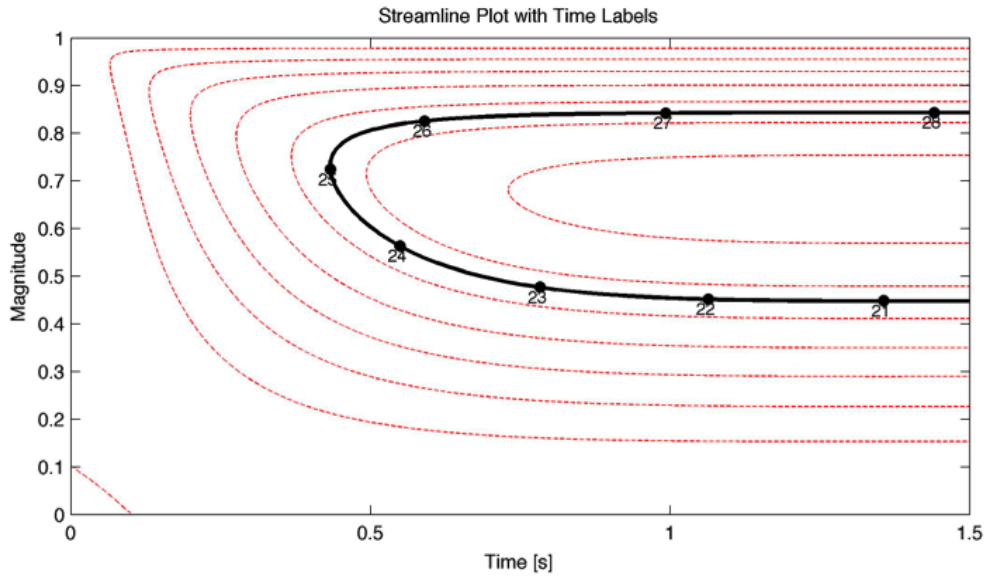


Figure 5.12: Lid Driven Cavity Interface Path for $y_0 = 0.45$

The inner streamline is defined as the streamline along which the material elements initial location is $\mathbf{x}_0 = \{7.50, 0.45\}$ and initial orientation $\mathbf{p}_0 = \{0, 1\}$. The material vector enters the upward flight at $t = 20.40s$. The material vector achieves peak twirl value in the upward flight at $t = 24.18s$ and maximum streamline curvature at $t = 25.25s$. The interface leaves the upward flight and enters the upper steady shear region at $t = 28.30s$ and then into the downward flight at $t = 54.96s$. Finally, the material vector transitions in the lower steady shear region at $t = 62.58$. A material vector on the inner streamline completes a single loop of the cavity every 84.09 seconds. Note that transition is defined as the movement of the material vector from one region to another (such as from the downward flight into the lower steady shear region).

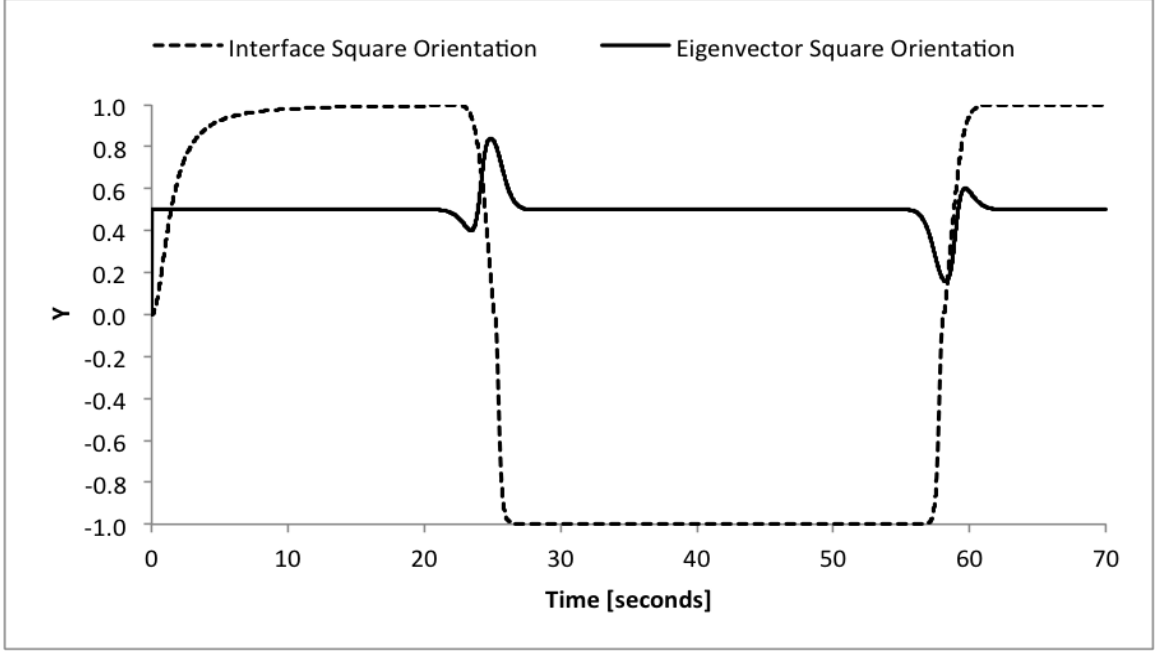


Figure 5.13: Lid Driven Cavity Square Orientation Plot for \mathbf{p} and \mathbf{d}_1 for $y_0 = 0.45$

Before exploring the O and \dot{O} values along the streamline, it is important to discuss the orientations of the maximum eigenvector orientation \mathbf{d}_1 and material vector orientation \mathbf{p} in order to explore changes in the orientation of the two parameters. This is necessary because the second orientation factor makes no distinction between rotations in the material vector or the eigenvectors. Figure 5.13 and Figure B.26 show the sign adjusted square orientation between the interface/velocity orientation and the positive horizontal axis.

$$\Theta(\boldsymbol{\phi}) = \text{sgn}(\boldsymbol{\phi} \cdot \mathbf{x})(\boldsymbol{\phi} \cdot \mathbf{x})^2 \quad (5.3.2)$$

A sign adjusted square orientation value of $\Theta = 1$ corresponds to a direction parallel to the positive reference direction \mathbf{x} . A value of $\Theta = 0$ is perpendicular to the reference direction \mathbf{x} . A value of $\Theta = -1$ is anti-parallel to the reference direction \mathbf{x} , or alternatively parallel to $-\mathbf{x}$.

In the lower steady shear region, the maximum eigenvector orientation remains

constant at $\Theta = 0.5$, consistent with a steady shear stretching regime (i.e. 45° to the velocity orientation). Upon entering the upward flight region, the interface begins to lose orientation (rotate away from the reference direction). The maximum value of twirl is achieved at $t = 24.18$, illustrated by the transition from concave to convex orientation curve. For the inner interface, observe that the principal direction does not undergo a flip, with the maximum difference between the maximum and minimum orientation value of $\Theta = 0.44$. This indicates that the equilibrium orientation of the eigenvector orientation does not change during the entirety of the corner traversal, entering and departing the corner at the same shearing orientation. At the entrance to the upper steady shear region, the maximum eigenvector again has an orientation of $\Theta = 0.5$ and maintains this orientation throughout the upper steady shear region. Once the interface enters the downward flight, the principal directions undergo a similar wobble about the $\Theta = 0.5$ value, reaching a local minimum at the downward flight maximum curvature time and a local maximum at the downward flight peak twirl time. The principal direction orientation then returns to a value of $\Theta = 0.5$ in the lower steady shear region, which is maintained throughout the region. Again, the principal direction orientation remains equivalent at the entrance and exit of the downward flight.

In the lower steady shear region, the interface begins with an orientation of $\Theta = 0$, corresponding to the initial orientation perpendicular to the streamline. The material vector then begins to orient to the stable equilibrium orientation, parallel to the velocity as a result of shearing. At the entry to the upward flight, the interface has an orientation at approximately $\Theta = 1$, which rapidly changes to $\Theta = -1$ by the end of the upward flight. The material maintains this orientation, which is parallel but oriented in the opposite direction of the velocity in the upper steady shear region. Upon entering the downward flight, the interface then follows the stable equilibrium orientation, rotating most rapidly at the maximum streamline curvature. At the

transition between downward flight and lower steady shear region, the interface has assumed its asymptotically decaying orientation of approximately $\Theta = 1$.

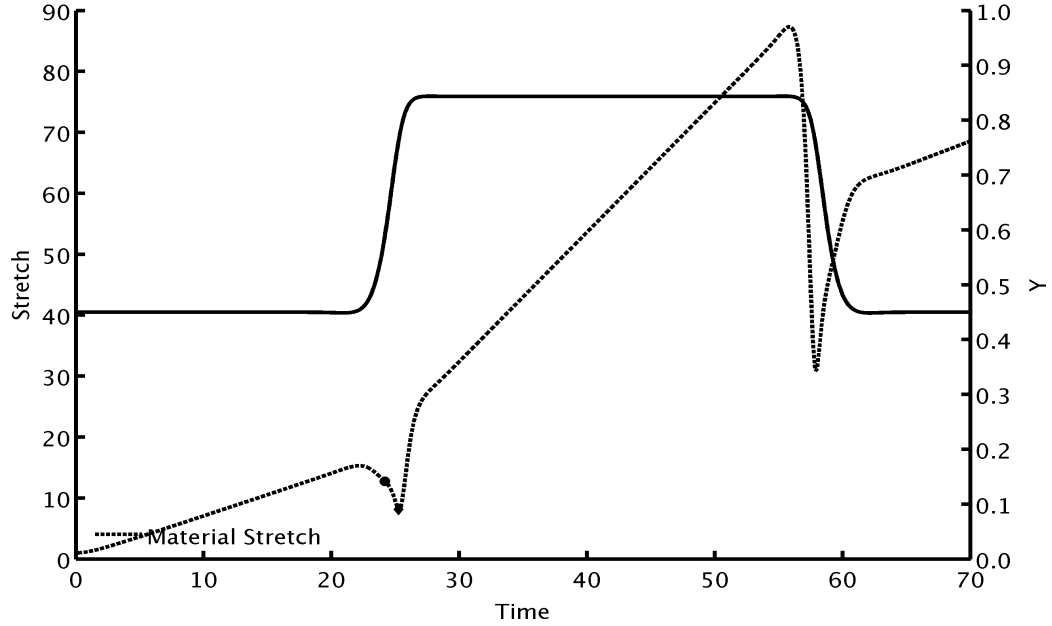


Figure 5.14: Lid Driven Cavity Material Stretch for $y_0 = 0.45$

Figure 5.14 shows the material vector stretch on the inner streamline. Material vector stretch in the lower steady shear region briefly has a greater than linear rate as the material orients parallel to the maximum eigenvector \mathbf{d}_1 . Shortly after, as the material asymptotically approaches the stable equilibrium orientation, the material vector continues to grow linearly in time in the lower steady shear region. Shortly after the material vector enters the upward flight, the material vector achieves a local maximum of stretch of $ds = 14.61$ before it becomes oriented unfavorably, resulting in loss of stretch. The interface reaches a local minimum of $ds = 8.11$ before becoming favorably orientated and beginning to regain stretch. Favorably refers to an orientation which produces positive stretching, which produces better mixing. At this time, the interface gains stretch at a greater than linear rate before returning to a more linear rate. After transitioning into the upper steady shear region, the

material vector resumes stretching at a linear rate, which remains approximately constant throughout the entirety of the upper steady shear region. Note that the apparent rate of growth appears greater in the upper steady shear region than in the lower steady shear region due to the increased shearing rate $\dot{\gamma}$. Upon entering the downward flight, the material stretch reaches a peak of $ds = 83.23$ before becoming unfavorably oriented and rapidly losing stretching, reaching a minimum of $ds = 28.89$, 1.69 seconds after the maximum stretch before becoming again favorably orientated and beginning to regain stretch at a greater than linear rate. As the material vector transitions into the lower steady shear region, it continues to gain stretch at a linear rate, which again remains constant over the length of the lower steady shear region.

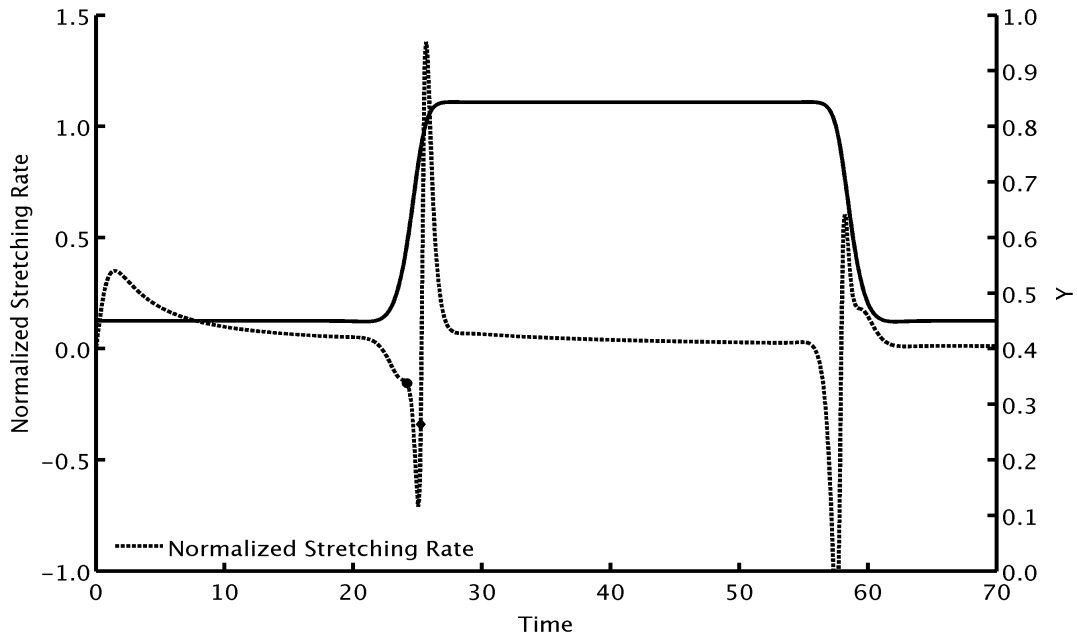


Figure 5.15: Lid Driven Cavity Normalized Material Stretching Rate for $y_0 = 0.45$

In the lower steady shear region, the material vector is found to have the highest normalized growth rate as it becomes parallel to the maximum eigenvector, and then begins to decay asymptotically to $\xi \rightarrow 0$ over time as the material vector asymptotically approaches the stable equilibrium orientation. In the upward flight, the

material vector is found to experience a slight decrease in growth rate (transitioning into an unfavorable orientation relative to the eigenvectors) as it begins to turn the corner. At the peak twirl time, the normalized growth rate is found to briefly remain constant as the maximum eigenvector orientation and material vector rotate concurrently. This is followed by a rapid decrease in normalized stretching rate. At the peak streamline curvature time, the normalized stretching rapidly changes from approximately $\xi = -0.71$ to $\xi = 1.38$, producing a rapid change in the normalized stretching rate of the material in this time. As the material vector enters the upper steady shear region, the normalized stretching rate asymptotically approaches zero due to shear stretching, although the resulting stretch rate (note, not the normalized stretch rate) is higher due to the greater shearing rate than the lower steady shear region. Upon entering the downward flight, material stretching reaches a local minimum normalized stretching rate of $\xi = -1.38$, at the maximum curvature time and a local maximum of $\xi = 0.71$ at the peak twirl time shortly after. The normalized stretching rate then begins to asymptotically approach $\xi \rightarrow 0$ as the material vector transitions into the lower steady shear region.

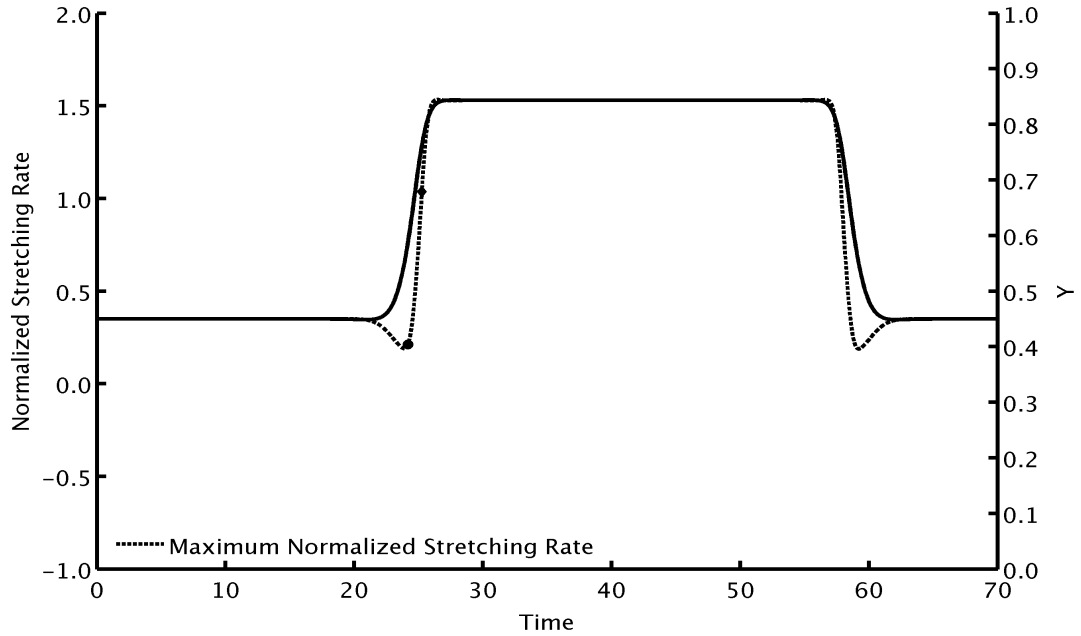


Figure 5.16: Lid Driven Cavity Maximum Normalized Material Stretching Rate for $y_0 = 0.45$

The maximum normalized stretching rate, shown above in Figure 5.16, remains constant throughout the lower steady shear region at $\dot{\epsilon} = \pm 0.35$. As the material vector entered the upward flight, the rate begins to decrease, reaching a local minimum of $\dot{\epsilon} = \pm 0.19$, and then begins to rapidly increase after the material vector element reaches peak twirl time. As the material vector is leaving the upward flight into the upper steady shear region, the maximum normalized stretching rate converges to a constant value of $\dot{\epsilon} = \pm 1.53$, which remains constant throughout the upper steady shear region. Upon entering the downward flight, the maximum normalized stretching rate begins to decrease, reaching a minimum of $\dot{\epsilon} = \pm 0.19$ before returning to the lower steady shear region value of $\dot{\epsilon} = \pm 0.35$, which remains constant throughout the region.

For consistency purposes, the normalized stretching rate was found to be bounded by the maximum normalized stretching rate at all times such that $|\xi| \leq \dot{\epsilon}$. This check

is necessary because a choice in time step δ_t that is too large can produce situations in which $|\xi| > \epsilon$, which is physically impossible.

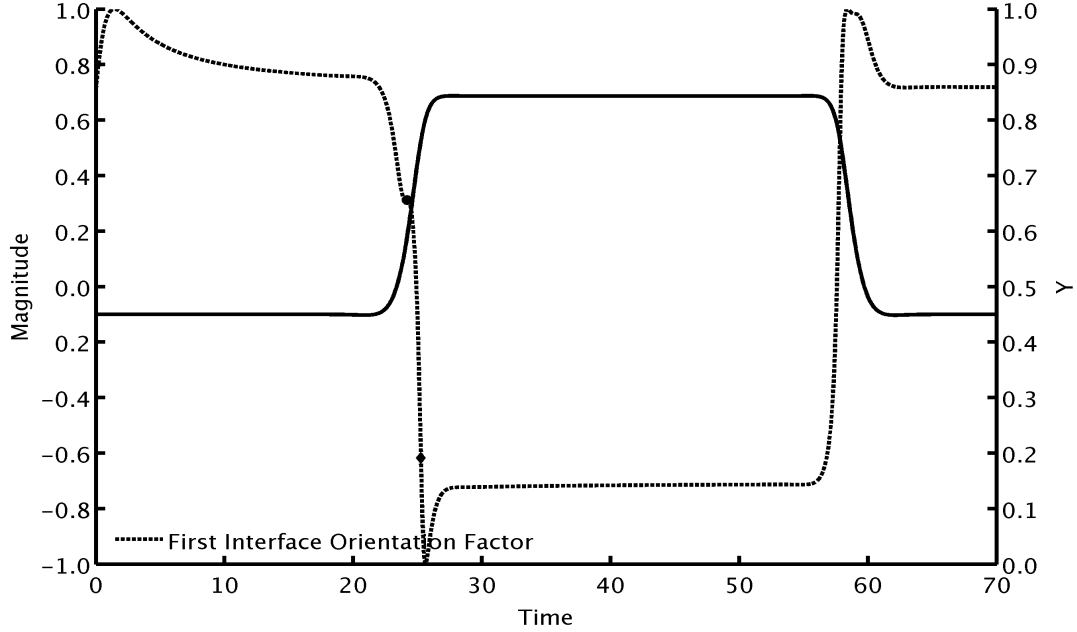


Figure 5.17: Lid Driven Cavity First Interface Orientation Factor for $y_0 = 0.45$

At simulation initialization, the material vector begins with a first interface orientation factor value of $O_p = 0.707$ (Figure 5.17). Shortly after, the value goes to $O_p = 1.000$ as the material vector orients parallel to the maximum eigenvector before returning to approximately $O_p = 0.707$ (that is, rotating from 45° counter-clockwise to 45° clockwise of the maximum eigenvector orientation), which is maintained throughout the upper steady shear region. At the entry to the upward flight at $t = 20.40$, the first interface orientation factor begins to decrease, rapidly approaching a local saddle point value of $O_p = 0.311$ at the peak twirl time, which is a result of the concurrent rotation between the maximum eigenvector and material vector orientations. After this time, the first interface orientation factor begins to rapidly decrease, reaching the maximum rate of change at the peak streamline time as a result of the rapid change of the material vector orientation relative to the maximum eigenvector orientation,

which can be readily seen in Figure 5.13. Shortly after, the first interface orientation factor reaches a minimum value of $O_p = -1.000$ before rapidly returning to the lower steady shear region value of approximately $O_p = -0.707$, which remains asymptotically fixed as the interface travels throughout the upper steady shear region. This value is consistent with the orientations observed in Figure 5.13, where the material vector and maximum eigenvector are oriented in the positive direction in the lower steady shear region and oriented in the opposite direction in the upper steady shear region. Upon entering the downward flight, the interface readily rotates to a value of $O_p = 1.000$, reaching its most rapid change at the maximum curvature time. A local first interface orientation factor saddle point is again reached at the peak twirl time. Following this, the first interface orientation factor returns to the the lower steady shear region value of $O_p = 0.707$, which remains constant throughout the lower steady shear region.

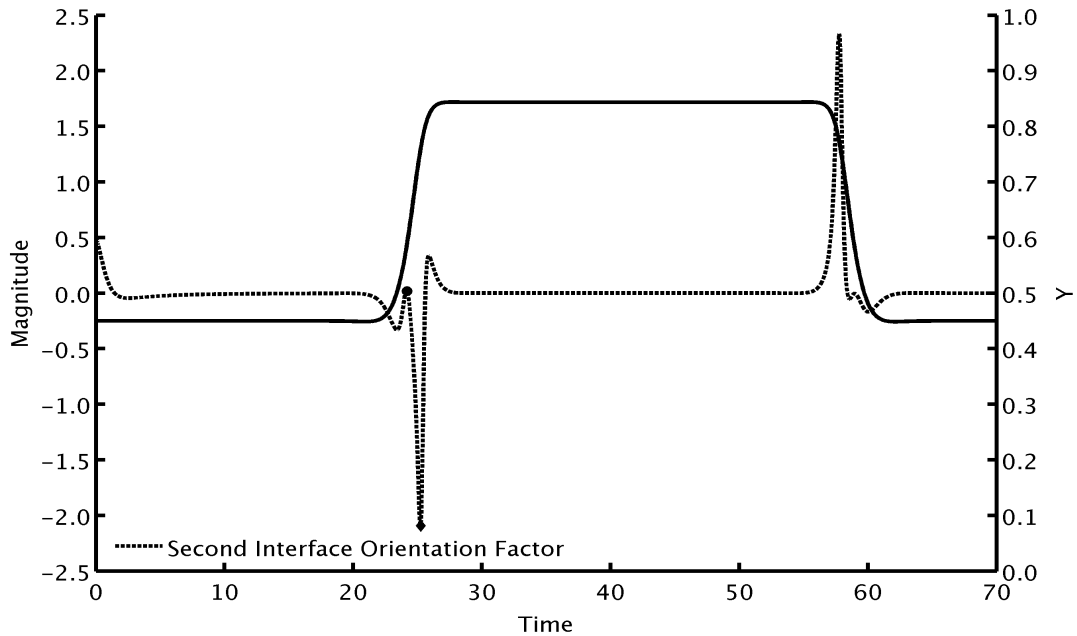


Figure 5.18: Lid Driven Cavity Second Interface Orientation Factor for $y_0 = 0.45$

Material element rotation behavior is most easily demonstrated using the second

interface orientation factor (Figure 5.18). In the lower steady shear region, the second interface orientation factor converges to approximately zero in a manner consistent with steady shear flow. Upon entering the upward flight, the second interface orientation factor becomes negative for a short time, reaching a local minimum of $\dot{O}_p = -0.3$ before returning to a value of $\dot{O}_p = 0$ at the peak twirl time (indicative of the concurrent rotation of the maximum eigenvector and rotation). Between the peak twirl and peak curvature times, the value of \dot{O}_p rapidly decreases to a minimum value of $\dot{O}_p = -2.116$ at the maximum curvature time. The second interface orientation factor value then briefly returns to positive before decaying asymptotically to zero again as the material vector enters and travels through the upper steady shear region. As the material element enters the downward flight, the second interface orientation factor reaches a maximum value of $\dot{O}_p = 2.116$ at the peak curvature time and again reaches a saddle point at the peak twirl time. Post exit into the lower steady shear region, the second interface orientation factor again asymptotically converges to zero (as the first interface orientation factor converges to $O_p = 0.707$). This value is maintained throughout the lower steady shear region.

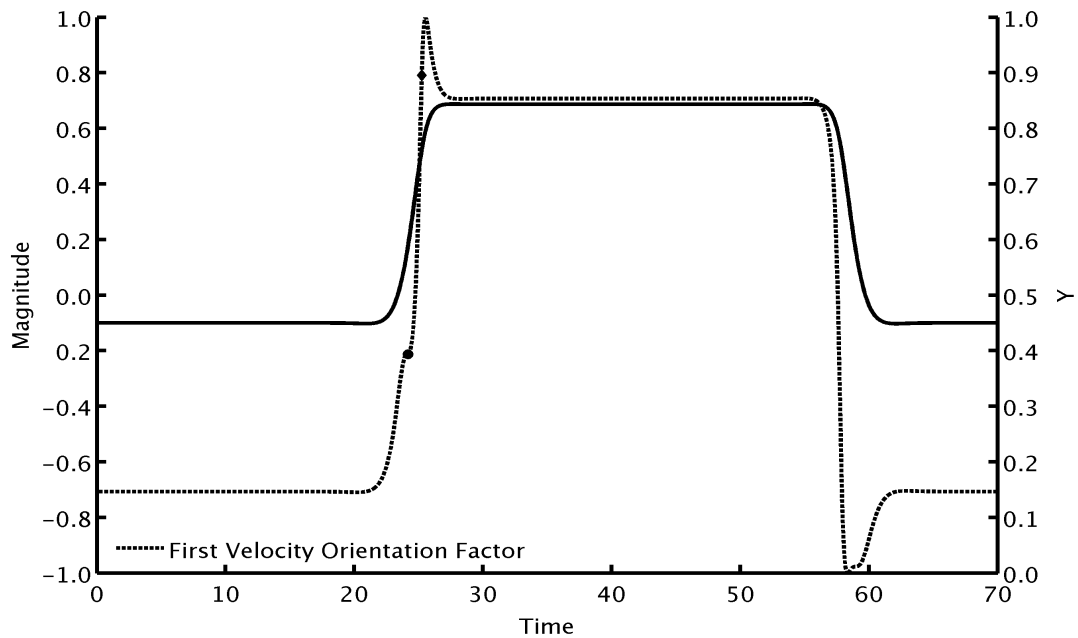


Figure 5.19: Lid Driven Cavity First Velocity Orientation Factor for $y_0 = 0.45$

Figure 5.19 shows that, in the lower steady shear flight, the first velocity orientation factor remains constant throughout the zone at a value of $O_u = -0.707$, consistent with behavior observed in steady shear. At the transition from the lower steady shear region into the upward flight, the material element approximately converges to the stable equilibrium orientation for shear, which results in approximately equivalent behavior between the first interface orientation factor and the first velocity orientation factor. This is maintained throughout the remainder of the simulation.

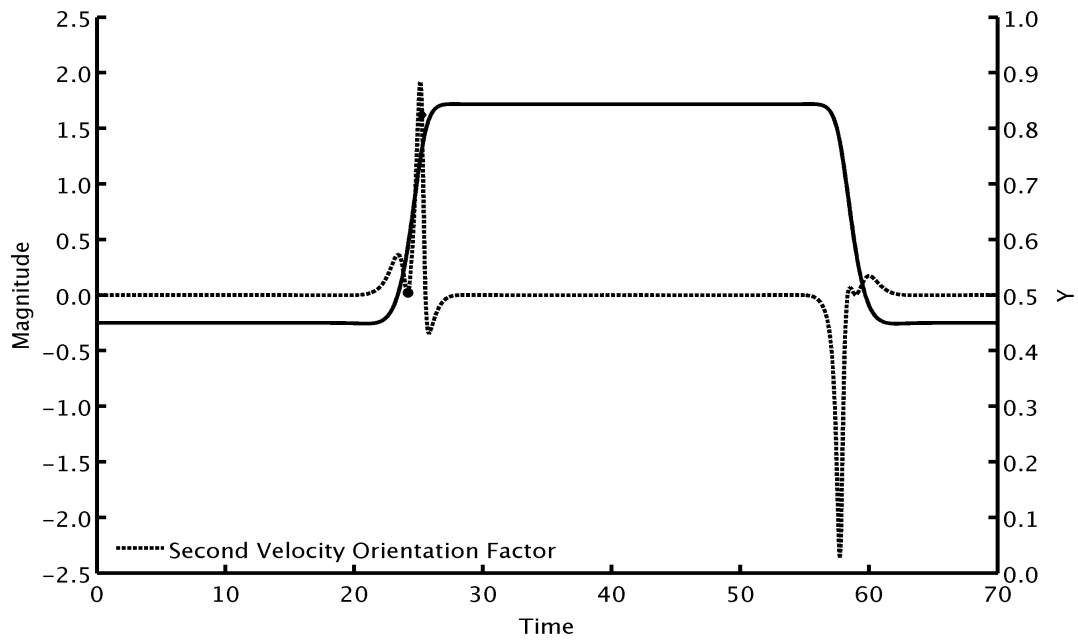


Figure 5.20: Lid Driven Cavity Second Velocity Orientation Factor for $y_0 = 0.45$

Figure 5.20 shows that, in the lower steady shear flight, the stable equilibrium orientation does not change in time and therefore has a value of $\dot{O}_u = 0$. At the transition from the lower steady shear flight, the material element has approximately converged to the stable equilibrium orientation for shear, so the second velocity orientation factor approximately follows the second interface orientation factor. This behavior is maintained throughout the remainder of the simulation.

5.3.2 Outer Streamline ($y_0 = 0.23$)

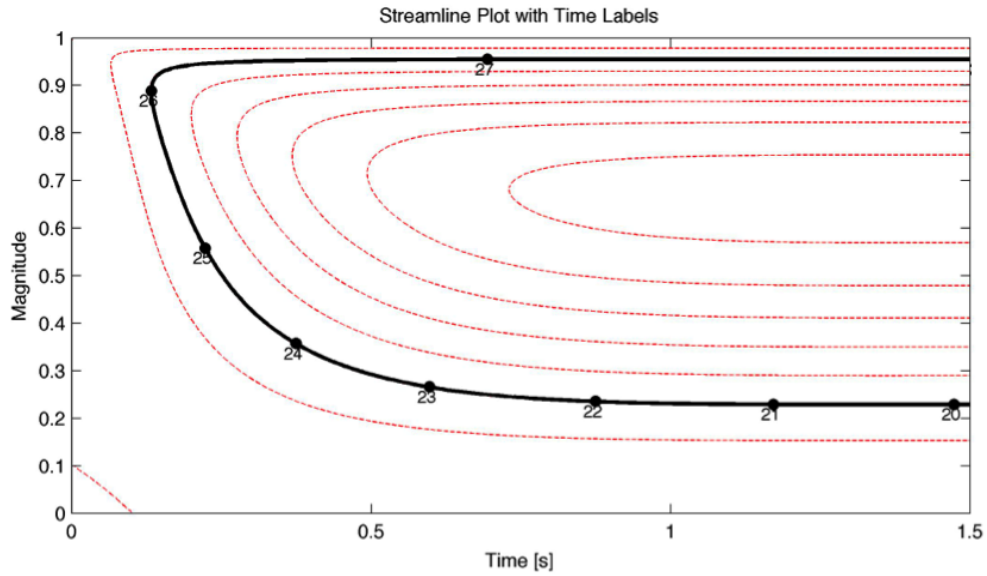


Figure 5.21: Lid Driven Cavity Interface Path for $y_0 = 0.23$

Material traveling on the outer streamline is defined by material with an initial spatial location of $\mathbf{x}_0 = \{7.50, 0.23\}$ and initial orientation $\mathbf{p}_0 = \{0, 1\}$. The material element \mathbf{p} transitions between the lower steady shear region and the upward flight at $t = 19.90s$, achieving its peak twirl value and maximum streamline curvature at $t = 25.79s$ and $t = 26.12s$ respectively and finally transitions from the upward flight into the upper steady state region at $t = 28.00s$. Later, the material element transitions the downward flight at $t = 42.48s$, achieving maximum streamline curvature at $t = 46.33s$, maximum twirl magnitude at $t = 47.98s$, and finally transitions into the lower steady shear region at $t = 50.54s$. The material vector completes one loop of the cavity in 70.45 seconds. Note that the outer streamline material vector travels around the cavity at a higher speed than the inner streamline. Note that this results in a higher shearing rate in both the lower and upper steady shear regions when compared to the

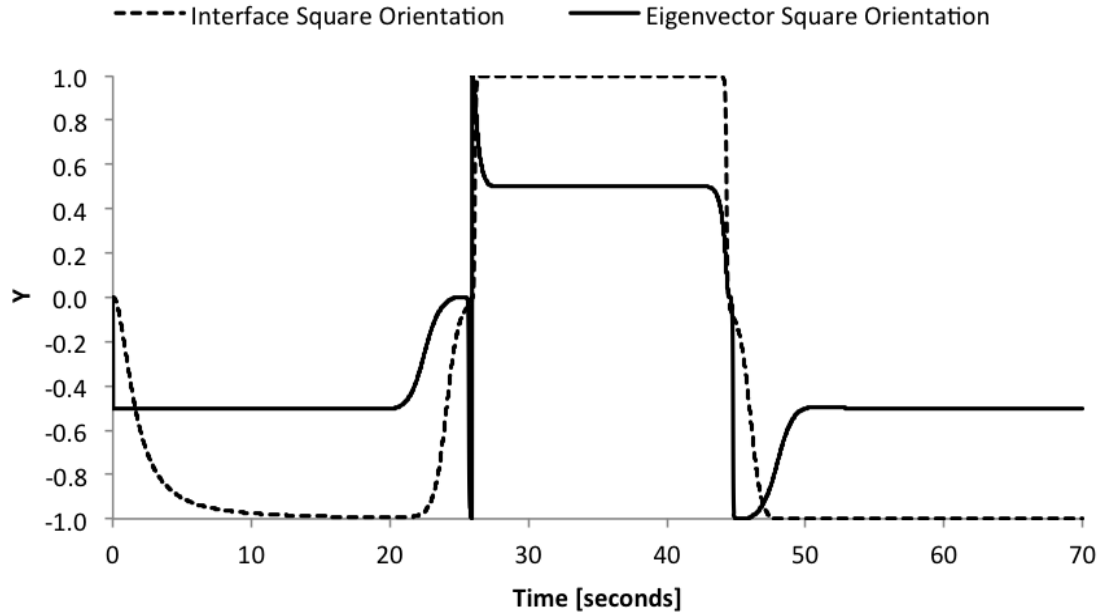


Figure 5.22: Lid Driven Cavity Square Orientation Plot for \mathbf{p} and \mathbf{d}_1 for $y_0 = 0.23$

In the lower steady shear region, the maximum eigenvector orientation remains fixed at $\Theta = -0.5$, consistent with a steady shear stretching regime (Figure B.26). At the entry to the upward flight, the maximum eigenvector begins rotating away from the horizontal reference direction. At the peak twirl time, the maximum eigenvector undergoes a rapid rotation, demonstrating a reorientation of the principal axis. At this time, the material vector does not undergo any significant change in orientation. Note that, unlike the transition through the upward flight on the inner streamline, the maximum eigenvector undergoes a flip from $\Theta = -0.5$ and $\Theta = 0.5$. At the exit from the upward flight, the maximum eigenvector has an orientation of $\Theta = 0.5$, consistent with steady shearing. This orientation remains fixed throughout the remainder of the upper steady shear region. Upon transition into the downward flight, the orientation of the maximum eigenvector begins to decay from $\Theta = 0.5$ towards $\Theta = -1$, rotating most rapidly at the downward flight peak twirl time. Once the maximum eigenvector orientation reaches $\Theta = -1$, it begins a less rapid rotation towards $\Theta = -0.5$ as it

transitions into the lower steady shear region. This orientation is again maintained throughout the region.

In the lower steady shear region, the material vector begins with an orientation of $\Theta = 0$. This corresponds to the initial orientation which is perpendicular to the streamline. The material vector then begins to orient to the zero-rotation orientation at $\Theta = -1$, parallel to the velocity orientation and in the opposite direction of the reference direction as a result of shearing. At the entry to the upward flight, the material vector begins to orient towards an orientation of $\Theta = 0$, followed by a very rapid rotation to $\Theta = -1$ at the maximum streamline curvature time. At the transition between the upward flight and upper steady shear region, the material vector achieved an orientation of $\Theta = 1$, parallel to both the velocity and reference direction, which remains constant throughout the upper steady shear region. Upon entering the downward flight, the interface again follows the stable equilibrium orientation and begins to rotate towards $\Theta = -1$, reaching its maximum rotation speed at the maximum streamline curvature time. At the transition into the lower steady shear region, the material vector has asymptotically reached an orientation of $\Theta = -1$, which is maintained throughout the lower steady shear region.

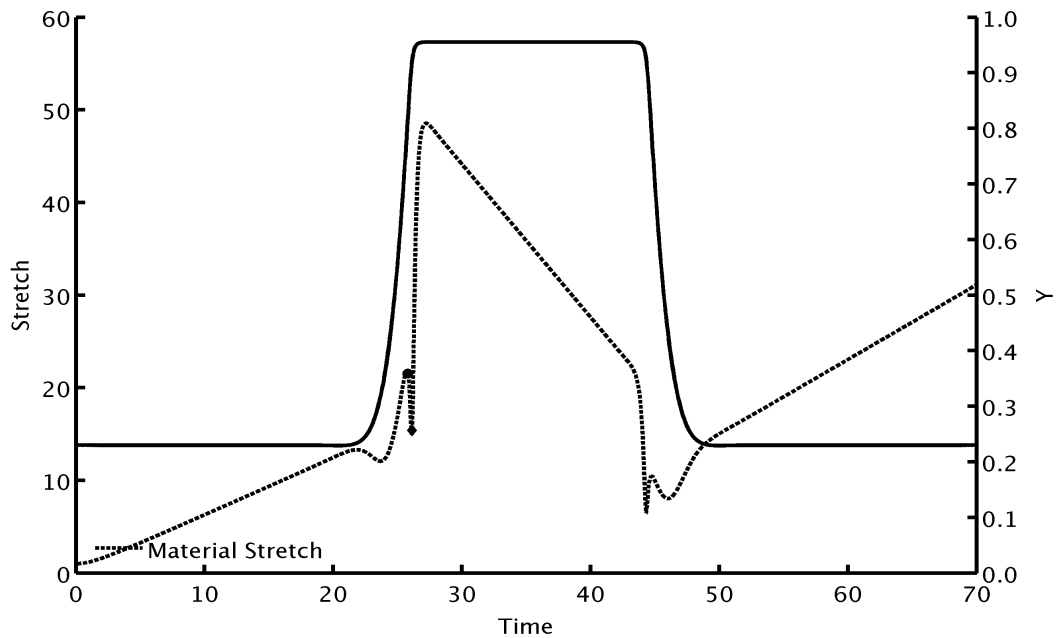


Figure 5.23: Lid Driven Cavity Material Stretch for $y_0 = 0.23$

The material stretch (Figure 5.23) rapidly converges to a steady shear growth rate (linearly increasing in time) in the lower steady shear region. At the entry to upward flight, the interface transitions into an unfavorable orientation (with a stretch of $ds = 13.30$ prior to loss) and then transitions back into a favorable orientation, losing a small amount of stretch in this period. At the peak twirl time, the material vector rapidly loses a large amount of stretch as a result of rapidly changing deformation directions relative to the unchanged material. Shortly after, the material then transitions into a favorable orientation and rapidly gains a large amount of stretch, with a maximum stretch of $ds = 49.07$. Between this short period of rapid gain and the exit from the upward flight into the upper steady shear region, the material becomes unfavorably oriented. Throughout the upper steady shear region, the material remains oriented unfavorably, losing stretch at an approximately linear rate. The material contracts to approximately half of its stretch at the start of the upper steady shear region before transitioning into the downward flight. The material continues to

remain unfavorably oriented at the transition into the downward flight with a stretch of $ds = 26.49$. Upon nearing the maximum curvature time, the material vector begins to rapidly lose stretch, reaching a local minimum of $ds = 8.72$, followed by a short gain and another period of loss, although at a slower rate than previously around the peak twirl time. Upon exit from the downward flight into the lower steady shear region, the interface has regained a favorable orientation and has begun to linearly stretch.

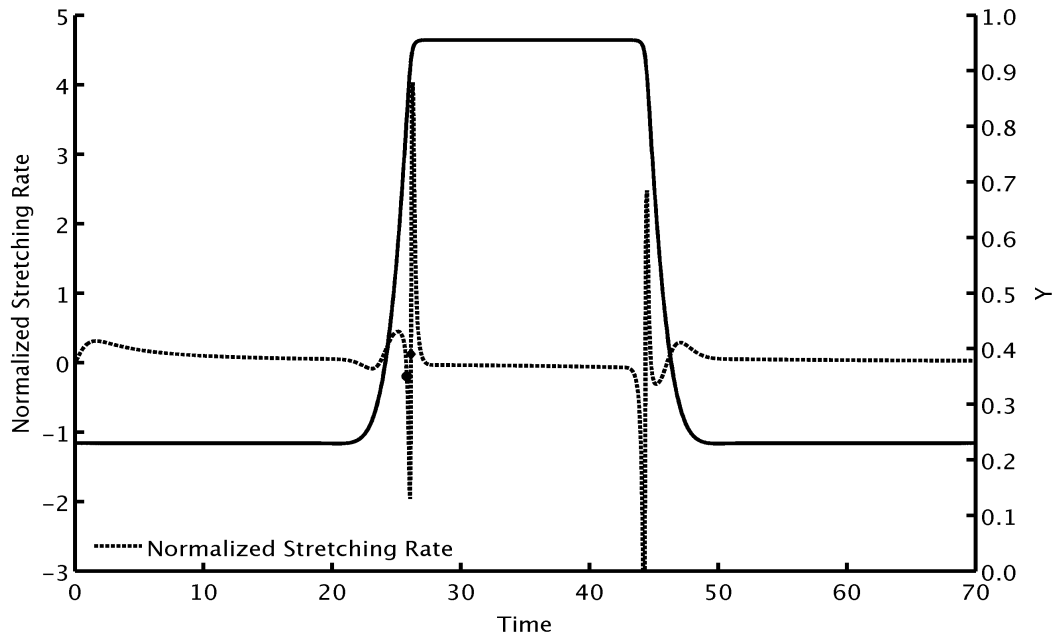


Figure 5.24: Lid Driven Cavity Normalized Material Stretch Rate for $y_0 = 0.23$

Normalized material stretch (Figure 5.3.2) shows similar trends to material stretch in Figure 5.23. In the lower steady shear region, the interface reaches its maximum local normalized stretch rate as it passes the maximum eigenvector direction. The normalized stretching rate then begins to decay asymptotically $\xi \rightarrow 0$ as the material asymptotically approaches the stable equilibrium orientation. At the transition into the upward flight, the normalized stretching begins to rapidly decrease, followed by a period of rapid changes. In this period, the normalized stretching rate reaches a local

minimum $\xi = -1.98$ and a local maximum of $\xi = 4.11$ at the peak twirl time and peak curvature times respectively. These rapid, high magnitude regions of growth rate produce the large increases in material stretch seen in Figure B.27. As the material exits the upward flight, the normalized stretching rate becomes negative and again begins asymptotically decaying to $\xi \rightarrow 0$. This behavior is continued throughout the upper steady shear region. Following transitioning into the downward flight, the material vector again undergoes two rapid changes in growth rate at the maximum streamline curvature and peak twirl times. At the transition from the downward flight to the lower steady shear region, the interface resumes stretching again with a positive, though asymptotically decaying, normalized stretching rate.

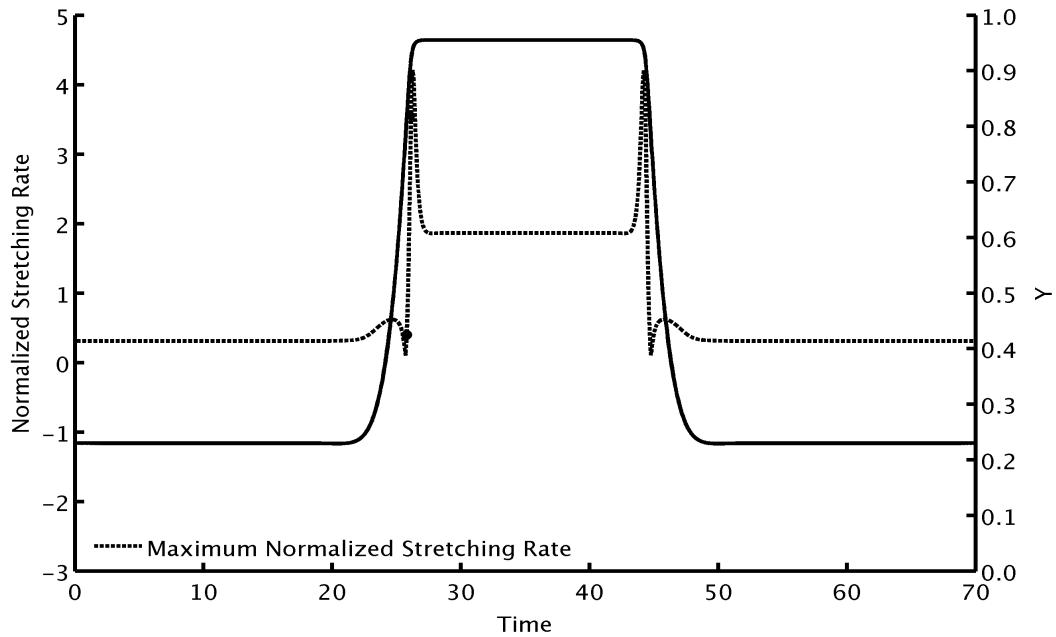


Figure 5.25: Lid Driven Maximum Normalized Material Stretching Rate for $y_0 = 0.23$

The maximum normalized stretching rate, shown above in Figure 5.25, remains constant throughout the lower steady shear region with a value of $\dot{\epsilon} = \pm 0.31$. As the material enters the upward flight, the rate $\dot{\epsilon}$ begins to increase followed by a somewhat rapid decrease, reaching a local minimum of $\dot{\epsilon} = \pm 0.10$, and then begins

to rapidly increase after the material vector passes the peak twirl time. $\dot{\epsilon}$ reaches a local maximum of $\dot{\epsilon} = \pm 4.21$ before rapidly decreasing to a steady shear maximum stretching rate. As the material vector is leaves the upward flight into the upper steady shear region, the maximum normalized stretching rate converges to a constant value of $\dot{\epsilon} = \pm 1.87$, which remains constant throughout the upper steady shear region. Once in the downward flight, the maximum normalized stretching rate rapidly reaches a peak value of $\dot{\epsilon} = \pm 4.21$ near the maximum streamline curvature time, followed by a rapid decay to a local minimum of $\dot{\epsilon} = \pm 0.10$, at the peak twirl time. This is followed by a short rebound which then decreases to a constant value of $\dot{\epsilon} = \pm 0.31$, which remains constant throughout the lower steady shear region. Again, for consistency purposes, the normalized stretching rate is found to be bounded by the maximum normalized stretching rate so that $|\xi| \leq \dot{\epsilon}$ at all times.

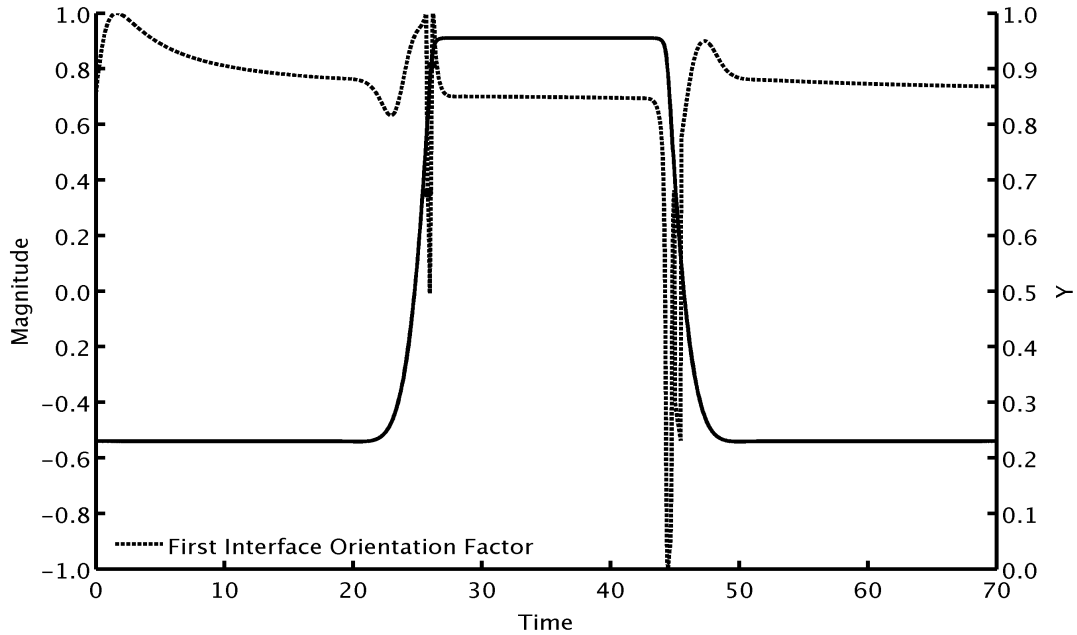


Figure 5.26: Lid Driven Cavity First Interface Orientation Factor for $y_0 = 0.23$

At time $t = 0$, the material element begins with an orientation of $\mathbf{p} = \{0, 1\}$, at a first interface orientation factor value of $O_p = 0.707$. (Figure 5.26) Shortly after,

the material element aligns with the maximum eigenvector \mathbf{d}_1 ($O_p = 0.707$) before asymptotically converging to the stable equilibrium orientation at $O_p = 0.707$. This steady state shear value is maintained throughout the lower steady shear region. The material element enters the upward flight approximately fully aligned to the shear orientation at a value of $O_p \approx 0.707$. Change in the material element orientation from the shearing orientation is observable as early as $t = 20.50$. At time $t = 25.60$, the interface instantaneously aligns to $O_p = 1.000$, followed by a transition to $O_p = 0.000$ at $t = 25.90$ and another rapid transition back to $O_p = 1.000$ at $t = 26.20$. The first and third change in this short period correspond to the peak twirl and peak curvature times respectively. After this time, first interface orientation factor converges rapidly $O_p \rightarrow 0.707$ which is maintained throughout the upper steady shear region. At the transition to the downward flight, rapid changes are observed again, similar to the changes found in the upward flight. At the exit into the lower steady shear region, the material element has again already converged asymptotically to the stable equilibrium orientation and remains so throughout the lower steady shear region.

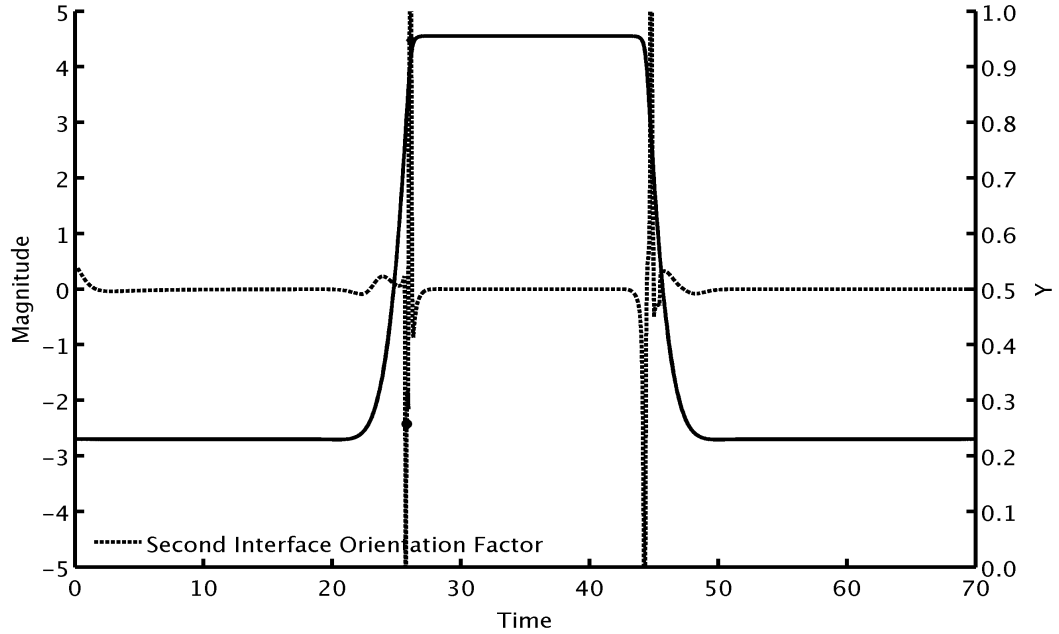


Figure 5.27: Lid Driven Cavity Second Interface Orientation Factor for $y_0 = 0.23$

At simulation initialization, the value of the first interface orientation factor rapidly converges to zero as a result of the asymptotic convergence of $O_p \rightarrow 0.707$. In the upward flight region, as seen in Figure B.30, instantaneously extensional stretching regimes are achieved at $t = 25.60$, $t = 25.90$, $t = 26.20$. These three times correspond to the local \dot{O}_p extrema. At both the twirl and curvature peaks, the \dot{O}_p value can be seen rapidly changing, with a minimum peak second interface orientation factor value of $\dot{O}_p = -9.004$ and a maximum peak \dot{O}_p value of 6.000 respectively. Note that, at the time which corresponds to an unstable equilibrium orientation, there is a slight redirection of the interface rotation followed by an extremely rapid change in the opposite direction. This is a result of the rapid reorientation of the interface as a result of acceleration in the velocity field. Upon entering the upper steady shear region, the value of the first interface orientation factor converges asymptotically to $\dot{O}_p \rightarrow 0$. As seen before in Figure 5.18, second interface orientation factor behavior in the downward flight is a mirror of behavior in the upward flight. However, for the inner

streamline, the values of the second interface orientation factor was opposite, whereas second interface orientation factor values are equivalent between upward and downward flights. This is very roughly related to the sign of shearing in the flow field, which is opposite between the inner and outer streamlines, $(\text{sgn}(\mathcal{W})_{inner} \propto -\text{sgn}(\mathcal{W})_{outer})$.

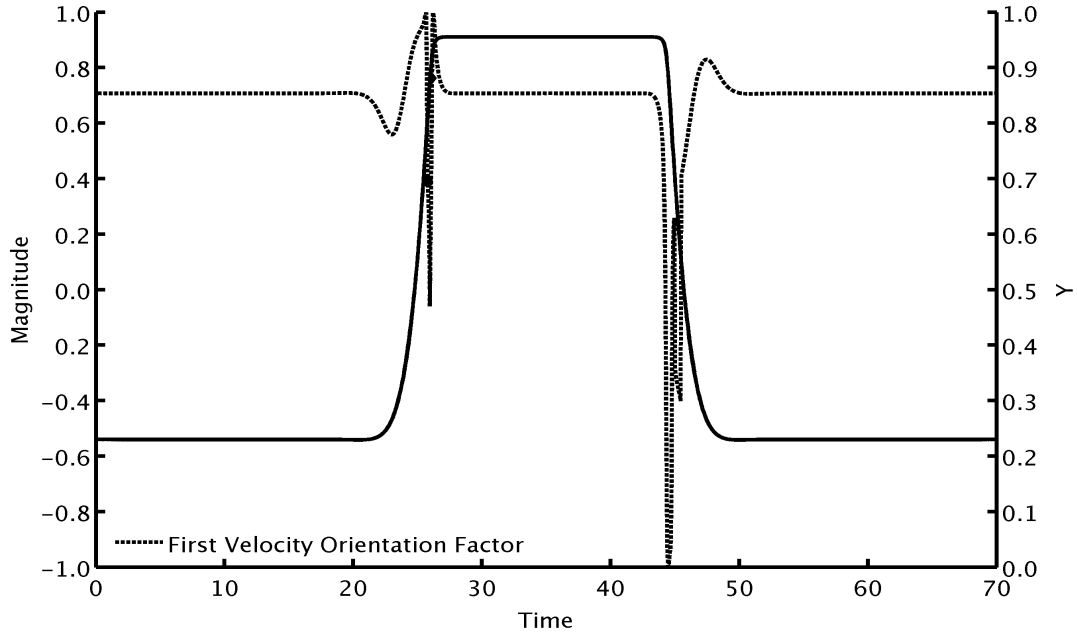


Figure 5.28: Lid Driven Cavity First Velocity Orientation Factor for $y_0 = 0.23$

In the lower steady shear flight, the first velocity orientation factor O_u is in a stable equilibrium orientation with a value of $O_u = 0.7071$. (Figure 5.28) This is consistent with results shown in the Couette channel. By the transition from the lower steady shear region into upward flight, the material element orientation has approximately converged to a stable equilibrium orientation. This results in nearly approximate convergence of the first interface orientation factor to the first velocity orientation factor. While the first velocity orientation factor values that are produced from this simulation are approximately identical throughout the remainder of the simulation, there is greater benefit to be had using this measure in fields in which the material element is exposed to flow in which no stable equilibrium orientation exists for long

periods of time and the interface is free to rotate and stretch in a wider variety of stretching regimes.

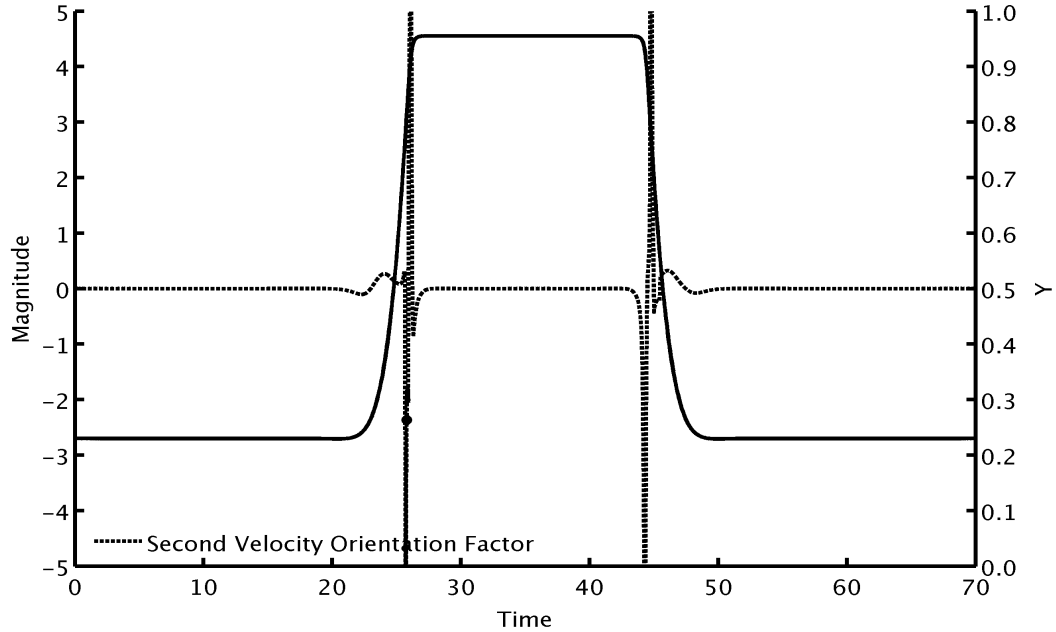


Figure 5.29: Lid Driven Cavity Second Velocity Orientation Factor for $y_0 = 0.23$

In the lower steady shear flight, the stable equilibrium orientation does not change in time, resulting in a second velocity orientation factor value of $\dot{O}_u = 0$. (Figure 5.29) At the transition from the lower steady shear flight, the material element has approximately converged to the stable equilibrium orientation, so the second velocity orientation factor approximately follows the second interface orientation factor. This remains true for the remainder of the simulation.

5.3.3 Twirl and Streamline Curvature Fields

Because both streamline curvature and twirl magnitude can be derived independently of material path, it is beneficial to explore the absolute magnitudes of these two parameters. Figure 5.30 shows the absolute magnitude of twirl. Figure 5.31 shows the absolute magnitude of streamline curvature. Finally, Figure 5.32 overlays Figure

5.31 onto Figure 5.31 for comparison. The values showed in these figures are calculated at each node of the velocity field solution. Color was added between nodes through interpolation.

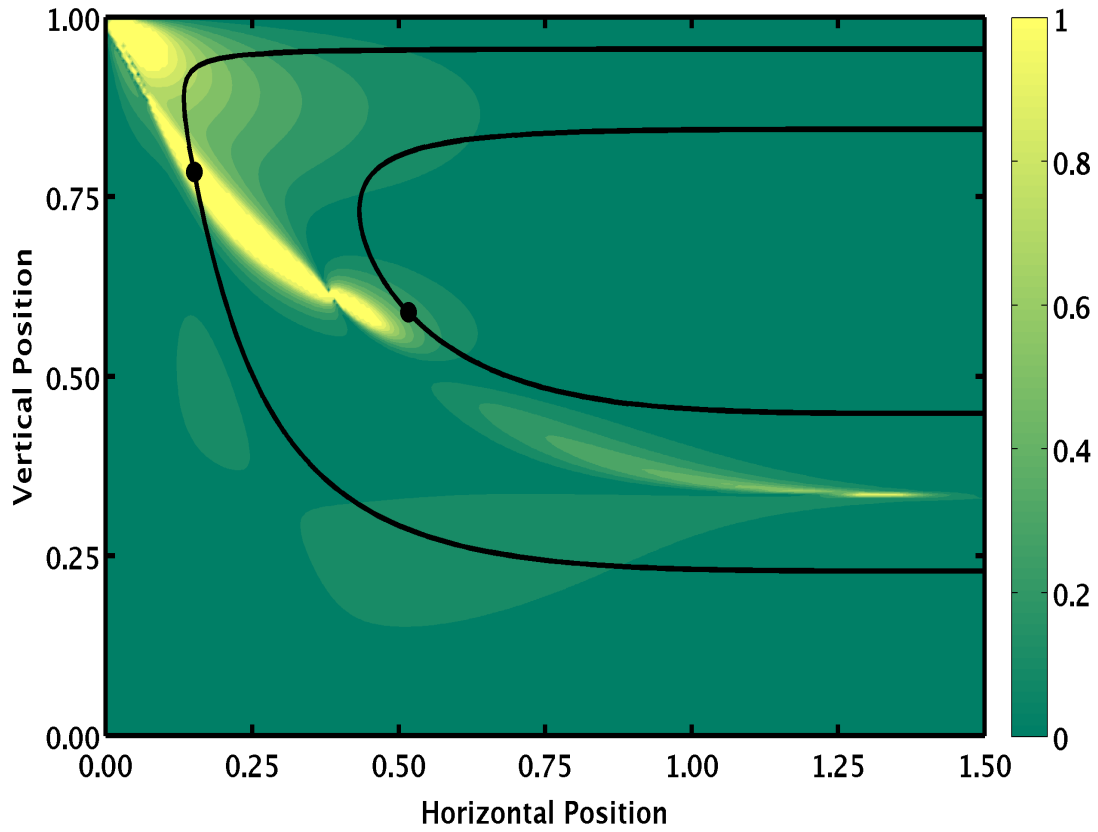


Figure 5.30: Lid Driven Cavity Upward Flight Twirl Contour

Note in Figure 5.30, any magnitude of twirl greater than one is set equal to one for presentation purposes.

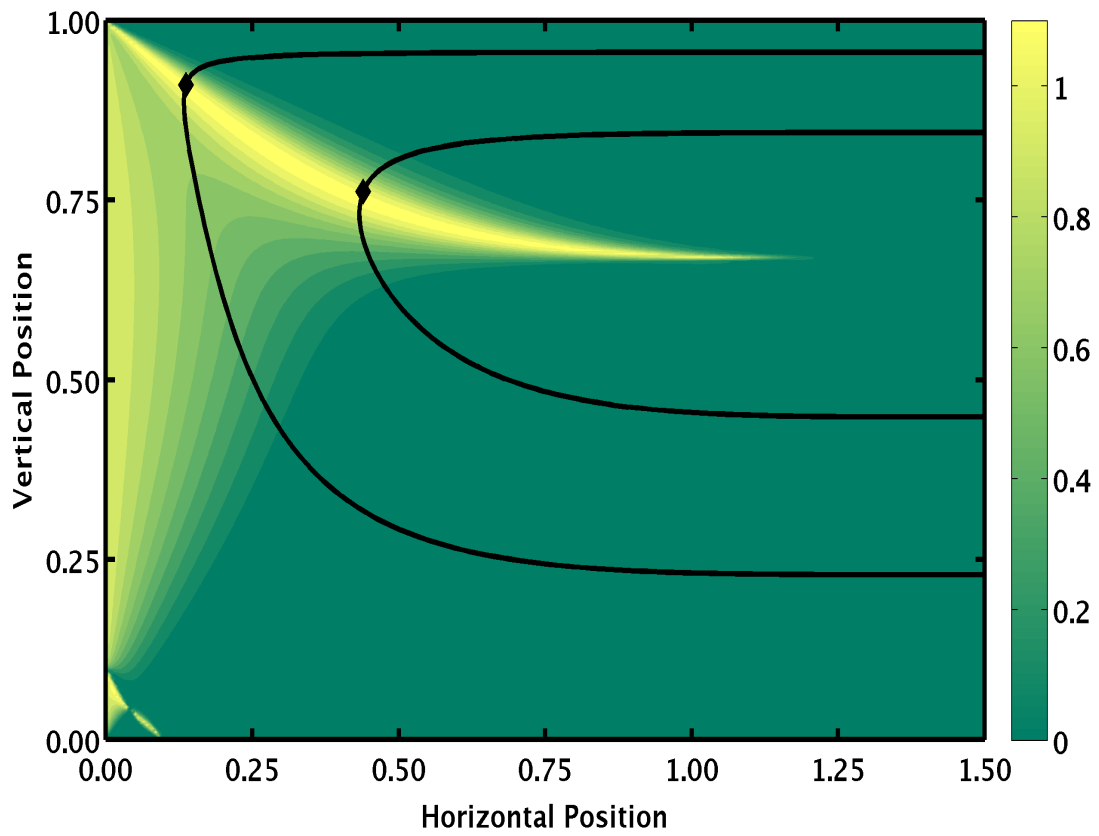


Figure 5.31: Lid Driven Cavity Upward Flight Streamline Curvature Contour

Note in Figure 5.30, any value of streamline curvature greater than one is set equal to one for presentation purposes.

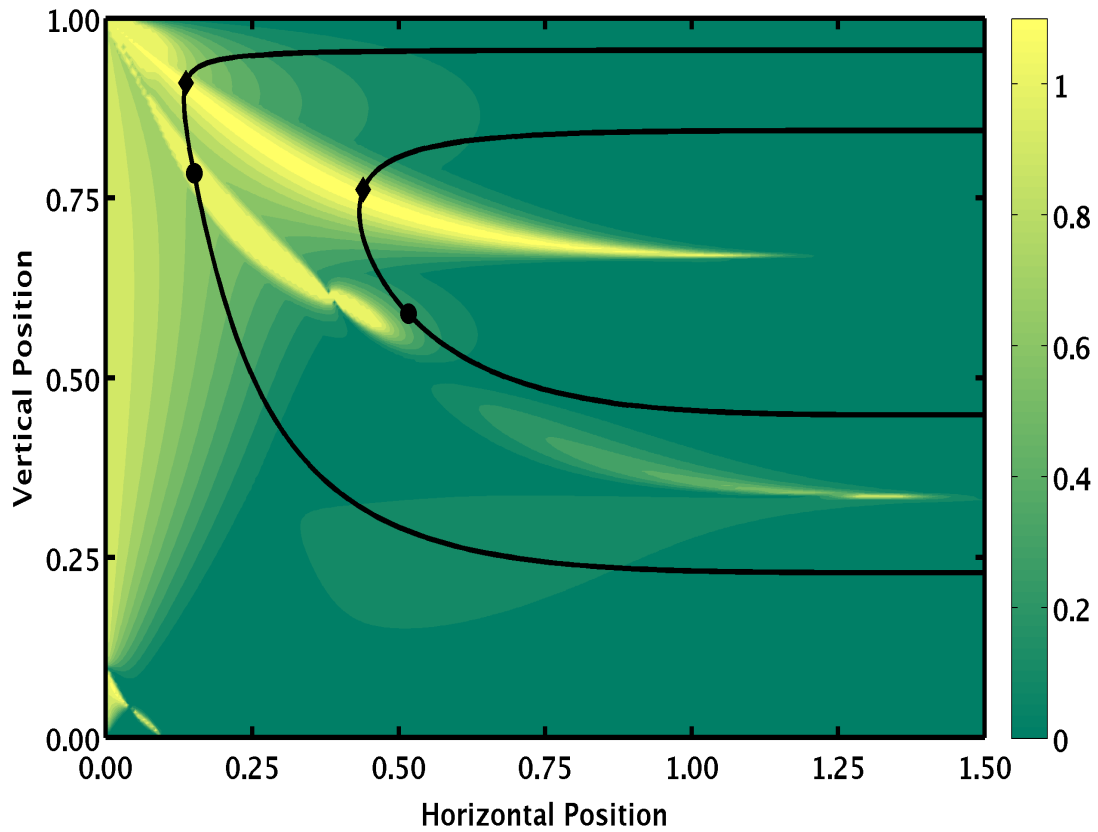


Figure 5.32: Lid Driven Cavity Upward Flight Twirl and Streamline Curvature Comparison

Figure 5.32 above shows the overlay of the absolute twirl tensor magnitude and the absolute streamline curvature. This contour plot was created to show the most rapid change in the eigenvector orientation (associated with high twirl magnitudes) and rapid change in the material orientation (associated with high streamline curvature values). There are two ridges indicating high values in the upward flight. Comparison of Figure 5.30 to Figure 5.31 shows that the maximum twirl occurs separately and prior to the maximum curvature zone. The reverse is true in the downward flight. Because of this two rapid changes in orientation (associated with first the eigenvectors and later with the material), significant improvements in stretching can be found at these zones.

Chapter 6: Conclusions

6.1 Conclusions

Two sets of measures were derived that give further insight into continuum laminar mixing. The measures are divided into interface measures and shear-equilibrium (velocity) measures. These expressions compare material orientations against the maximum rate of deformation tensor eigenvector \mathbf{d}_1 , which are the mechanisms of a deformation in a flow, an indicator of the amount of stretching received by the material. The former expressions, the interface orientation factors, compare the orientation of a material interface element to the eigenvector. The latter expressions relate the shear-equilibrium orientation, or more formally the orientations at which a material vector does not deform in a shear field (parallel to the shearing direction) and at which all other material orientations converge, to the maximum eigenvector \mathbf{d}_1 . These measures characterize a range of material stretching regimes including pure-shear, pure-extensional, mixed shear-extensional, and spatially variant flows (where $\|\mathcal{T}\| \neq 0$, i.e. flows in which $\{\mathbf{d}_1, \mathbf{d}_2\}$ rotate in space along streamlines). Analysis of these measures in flow field models was accomplished using 2D simulations for the Couette channel, the diverging channel, and the lid driven cavity flow field.

These new measures are named the first interface orientation factor O_p , the second interface orientation factor \dot{O}_p , the first velocity orientation factor O_u , and the second velocity orientation factor \dot{O}_u . These measures were named with respect to the orientation to be compared against \mathbf{d}_1 and the level of time dependence, that is the second orientation factor is the material derivative of the first orientation factor. The first interface orientation factor and first velocity orientation factors are defined as:

$$O_p = \mathbf{p} \cdot \mathbf{d}_1 \tag{6.1.1}$$

$$O_u = \mathbf{u} \cdot \mathbf{d}_1 \quad (6.1.2)$$

First orientation factor measures O_p and O_u relate the degree of alignment between the orientations of interest (\mathbf{p} and \mathbf{u}) and the maximum eigenvector \mathbf{d}_1 and therefore the ratio of stretching to maximum possible stretching (locally) experienced by a material in this orientation. With this definition, the ratio of the experienced normalized stretching rate to the maximum normalized stretching rate is expressed at any point in the material stretching history as a function of the O_p . Furthermore, O_p can be substituted into several existing stretching efficiency measures, producing simplified expressions as a function of O_p which effectively further demonstrates the relationship between material orientation and the eigenvectors of the deformation tensor. Using these properties of O_p , the kinematical simplifications presented by Spencer and Wiley and Erwin can be expressed as a function of the mixing mechanisms in the fluid.

Further information about a flow can also be gained by the application of the first velocity orientation factor O_u , which is an expression of the long time material orientation in a shear flow (parallel to the velocity and the shearing orientation) to the maximum eigenvector \mathbf{d}_1 , to a streamline. In the pure-shear case $O_u = 0.7071$, which corresponds to a constant stretching rate $d\dot{s} = 0$. In the pure-extensional case $O_u = 1.0000$, which corresponds to a stretching rate of $d\dot{s} = \dot{\epsilon}ds$. With these values for reference, the ratio of shear to extensional deformation can be expressed, which is important for the characterization of material stretching along streamlines in diverging and converging channels where there both shearing and extensional flow character is present. Additionally, O_u can be used to test for changes in stretching regimes through the observation of changes in the velocity-eigenvector orientation value along a streamline. As expected, for a flow where a fluid element spends a significant amount of time on a streamline with zero twirl ($\dot{\mathbf{d}}_1 = \mathbf{0}$), the first interface factor converges to the value of the first velocity orientation factor ($O_p \rightarrow O_u$), illustrating

why over long times pure-shear material stretching is poor and pure-extensional is optimal for stretching. By extension, this property of O_p and O_u demonstrates the need for periodic reorientation of the intermaterial interface relative to the principal directions to produce improved mixing.

The second orientation factor measures \dot{O}_p and \dot{O}_u , the material derivatives of O_p and O_u respectively, are defined as follows:

$$\dot{O}_p = \mathbf{d}_1 \cdot [\mathcal{D} - (\mathbf{p} \cdot \mathcal{D} \cdot \mathbf{p})\mathcal{I} + \mathcal{W} - \mathcal{T}] \cdot \mathbf{p} \quad (6.1.3)$$

$$\dot{O}_u = \mathbf{d}_1 \cdot [\mathcal{D} - (\mathbf{u} \cdot \mathcal{D} \cdot \mathbf{u})\mathcal{I} + \mathcal{W} - \mathcal{T}] \cdot \mathbf{u} \quad (6.1.4)$$

Note that the second orientation factor expressions are composed of the maximum eigenvector \mathbf{d}_1 , the rate of deformation tensor \mathcal{D} , the vorticity tensor \mathcal{W} , the new tensor twirl \mathcal{T} and the test orientation. Twirl \mathcal{T} is an expression for the instantaneous rate of change of the eigenvectors $\{\mathbf{d}_1, \mathbf{d}_2\}$ in space. The tensor \mathcal{T} , which is derived in Section 3.2 and more thoroughly in Appendix A, is a function of the rate-of-deformation tensor \mathcal{D} , the material derivative of the rate-of-deformation $\dot{\mathcal{D}}$, and the maximum normalized stretching rate $\dot{\epsilon}$.

$$\mathcal{T} = \frac{\dot{\mathcal{D}} \cdot \mathcal{D} - \mathcal{D} \cdot \dot{\mathcal{D}}}{4\dot{\epsilon}^2} \quad (6.1.5)$$

In the case of discontinuous velocity fields, the velocity profile in a region can change instantaneously. This infinite change invalidates assumptions about the presence of spatial variance. While this does preclude the application, or at least require piecewise treatment, of the twirl tensor and, by extension, the orientation factor measures to discrete flows like the twin blinking vortex flow used by Aref [1] for the demonstration of chaotic advection, they can be readily applied to the transient solutions for such fields. Second, the presence of non-zero spatial variance along a streamline is indicative of change in the stretching regime, although the presence of twirl does not indicate the initial or final stretching regime.

Second orientation factors \dot{O}_p and \dot{O}_u express the rate at which the material element and the velocity orientations are changing with respect to the maximum eigenvector \mathbf{d}_1 , which itself may be changing in space resulting from spatial variance. In a flow, changes in maximum eigenvector orientation relative to the material vector orientation can lead to higher than linear stretching rates. In these regions, where $\|\mathcal{T}\| \neq 0$, the resulting change in normalized stretching rate ξ and, therefore, changes in the stretch ds can be large with greater twirl leading to potentially greater change. The second interface orientation factor O_p expresses the rate at which the interface approaches or moves away from \mathbf{d}_1 towards its instantaneous velocity alignment. The second velocity orientation factor O_u expresses the rate at which the stable equilibrium orientation changes in space relative to \mathbf{d}_1 , illuminating changes in flow regime.

The application of these measures is best demonstrated in the lid driven cavity simulation results presented in Section 5.3. On both streamlines, though more prevalent along $h_0 = 0.23$, two critical times were observed with rapid changes in the interface/velocity-eigenvector spatial relationship. The latter of these occurred at the maximum streamline curvature, at which the velocity orientation changes most quickly and the eigenvector set less so. The former of these times occurred at the peak twirl value, located well before the maximum streamline curvature, where the fluid acceleration reaches its greatest change. This time was denoted as the peak twirl time. At this time, the eigenvector set rotates rapidly with little observable change in the interface. These phenomenon were observed on all streamlines in this cavity. At both of these critical times, significant changes in the local scaled stretching rate were observed. This is critical to improved mixing. At moments of rapid changes in the eigenvectors, or the material relative to the eigenvectors, greater than linear rates of stretching are found. By the definition of mixing proposed by Spencer and Wiley, increases in intermaterial area generated by these greater than linear rates will lead to improved mixing. By manipulating these regions, improved mixing can be

produced in what was thought to ineffective mixing systems.

Expressions were derived for the evaluation of interface stretching (and therefore mixing) in continuous laminar flows using the eigenvectors of the rate of deformation tensor as a basis. Use of the eigenvectors greatly extends the understanding of mixing phenomenon. The eigenvectors, which are calculated as a function of the rate of deformation tensor, are the mechanisms for fluid deformation. Using the principal directions, intuitive and new insights into the mixing in a cavity are demonstrated.

6.2 Recommendation for Future Work

Future work could be directed along several directions of the concepts presented.

First, derivation of the twirl tensor and the orientation factor measures assumes that all transient terms, that is, any terms which are dependent on time, are zero because all flow field models are steady state. However, this will rarely be the case in realistic mixing situations. Therefore, the first step in future development of this work will be to re-derive twirl and orientation factors to include transient terms. This allows for transient flows, and more specifically, spatially and temporally continuous chaotic flow field models to be explored. An exploration of chaotic flows could potentially reveal additional phenomenon in chaotic flows that can be exploited to produce even greater mixing.

Next, future work would progress in the three dimensional real, again with the inclusion of transient terms. While the two dimensional flows examined in this study are critical to investigating fundamental flow behavior, they do not fully explore area deformation and some three dimensional mixing phenomenon. Expansion into three dimensions open possibilities for the exploration of realistic mixing simulations. Furthermore, the actual generation of the velocity field solutions is not important to the study of twirl and orientation factors. Therefore, complex velocity field solutions produced by other authors could be used, reducing research time by jumping im-

mediately to analysis rather than the overhead time spent developing velocity fields. Furthermore, very complex velocity fields could be used, such as a single screw, twin screw, or Kinex twisted tape mixer, which are outside of available computational resources to perform in house. Using the work in three dimensions, the fundamentals of interface reorientation in realistic flows can be explored, shedding new light on real mixing phenomenon.

Finally, a divergent path for future work considers investigating the form of swirl which can be derived by removing assumptions about incompressibility, miscibility, or other constitutive laws. This work could be pursued in both two dimensional and three dimensional flows.

Appendix A: Twirl Tensor Derivation

Consider the tensor \mathcal{T} which is defined as the mapping of the eigenvectors of the rate of deformation tensor to the material derivative of the eigenvectors of the rate of deformation tensor.

$$\dot{\mathbf{e}}_1 = \mathcal{T} \cdot \mathbf{e}_1 \quad (\text{A.0.1})$$

Prior to the actual twirl tensor derivation, an identity used in its derivation will be derived. Begin with the rate of deformation tensor \mathcal{D} , its associated eigenvector-eigenvalue pairs $\{\mathbf{d}_i, \lambda_i\}$, and an arbitrary tensor \mathcal{A} .

$$\begin{aligned} \mathcal{A}\mathcal{D} - \mathcal{D}\mathcal{A} &= \sum_{a,b} \left[\sum_i [\mathcal{A}_{ai}(\mathbf{d}_a \otimes \mathbf{d}_i) \lambda_b \delta_{ib}(\mathbf{d}_i \otimes \mathbf{d}_b)] \right. \\ &\quad \left. - \sum_i [\mathcal{A}_{ib}(\mathbf{d}_i \otimes \mathbf{d}_b) \lambda_a \delta_{ai}(\mathbf{d}_a \otimes \mathbf{d}_i)] \right] \end{aligned} \quad (\text{A.0.2})$$

$$\begin{aligned} \mathcal{A}\mathcal{D} - \mathcal{D}\mathcal{A} &= \sum_{a,b} [\mathcal{A}_{ab}(\mathbf{d}_a \otimes \mathbf{d}_b) \lambda_b \delta_{bb}(\mathbf{d}_b \otimes \mathbf{d}_b) \\ &\quad - \mathcal{A}_{ab}(\mathbf{d}_a \otimes \mathbf{d}_b) \lambda_a \delta_{aa}(\mathbf{d}_a \otimes \mathbf{d}_a)] \end{aligned} \quad (\text{A.0.3})$$

$$\mathcal{A}\mathcal{D} - \mathcal{D}\mathcal{A} = \sum_{a,b} [\mathcal{A}_{ab} [\lambda_b(\mathbf{d}_b \otimes \mathbf{d}_b) - \lambda_a(\mathbf{d}_a \otimes \mathbf{d}_a)] (\mathbf{d}_a \otimes \mathbf{d}_b)] \quad (\text{A.0.4})$$

$$\mathcal{A}\mathcal{D} - \mathcal{D}\mathcal{A} = \sum_{a,b} [\mathcal{A}_{ab} [\lambda_b - \lambda_a] (\mathbf{d}_a \otimes \mathbf{d}_b)] \quad (\text{A.0.5})$$

To begin defining twirl, start with the following expressions for the rate of deformation tensor \mathcal{D} , the rate of deformation material derivative $\dot{\mathcal{D}}$, and the twirl tensor \mathcal{T} .

$$\mathcal{D} = \sum_i \lambda_i \mathbf{d}_i \otimes \mathbf{d}_i = \sum_{a,b} \lambda_a \delta_{ab} \mathbf{d}_a \otimes \mathbf{d}_b \quad (\text{A.0.6})$$

$$\dot{\mathcal{D}} = \sum_{a,b} \dot{\mathcal{D}}_{ab} \mathbf{d}_a \otimes \mathbf{d}_b \quad (\text{A.0.7})$$

$$\mathcal{T} = \sum_{a,b} \mathcal{T}_{ab} \mathbf{d}_a \otimes \mathbf{d}_b \quad (\text{A.0.8})$$

Furthermore, assume that the eigenvalues of the rate of deformation tensor assume the form of $\lambda_1 = \dot{\epsilon}$ and $\lambda_2 = -\dot{\epsilon}$, where $\dot{\epsilon} = \sqrt{\mathcal{D} : \mathcal{D}}$. To start the definition, begin by taking the material derivative of the rate of deformation tensor definition.

$$\dot{\mathcal{D}} = \sum_i \dot{\lambda}_i \mathbf{d}_i \otimes \mathbf{d}_i + \lambda_i \dot{\mathbf{d}}_i \otimes \mathbf{d}_i + \lambda_i \mathbf{d}_i \otimes \dot{\mathbf{d}}_i \quad (\text{A.0.9})$$

$$= \sum_i \dot{\lambda}_i \mathbf{d}_i \otimes \mathbf{d}_i + \lambda_i (\mathcal{T} \cdot \mathbf{d}_i) \otimes \mathbf{d}_i + \lambda_i \mathbf{d}_i \otimes (\mathcal{T} \cdot \mathbf{d}_i) \quad (\text{A.0.10})$$

$$= \sum_i \dot{\lambda}_i \mathbf{d}_i \otimes \mathbf{d}_i + \mathcal{T} \cdot (\lambda_i \mathbf{d}_i \otimes \mathbf{d}_i) - (\lambda_i \mathbf{d}_i \otimes \mathbf{d}_i) \cdot \mathcal{T} \quad (\text{A.0.11})$$

$$= \mathcal{T} \cdot \mathcal{D} - \mathcal{D} \cdot \mathcal{T} + \sum_i \dot{\lambda}_i \mathbf{d}_i \otimes \mathbf{d}_i \quad (\text{A.0.12})$$

$$= \sum_{a,b} \dot{\lambda}_a \delta_{ab} \mathbf{d}_a \otimes \mathbf{d}_b + \mathcal{T}_{ab} (\lambda_b - \lambda_a) (\mathbf{d}_a \otimes \mathbf{d}_b) \quad (\text{A.0.13})$$

$$= \sum_{a,b} \left(\dot{\lambda}_a \delta_{ab} + \mathcal{T}_{ab} (\lambda_b - \lambda_a) \right) (\mathbf{d}_a \otimes \mathbf{d}_b) \quad (\text{A.0.14})$$

Substituting the alternative definition of the rate of deformation material derivative yields:

$$\sum_{a,b} \mathcal{D}_{ab} \mathbf{d}_a \otimes \mathbf{d}_b = \sum_{a,b} \left(\dot{\lambda}_a \delta_{ab} + \mathcal{T}_{ab} (\lambda_b - \lambda_a) \right) (\mathbf{d}_a \otimes \mathbf{d}_b) \quad (\text{A.0.15})$$

Removing the summations, eigenvector tensor product, and further equation manipulation yields:

$$\mathcal{T}_{ab} = \frac{\dot{\mathcal{D}}_{ab} - \dot{\lambda}_a \delta_{ab}}{(\lambda_b - \lambda_a)} \quad (\text{A.0.16})$$

For the case of $a = b$, the numerator goes to zero ($\dot{\mathcal{D}}_{aa} = \dot{\lambda}_a$). In the case $a \neq b$, the $\dot{\lambda}_a$ term vanishes. Equation (A.0.16) can then be simplified and solved only for the case where $a \neq b$. Multiplication of the numerator and denominator of equation

(A.0.18) by $\lambda_b - \lambda_a$ yields:

$$\mathcal{T}_{ab} = \frac{\dot{\mathcal{D}}_{ab} \lambda_b - \lambda_a}{\lambda_b - \lambda_a \lambda_b - \lambda_a} \quad (\text{A.0.17})$$

$$= \frac{1}{(\lambda_b - \lambda_a)^2} \left[\dot{\mathcal{D}}_{ab} (\lambda_b - \lambda_a) \right] \quad (\text{A.0.18})$$

Expanding equation (A.0.18) into its summation form yields:

$$\sum_{a \neq b} \mathcal{T}_{ab} \mathbf{d}_a \otimes \mathbf{d}_b = \sum_{a \neq b} \frac{1}{(\lambda_b - \lambda_a)^2} \left[\dot{\mathcal{D}}_{ab} (\lambda_b - \lambda_a) \right] \mathbf{d}_a \otimes \mathbf{d}_b \quad (\text{A.0.19})$$

Substituting the eigenvalues of λ_1 and λ_2 yields:

$$\sum_{a \neq b} \mathcal{T}_{ab} \mathbf{d}_a \otimes \mathbf{d}_b = \frac{1}{4\dot{\epsilon}^2} \sum_{a \neq b} \left[\dot{\mathcal{D}}_{ab} (\lambda_b - \lambda_a) \right] \mathbf{d}_a \otimes \mathbf{d}_b \quad (\text{A.0.20})$$

Finally, application of the identity (A.0.5) to (A.0.20) yields the final form of twirl given below:

$$\mathcal{T} = \frac{\dot{\mathcal{D}} \cdot \mathcal{D} - \mathcal{D} \cdot \dot{\mathcal{D}}}{4\dot{\epsilon}^2} \quad (\text{A.0.21})$$

Appendix B: Supplementary Figures

B.1 Diverging Channel with $\theta \rightarrow \alpha$

Additional simulations using the diverging channel flow field model were conducted to show material orientation behavior near the boundary.

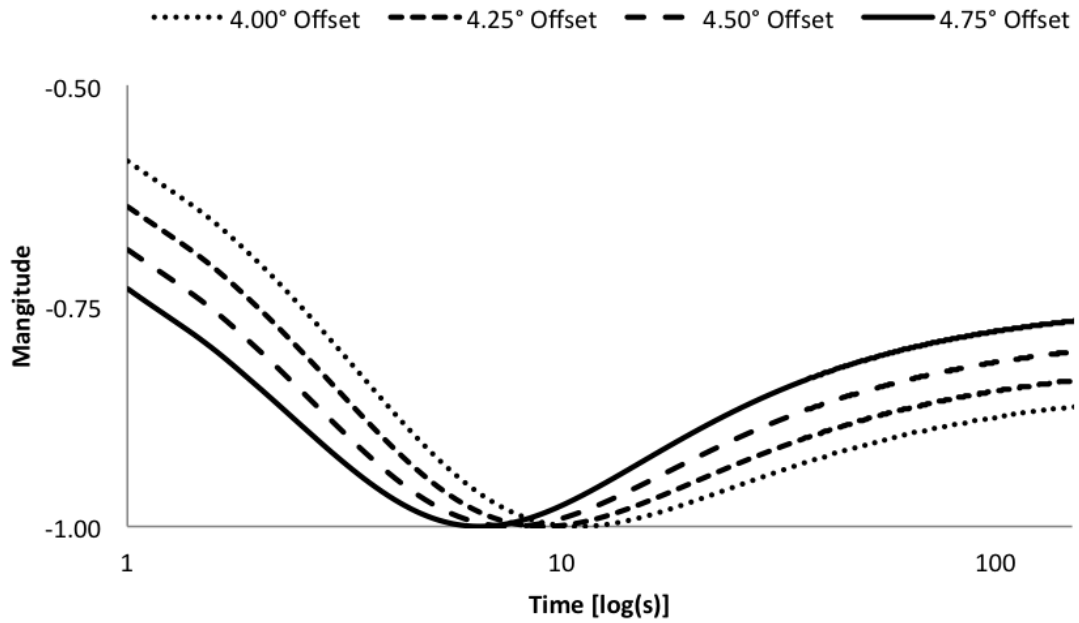


Figure B.1: Diverging Channel First Interface Orientation Factor for Streamline Angle $\theta = 4.00^\circ$, $\theta = 4.25^\circ$, $\theta = 4.50^\circ$, and $\theta = 4.75^\circ$

Observe as $\theta \rightarrow \alpha$, the equilibrium orientation value of the first interface orientation factor goes to a shear equilibrium value $O_p = 0.707$. Note that the axis have been modified from a typically diverging channel first interface orientation plot for presentation quality. First interface orientation factor values at $t = 10^4$ was $O_p = -0.840$, $O_p = -0.810$, $O_p = -0.777$, and $O_p = -0.743$ for $\theta = 4.00$, $\theta = 4.25$, $\theta = 4.50$, and $\theta = 4.75$.

B.2 Lid Driven Cavity Inner Streamline ($y = 0.23$)

B.2.1 Upward Flight

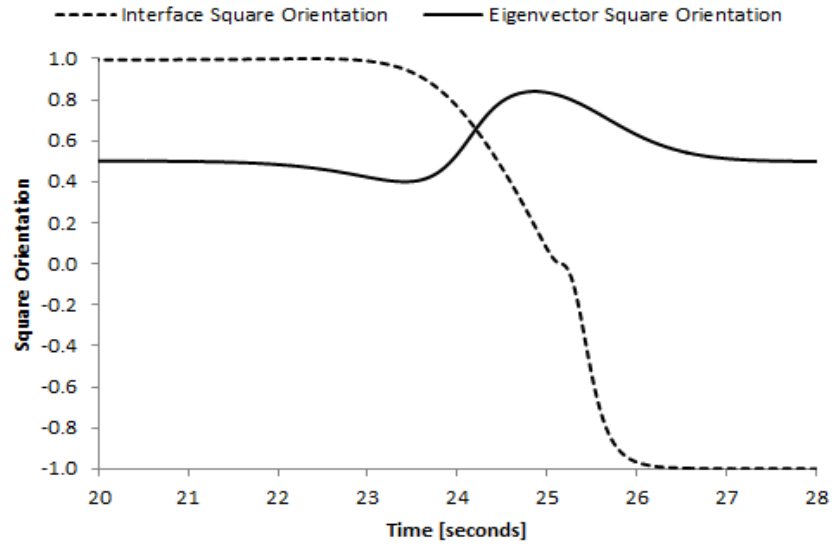


Figure B.2: Lid Driven Cavity Upward Flight Square Orientation Plot for \mathbf{p} and \mathbf{d}_1 for $y_0 = 0.45$

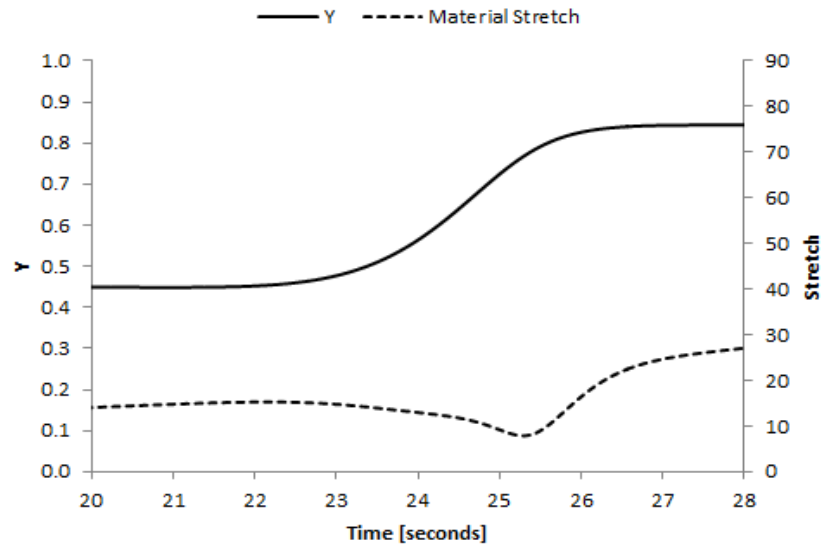


Figure B.3: Lid Driven Cavity Upward Flight Material Stretch for $y_0 = 0.45$

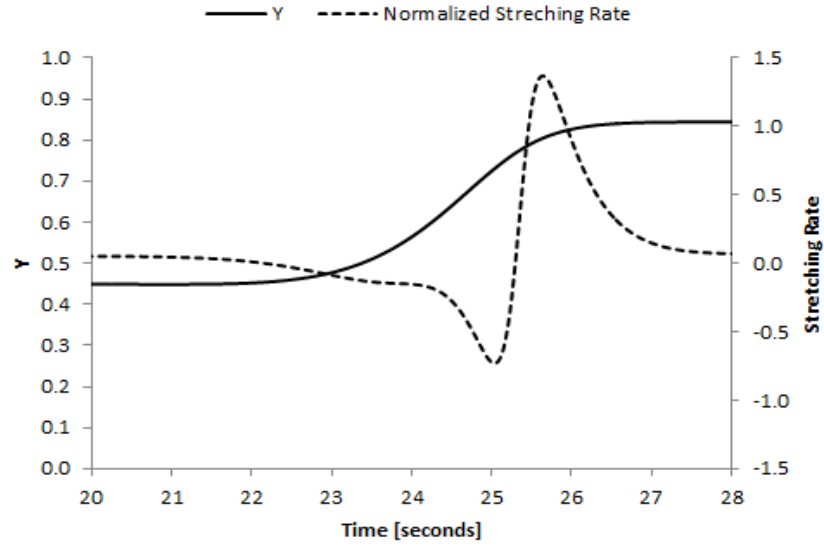


Figure B.4: Lid Driven Cavity Upward Flight Normalized Material Stretch Rate for $y_0 = 0.45$

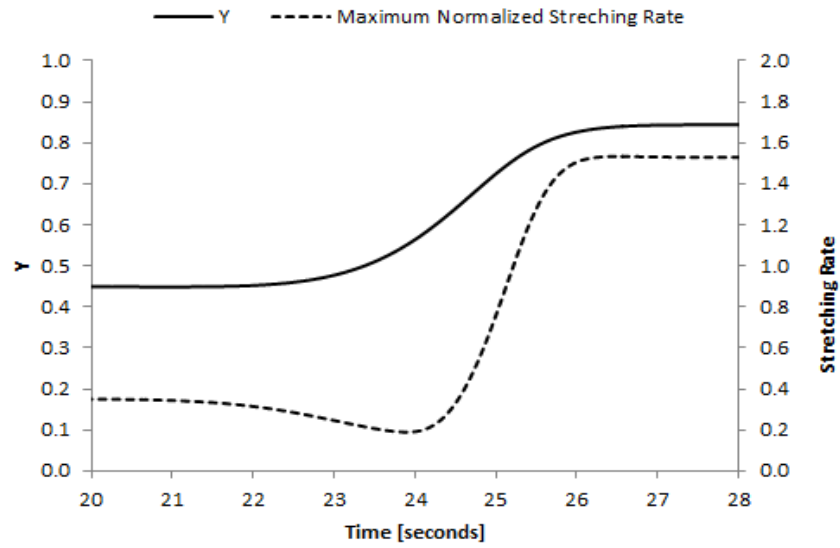


Figure B.5: Lid Driven Cavity Upward Flight Maximum Normalized Material Stretching Rate for $y_0 = 0.45$

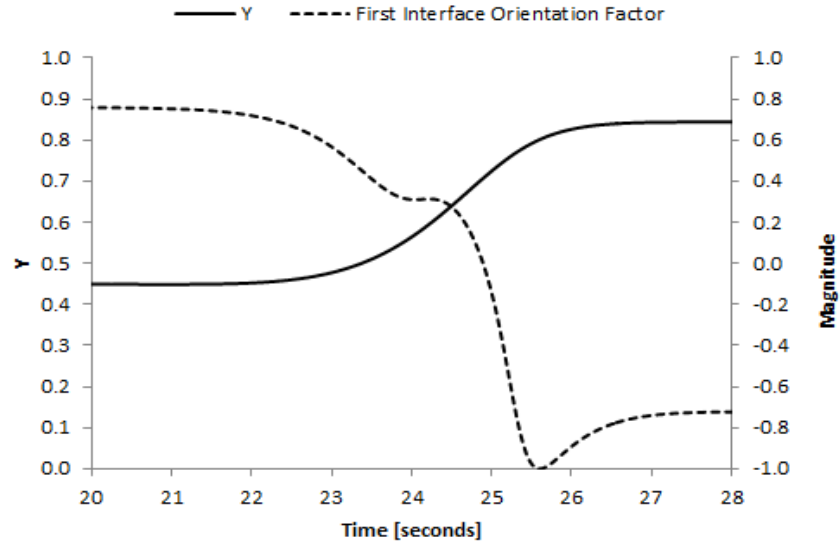


Figure B.6: Lid Driven Cavity Upward Flight First Interface Orientation Factor for $y_0 = 0.45$

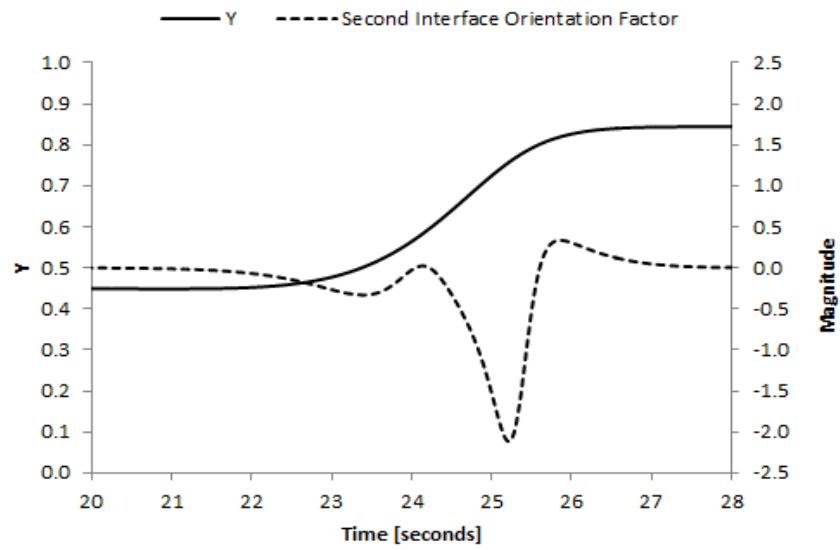


Figure B.7: Lid Driven Cavity Upward Flight Second Interface Orientation Factor for $y_0 = 0.45$

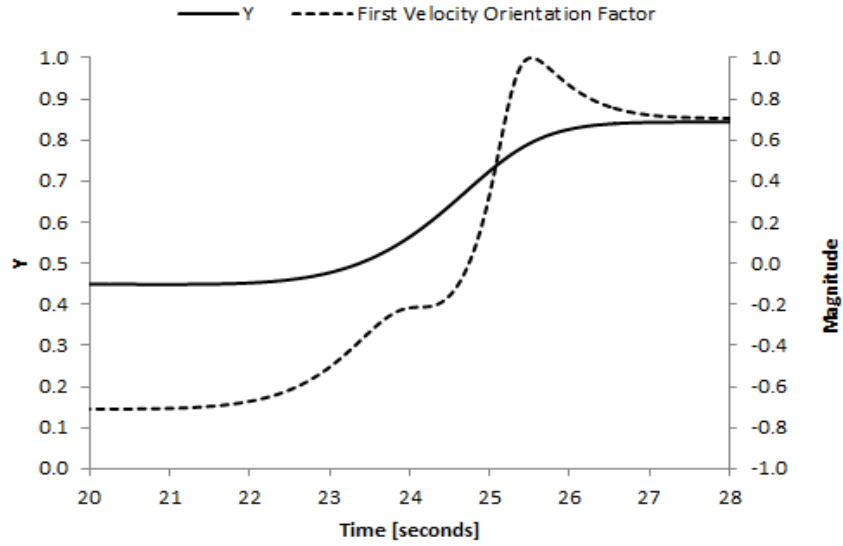


Figure B.8: Lid Driven Cavity Upward Flight First Velocity Orientation Factor for $y_0 = 0.45$

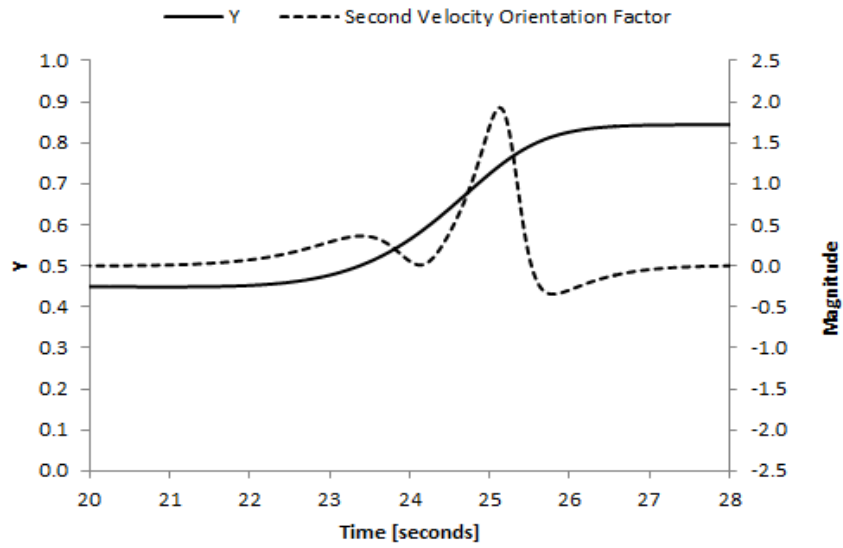


Figure B.9: Lid Driven Cavity Upward Flight Second Velocity Orientation Factor for $y_0 = 0.45$

B.2.2 Downward Flight

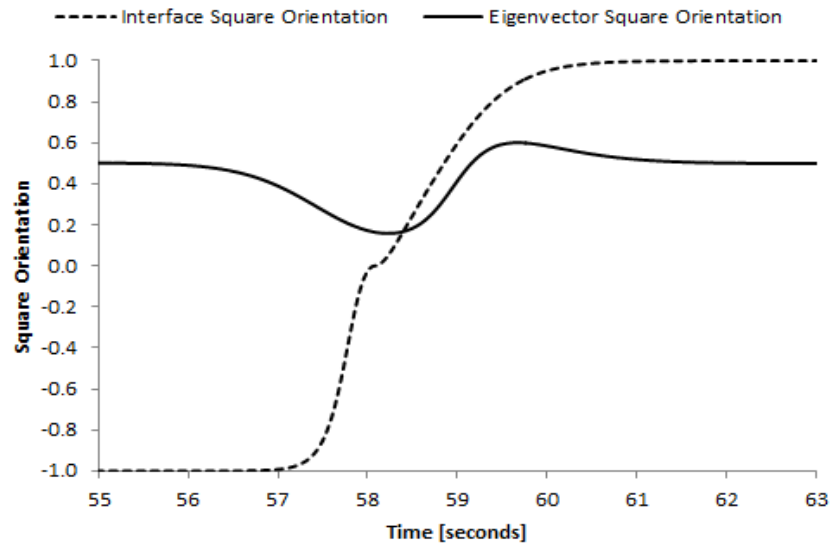


Figure B.10: Lid Driven Cavity Downward Flight Square Orientation Plot for p and d_1 for $y_0 = 0.45$

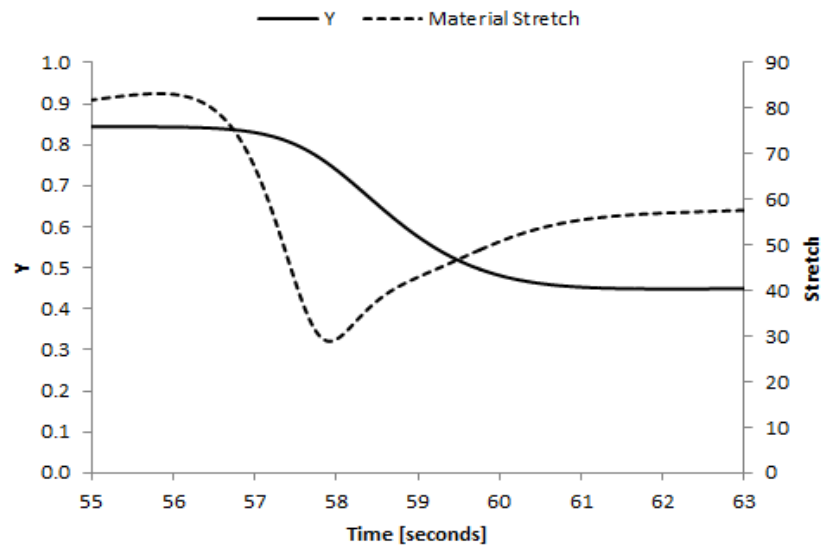


Figure B.11: Lid Driven Cavity Downward Flight Material Stretch for $y_0 = 0.45$

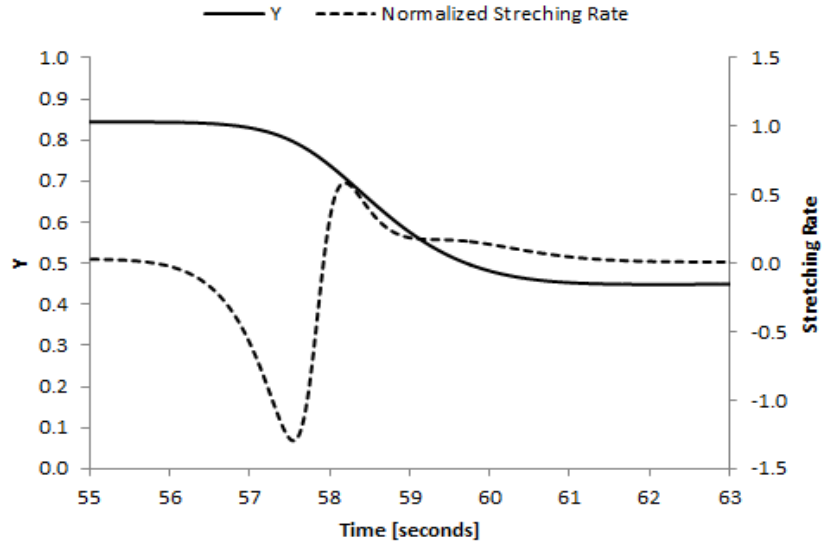


Figure B.12: Lid Driven Cavity Downward Flight Normalized Material Stretch Rate for $y_0 = 0.45$

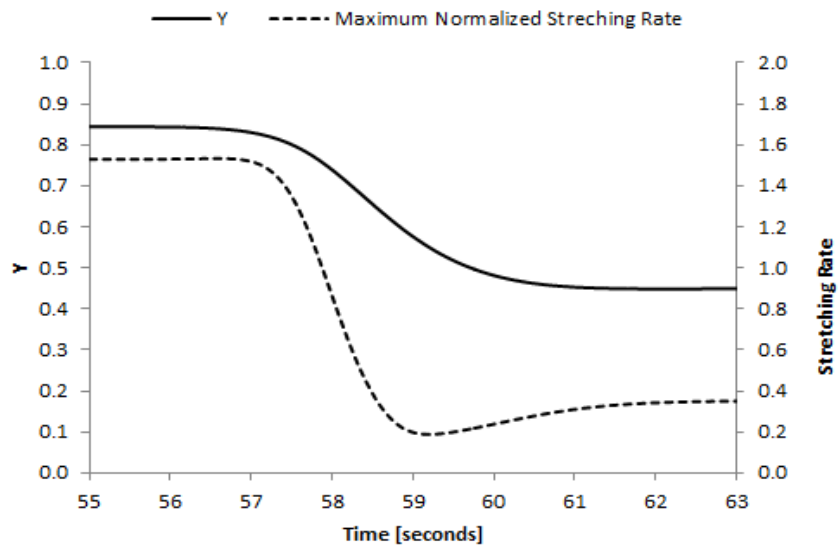


Figure B.13: Lid Driven Cavity Downward Flight Maximum Normalized Material Stretching Rate for $y_0 = 0.45$

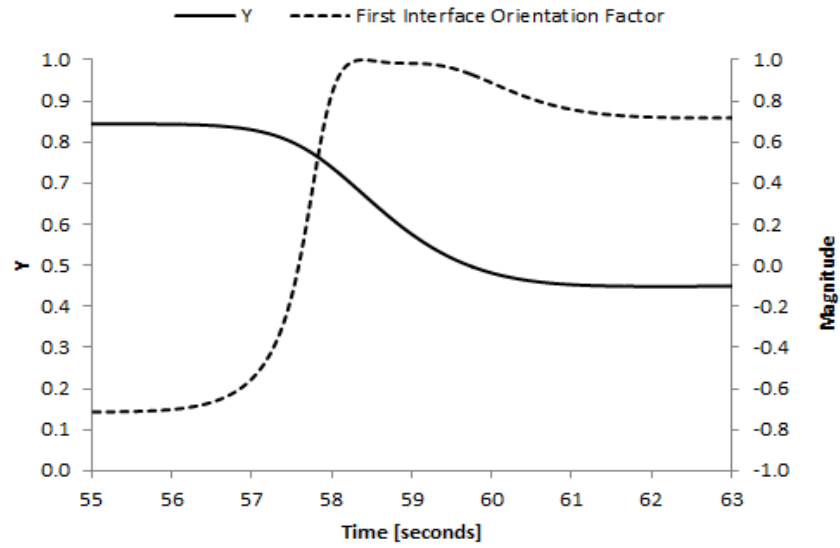


Figure B.14: Lid Driven Cavity Downward Flight First Interface Orientation Factor for $y_0 = 0.45$

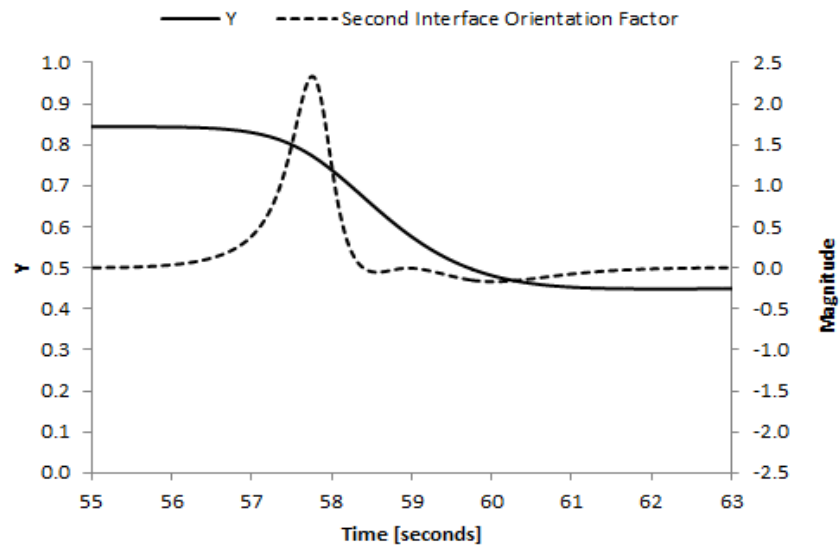


Figure B.15: Lid Driven Cavity Downward Flight Second Interface Orientation Factor for $y_0 = 0.45$

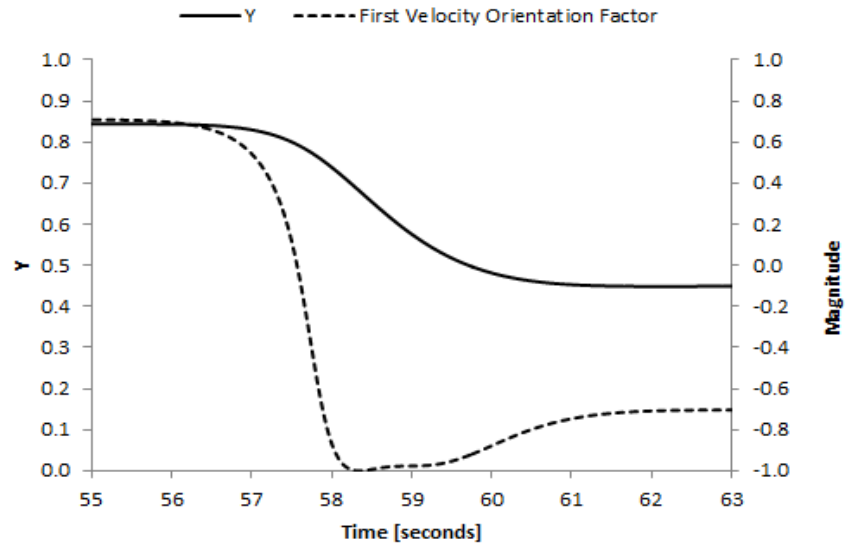


Figure B.16: Lid Driven Cavity Downward Flight First Velocity Orientation Factor for $y_0 = 0.45$

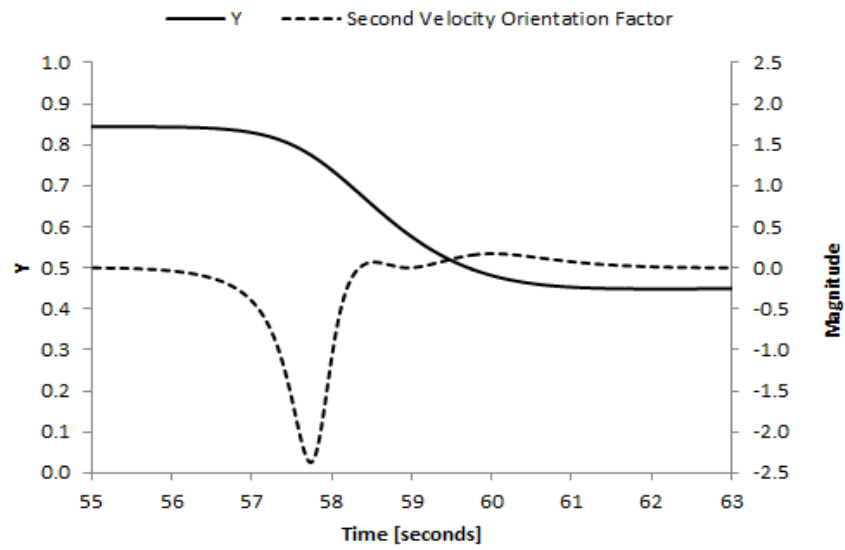


Figure B.17: Lid Driven Cavity Downward Flight Second Velocity Orientation Factor for $y_0 = 0.45$

B.3 Lid Driven Cavity Outer Streamline ($y = 0.23$)

B.3.1 Upward Flight

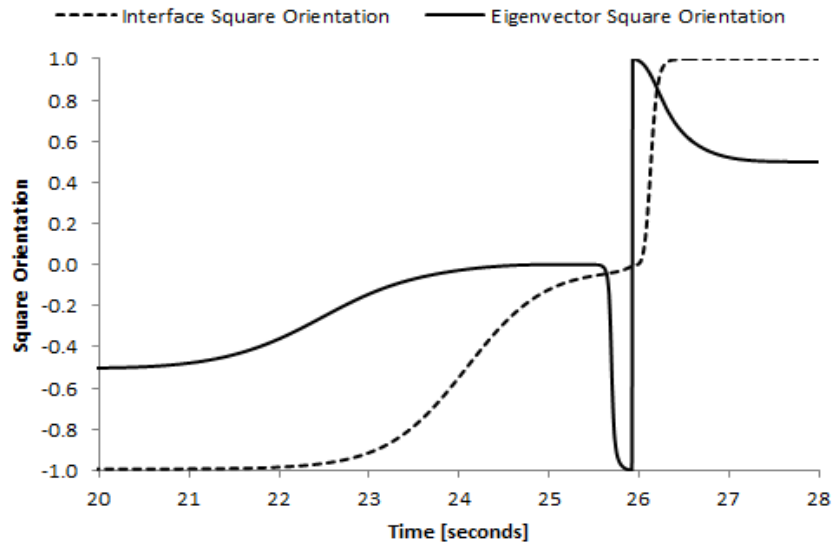


Figure B.18: Lid Driven Cavity Upward Flight Square Orientation Plot for \mathbf{p} and \mathbf{d}_1 for $y_0 = 0.23$

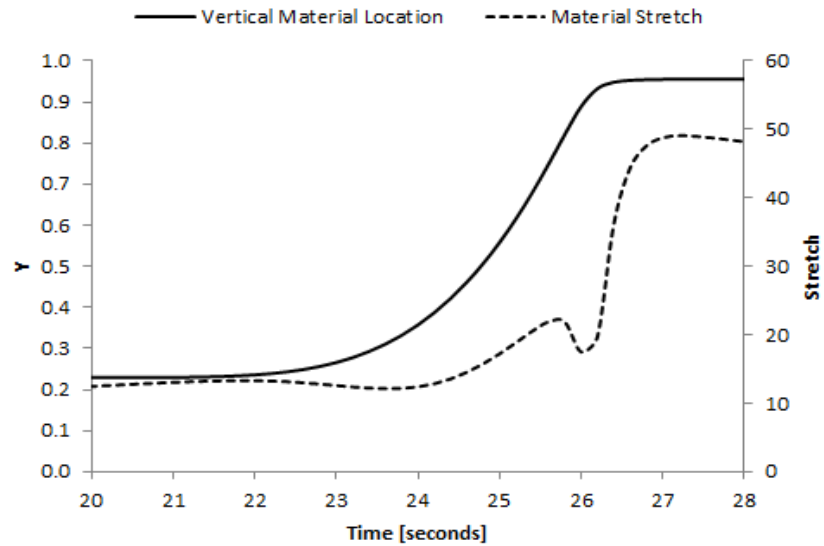


Figure B.19: Lid Driven Cavity Upward Flight Material Stretch for $y_0 = 0.23$

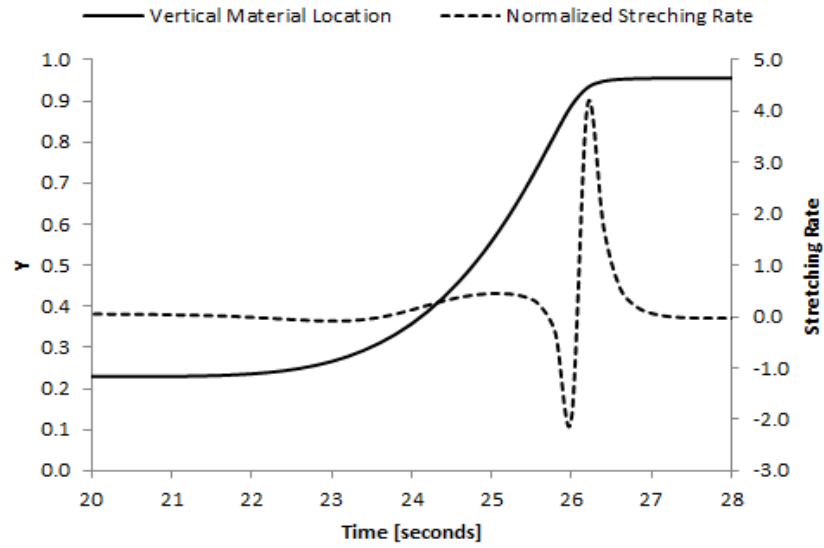


Figure B.20: Lid Driven Cavity Upward Flight Normalized Material Stretch Rate for $y_0 = 0.23$

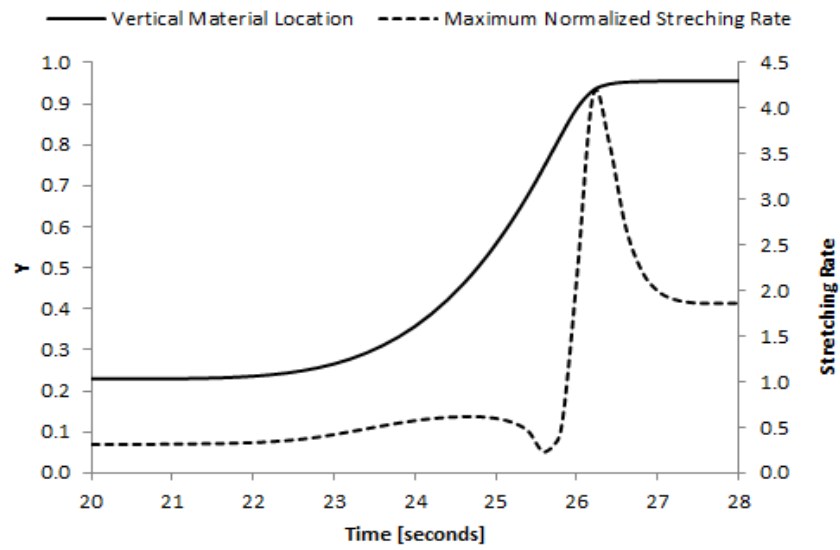


Figure B.21: Lid Driven Cavity Upward Flight Maximum Normalized Material Stretching Rate for $y_0 = 0.23$

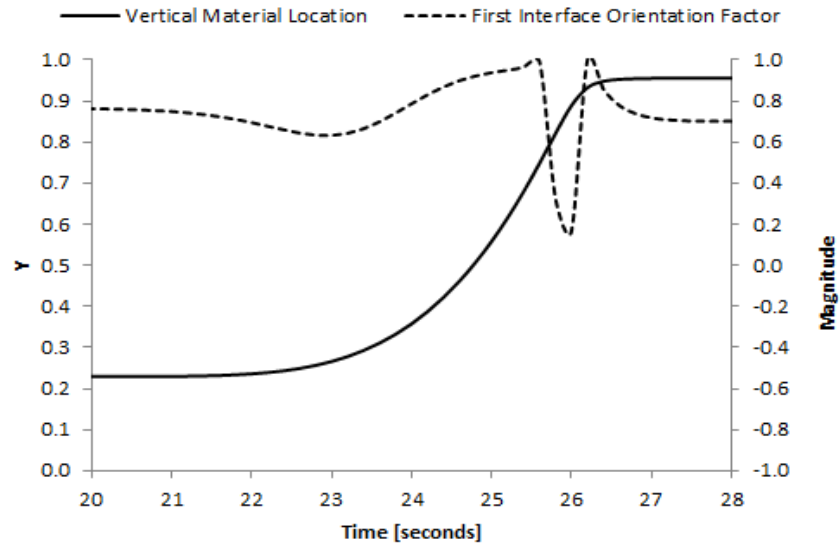


Figure B.22: Lid Driven Cavity Upward Flight First Interface Orientation Factor for $y_0 = 0.23$

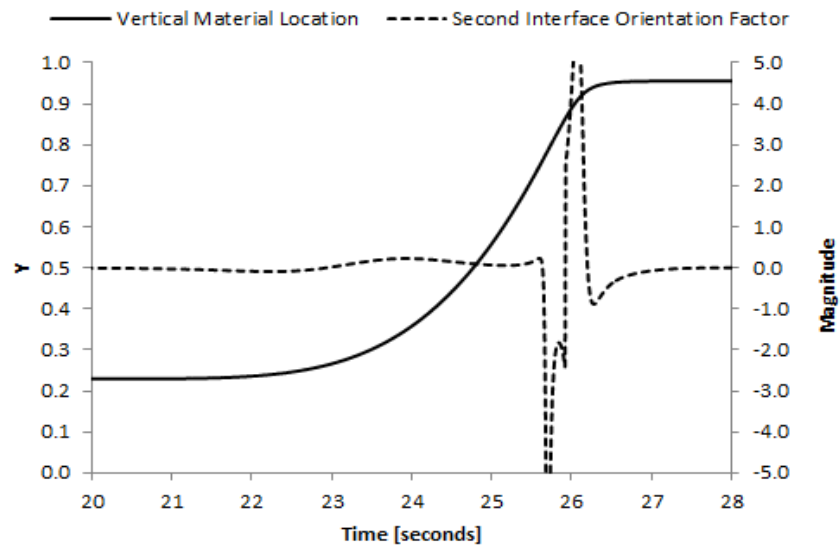


Figure B.23: Lid Driven Cavity Upward Flight Second Interface Orientation Factor for $y_0 = 0.23$

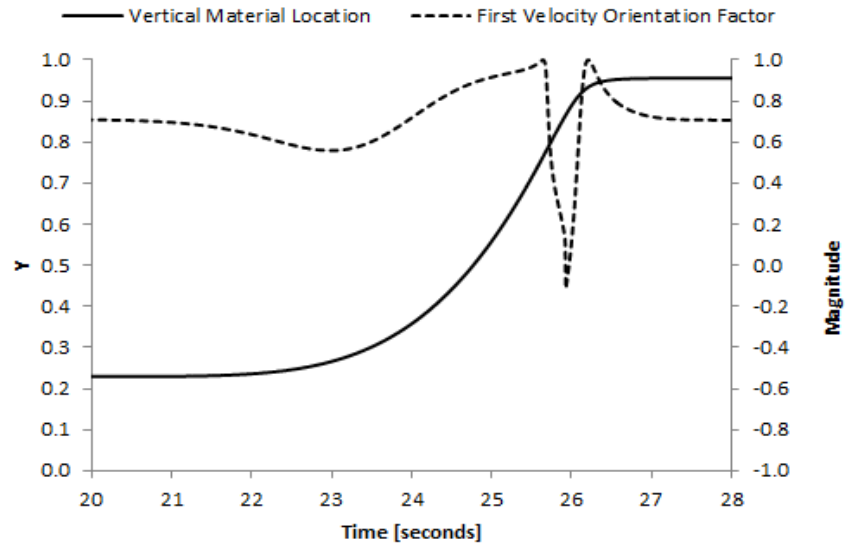


Figure B.24: Lid Driven Cavity Upward Flight First Velocity Orientation Factor for $y_0 = 0.23$

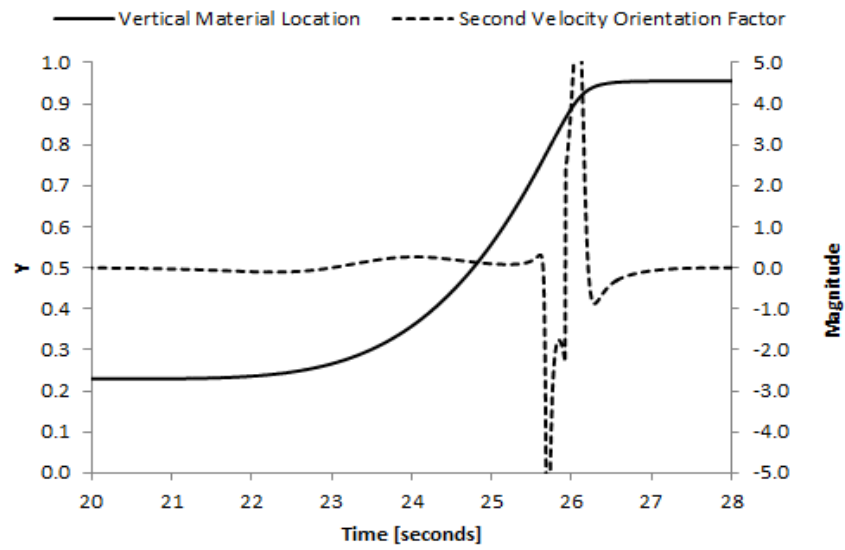


Figure B.25: Lid Driven Cavity Upward Flight Second Velocity Orientation Factor for $y_0 = 0.23$

B.3.2 Downward Flight

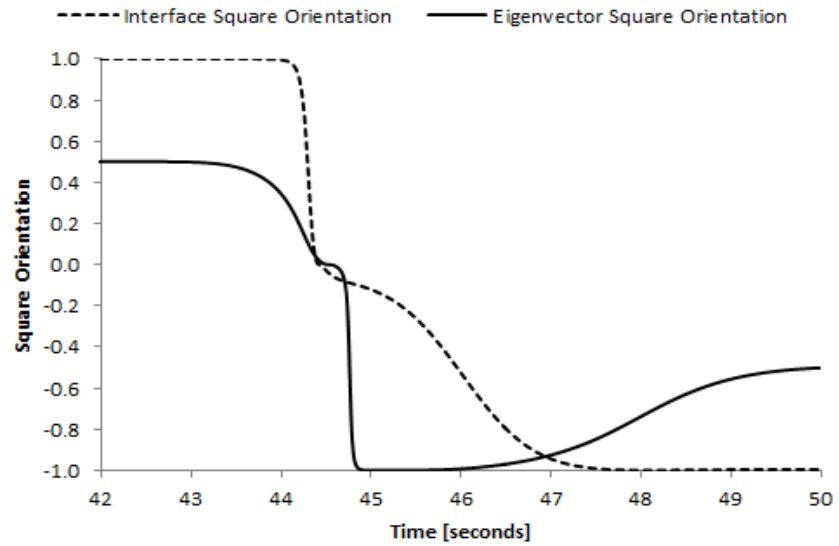


Figure B.26: Lid Driven Cavity Downward Flight Square Orientation Plot for p and d_1 for $y_0 = 0.23$

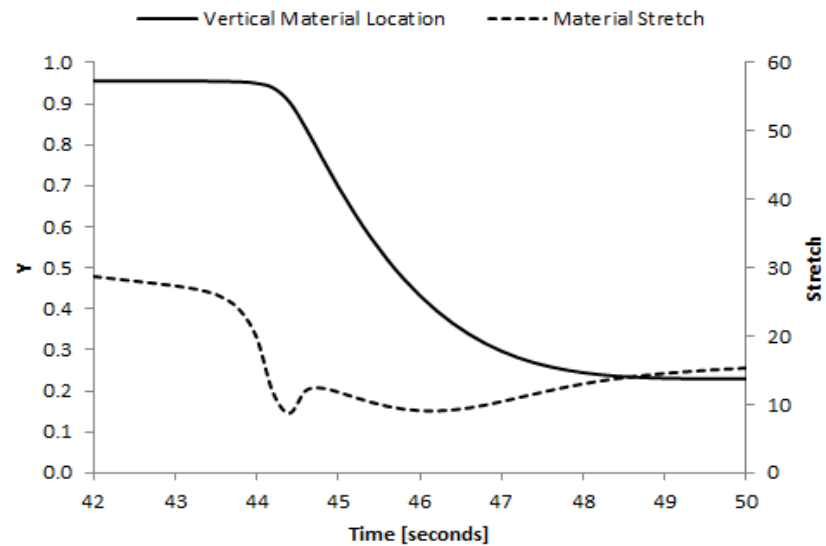


Figure B.27: Lid Driven Cavity Downward Flight Material Stretch for $y_0 = 0.23$

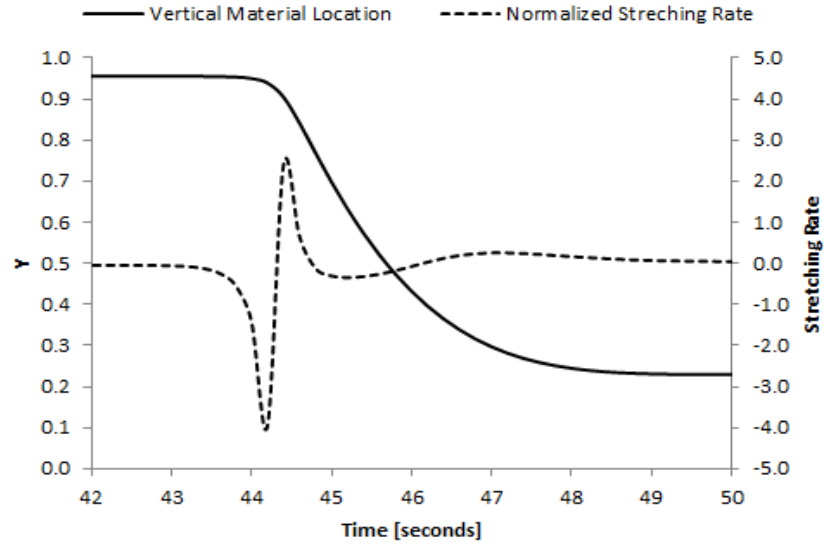


Figure B.28: Lid Driven Cavity Downward Flight Normalized Material Stretch Rate for $y_0 = 0.23$

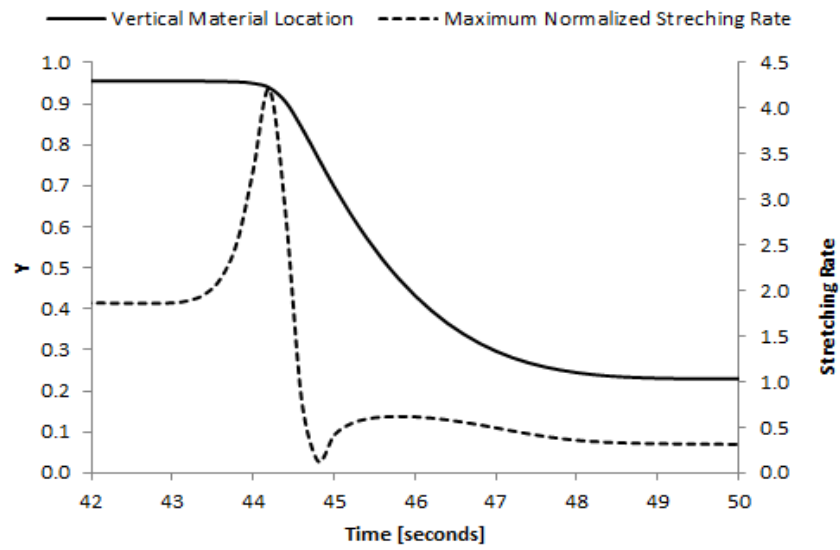


Figure B.29: Lid Driven Cavity Downward Flight Maximum Normalized Material Stretching Rate for $y_0 = 0.23$

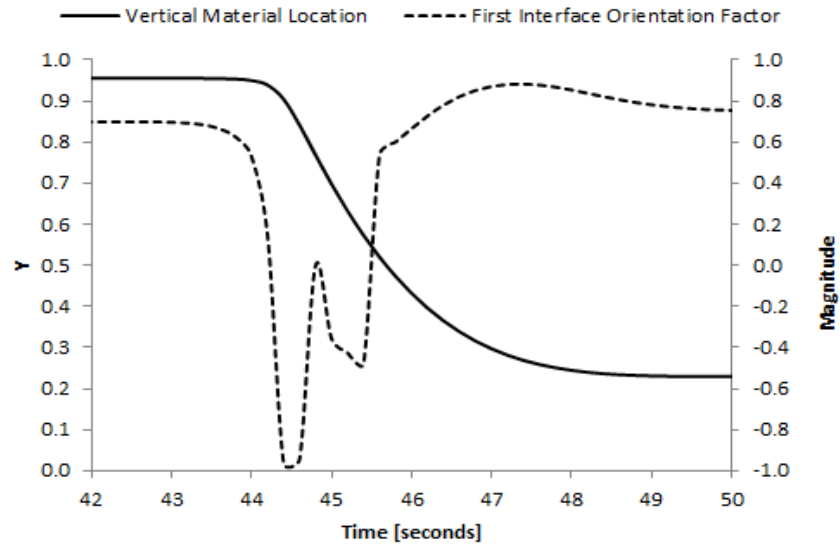


Figure B.30: Lid Driven Cavity Downward Flight First Interface Orientation Factor for $y_0 = 0.23$

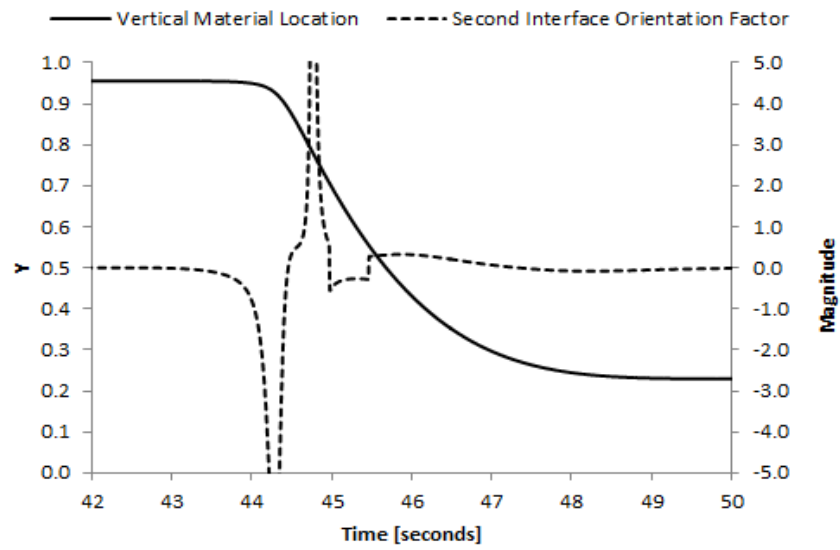


Figure B.31: Lid Driven Cavity Downward Flight Second Interface Orientation Factor for $y_0 = 0.23$

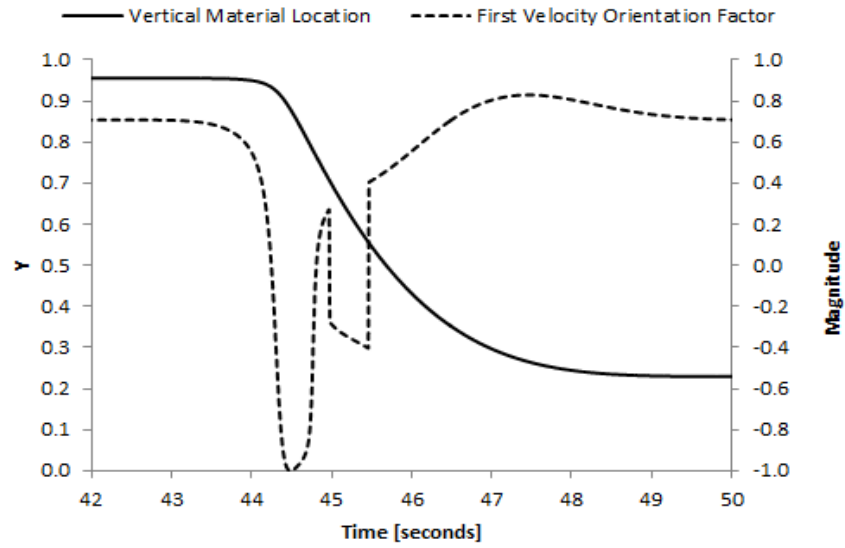


Figure B.32: Lid Driven Cavity Downward Flight First Velocity Orientation Factor for $y_0 = 0.23$

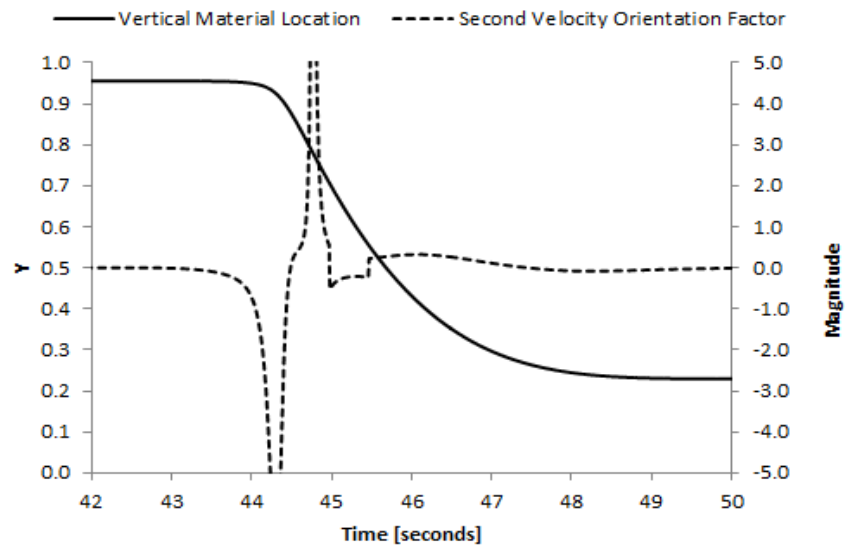


Figure B.33: Lid Driven Cavity Downward Flight Second Velocity Orientation Factor for $y_0 = 0.23$

Appendix C: Code

C.1 Couette Channel

C.1.1 Master Code

```
1 %
2 %   Title:       New Measures for the Study of Distributive Mixing
3 %               in Continuous Creeping Flows
4 %
5 %   Author:     Jason Nixon
6 %
7 %   Code:       2D Steady State Couette Channel Master Code
8 %
9
10 clc; clear; close all
11
12 global U h dt tmax
13
14 U=0.5;         % Top wall velocity
15
16 h=1;          % Channel heigh
17
18 dt=0.1;       % Time step
19
20 tmax=15;      % Run time
21
22 theta = [ 0 45 90 135 ]*pi/180;    % Interface angles
23
24 Time=zeros (tmax/dt+1,numel(theta));
25 SquareOrientationInterface=zeros (tmax/dt+1,numel(theta));
26 MaterialStretch=zeros (tmax/dt+1,numel(theta));
27 FirstInterfaceOrientationFactor=zeros (tmax/dt+1,numel(theta));
28 FirstVelocityOrientationFactor=zeros (tmax/dt+1,numel(theta));
29 SecondInterfaceOrientationFactor=zeros (tmax/dt+1,numel(theta));
30 SecondVelocityOrientationFactor=zeros (tmax/dt+1,numel(theta));
31 MaximumNormalizedStretchingRate=zeros (tmax/dt+1,numel(theta));
32 NormalizedStretchingRate=zeros (tmax/dt+1,numel(theta));
33
34 for n=1:numel(theta)
35
36     [   Time(:,n),...
37         SquareOrientationInterface(:,n), ...
38         MaterialStretch(:,n), ...
39         FirstInterfaceOrientationFactor(:,n), ...
40         FirstVelocityOrientationFactor(:,n), ...
41         SecondInterfaceOrientationFactor(:,n), ...
42         SecondVelocityOrientationFactor(:,n), ...
43         MaximumNormalizedStretchingRate(:,n), ...
44         NormalizedStretchingRate(:,n)   ] = ...
45     Flow1_CODE_Routine_1(theta(n));
46
```

```

47 end
48
49 dlmwrite('Flow1_DATA_time', ...
50         Time, 'precision', '%15.13f')
51 dlmwrite('Flow1_DATA_SquareOrientationInterface', ...
52         SquareOrientationInterface, 'precision', '%15.13f')
53 dlmwrite('Flow1_DATA_MaterialStretch', ...
54         MaterialStretch, 'precision', '%15.13f')
55 dlmwrite('Flow1_DATA_FirstInterfaceOrientationFactor', ...
56         FirstInterfaceOrientationFactor, 'precision', '%15.13f')
57 dlmwrite('Flow1_DATA_SecondInterfaceOrientationFactor', ...
58         SecondInterfaceOrientationFactor, 'precision', '%15.13f')
59 dlmwrite('Flow1_DATA_FirstVelocityOrientationFactor', ...
60         FirstVelocityOrientationFactor, 'precision', '%15.13f')
61 dlmwrite('Flow1_DATA_SecondVelocityOrientationFactor', ...
62         SecondVelocityOrientationFactor, 'precision', '%15.13f')
63 dlmwrite('Flow1_DATA_MaximumNormalizedStretchingRate', ...
64         MaximumNormalizedStretchingRate, 'precision', '%15.13f')
65 dlmwrite('Flow1_DATA_NormalizedStretchingRate', ...
66         NormalizedStretchingRate, 'precision', '%15.13f')

```

C.1.2 Material Tracking Module

```

1 function [t, SOI, ds, IOF1, UOF1, IOF2, UOF2, MNSR, NSR] = ...
2     Flow1_CODE_Routine_1(theta)
3
4     global U h dt tmax
5
6     ds(1)=1;
7
8     u=[1 ; 0];
9
10    G=U/h;
11
12    L=[0 G ; 0 0];
13
14    D=0.5*(L+L');
15
16    W=0.5*(L-L');
17
18    T=[0 0 ; 0 0];
19
20    [n, n, d1]=PD2v2(D);
21
22    MNSR(1)=sqrt(sum(sum(D.*D))/2);
23
24    dx(:,1)=[cos(theta) sin(theta)];
25
26    [ds(1), p, n, SOI(1)]=vec_prop(dx(:,1), [1 0]');
27
28    IOF1(1)=dot(p, d1);

```



```

29
30     UOF1(1)=dot(u,d1);
31
32     IOF2(1)=d1'*(D+W-eye(2)*(p'*D*p)-T)*p;
33
34     UOF2(1)=d1'*(D+W-eye(2)*(u'*D*u)-T)*u;
35
36     NSR(1)=p'*D*p;
37
38     for n=2:tmax/dt+1
39
40         dx(:,n)=dt*L*dx(:,n-1)+dx(:,n-1);
41
42         [ds(n),p,tau,SOI(n)]=vec_prop(dx(:,n),[1 0]');
43
44         IOF1(n)=dot(p,d1);
45
46         UOF1(n)=dot(u,d1);
47
48         IOF2(n)=d1'*(D+W-eye(2)*(p'*D*p)-T)*p;
49
50         UOF2(n)=d1'*(D+W-eye(2)*(u'*D*u)-T)*u;
51
52         MNSR(n)=sqrt(DDP(D,D)/2);
53
54         NSR(n)=MNSR(n)*(2*IOF1(n)^2-1);
55
56     end
57
58     t=linspace(0,tmax,tmax/dt+1);
59
60 end

```

C.2 Diverging Channel

C.2.1 Master Code

```

1 %
2 %   Title:      New Measures for the Study of Distributive Mixing
3 %              in Continuous Creeping Flows
4 %
5 %   Author:    Jason Nixon
6 %
7 %   Code:      2D Steady State Diverging Channel Master Code
8 %
9
10 clc; clear; close all; format long
11
12 global N alpha F0 tmax dt init_orient R0 ds0 Re
13
14 %Material Properties

```

```

15 rho=1000; % Density
16
17 mu=10; % Kinematic viscosity
18
19 nu=mu/rho; % Dynamic viscosity
20
21 N=1001; % Number of divisions in time for solver
22
23 alpha=5*pi/180; % Channel divergence angle
24
25 F0=0.1; % Centerline F value
26
27 tmax=10000; % Runtime
28
29 dt=2; % Time step
30
31 ds0=1; % Initial interface magnitude
32
33 init_orient=[10;1]; % Initial orientation
34
35 Re=F0*alpha/nu; % Reynolds number
36
37 R0=1; % Initial radial location
38
39 theta=[4.00 4.25 4.50 4.75]*pi/180; % Test angles
40
41 UOF1Profile=zeros(N,numel(theta));
42 FProfile=zeros(N,numel(theta));
43 MNSRProfile=zeros(N,numel(theta));
44 VorticityProfile=zeros(N,numel(theta));
45 TwirlProfile=zeros(N,numel(theta));
46 Time=zeros(tmax/dt+1,numel(theta));
47 SquareOrientationInterface=zeros(tmax/dt+1,numel(theta));
48 MaterialStretch=zeros(tmax/dt+1,numel(theta));
49 MaximumNormalizedStretchingRate=zeros(tmax/dt+1,numel(theta));
50 NormalizedStretchingRate=zeros(tmax/dt+1,numel(theta));
51 VorticityHistory=zeros(tmax/dt+1,numel(theta));
52 TwirlHistory=zeros(tmax/dt+1,numel(theta));
53 FirstInterfaceOrientationFactor=zeros(tmax/dt+1,numel(theta));
54 SecondInterfaceOrientationFactor=zeros(tmax/dt+1,numel(theta));
55 FirstVelocityOrientationFactor=zeros(tmax/dt+1,numel(theta));
56 SecondVelocityOrientationFactor=zeros(tmax/dt+1,numel(theta));
57 RadialDisplacement=zeros(tmax/dt+1,numel(theta));
58
59 for n=1:numel(theta)
60
61 [ Time(:,n), ...
62 UOF1Profile(:,n), ...
63 FProfile(:,n) , ...
64 MNSRProfile(:,n), ...
65 VorticityProfile(:,n), ...
66 TwirlProfile(:,n), ...
67 SquareOrientationInterface(:,n), ...
68 MaterialStretch(:,n), ...

```

```

69     MaximumNormalizedStretchingRate(:,n), ...
70     NormalizedStretchingRate(:,n), ...
71     VorticityHistory(:,n), ...
72     TwirlHistory(:,n), ...
73     FirstInterfaceOrientationFactor(:,n), ...
74     SecondInterfaceOrientationFactor(:,n), ...
75     FirstVelocityOrientationFactor(:,n), ...
76     SecondVelocityOrientationFactor(:,n), ...
77     RadialDisplacement(:,n)] ...
78     =Flow2_CODE_Routine_1(theta(n));
79
80 end
81
82 dlmwrite('Flow2_DATA.UOF1Profile', ...
83         UOF1Profile, 'precision', '%15.13f')
84 dlmwrite('Flow2_DATA.FProfile', ...
85         FProfile, 'precision', '%15.13f')
86 dlmwrite('Flow2_DATA.MNSRProfile', ...
87         MNSRProfile, 'precision', '%15.13f')
88 dlmwrite('Flow2_DATA.VorticityProfile', ...
89         VorticityProfile, 'precision', '%15.13f')
90 dlmwrite('Flow2_DATA.TwirlProfile', ...
91         TwirlProfile, 'precision', '%15.13f')
92 dlmwrite('Flow2_DATA.Time', ...
93         Time, 'precision', '%15.13f')
94 dlmwrite('Flow2_DATA.SquareOrientationInterface', ...
95         SquareOrientationInterface, 'precision', '%15.13f')
96 dlmwrite('Flow2_DATA.MaterialStretch', ...
97         MaterialStretch, 'precision', '%15.13f')
98 dlmwrite('Flow2_DATA.FirstInterfaceOrientationFactor', ...
99         FirstInterfaceOrientationFactor, 'precision', '%15.13f')
100 dlmwrite('Flow2_DATA.SecondInterfaceOrientationFactor', ...
101         SecondInterfaceOrientationFactor, 'precision', '%15.13f')
102 dlmwrite('Flow2_DATA.FirstVelocityOrientationFactor', ...
103         FirstVelocityOrientationFactor, 'precision', '%15.13f')
104 dlmwrite('Flow2_DATA.SecondVelocityOrientationFactor', ...
105         SecondVelocityOrientationFactor, 'precision', '%15.13f')
106 dlmwrite('Flow2_DATA.MaximumNormalizedStretchingRate', ...
107         MaximumNormalizedStretchingRate, 'precision', '%15.13f')
108 dlmwrite('Flow2_DATA.NormalizedStretchingRate', ...
109         NormalizedStretchingRate, 'precision', '%15.13f')
110 dlmwrite('Flow2_DATA.VorticityHistory', ...
111         VorticityHistory, 'precision', '%15.13f')
112 dlmwrite('Flow2_DATA.TwirlHistory', ...
113         TwirlHistory, 'precision', '%15.13f')
114 dlmwrite('Flow2_DATA.RadialDisplacement', ...
115         RadialDisplacement, 'precision', '%15.13f')

```

C.2.2 Material Tracking Module

```

1 function [ Time,UOF1Profile,FProfile,MNSRProfile,VorticityProfile,...

```

```

2 TwirlProfile, SOI, ds, MNSR, NSR, w, tw, IOF1, IOF2, UOF1, UOF2, R] ...
3 = Flow2_CODE_Routine_1(theta )
4
5 global N alpha F0 tmax dt init_orient R0 ds0 Re
6
7 ds(1)=ds0;
8
9 R(1)=R0;
10
11 u=[1;0];
12
13 dx(:,1)=ds0*init_orient/sqrt(dot(init_orient,init_orient));
14
15 aR=[0 ;
16     50;
17     100;
18     188;
19     300;
20     500;
21     800;
22     1400];
23
24 k=[-2.00508465;
25     -3.5394176;
26     -5.8691811;
27     -6.8802251;
28     -18.9682230;
29     -32.4654512;
30     -52.3003336;
31     -85.0484725];
32
33 K=interp1(aR,k,alpha*Re);
34
35 [tau,G]=ode45(@Flow2_CODE_Routine_2,linspace(0,1,N),[1 0 K]);
36
37 Kc(1)=sign(K)*(abs(K)-mod(abs(K),1));
38
39 conv_iter=10;
40
41 for n=1:conv_iter
42     for j=1:11
43         off=((j-1)/5-1)/(10^n);
44         [tau,G]=ode45(@Flow2_CODE_Routine_2,linspace(0,1,N),...
45             [1 0 Kc(n)+off]);
46         G_range(j)=G(1001,1);
47         eta_range(j)=Kc(n)+off;
48     end
49
50     Kc(n+1)=interp1(G_range,eta_range,min(0));
51
52 end
53
54 [tau,G]=ode45(@Flow2_CODE_Routine_2,linspace(0,1,N),...
55     [1 0 Kc(conv_iter+1)]);

```

```

56
57     Kc(conv_iter+1);
58
59     F=G*F0;
60
61     for n=1:N
62
63         f=F(n,1);
64
65         fp=F(n,2);
66
67         L=[-f 0 ; fp f];
68
69         D=0.5*(L+L');
70
71         W=0.5*(L-L');
72
73         DD=[2*f^2 -f*fp ; -f*fp -2*f^2];
74
75         [r, r, e1]=PD2v2(D);
76
77         T=(1/(4*(sum(sum(D.*D))/2)^2))* (DD*D-D*DD);
78
79         MNSRProfile(n)=sqrt(sum(sum(D.*D))/2);
80
81         VorticityProfile(n)=DDP([0 -1 ; 1 0],W)/2;
82
83         TwirlProfile(n)=DDP([0 -1 ; 1 0],T)/2;
84
85         UOF1Profile(n)=dot(e1,u);
86
87     end
88
89     f=interp1(linspace(0,alpha,N),F(:,1),theta);
90
91     fp=interp1(linspace(0,alpha,N),F(:,2),theta);
92
93     fpp=interp1(linspace(0,alpha,N),F(:,3),theta);
94
95     for j=1:1000
96         valU(j)=f/j;
97     end
98
99     L=(1/R(1)^2)*[-f 0 ; fp f];
100
101     D=0.5*(L+L');
102
103     W=0.5*(L-L');
104
105     DD=(1/R(1)^4)*[2*f^2 -f*fp ; -f*fp -2*f^2];
106
107     T=(DD*D-D*DD)/(2*sum(sum(D.*D)));
108
109     MNSR(1)=sqrt(sum(sum(D.*D))/2);

```

```

110     w(1)=sum(sum([0 -0.5 ; 0.5 0].*W));
111
112     tw(1)=sum(sum([0 -0.5 ; 0.5 0].*T));
113
114     [ds(1),p,ϕ,SOI(1)]=vec_prop(dx(:,1),[1 0]);
115
116     [ϕ,ϕ,e1]=PD2v2(D);
117
118     u=[1 ; 0];
119
120     NSR(1)=p'*D*p;
121
122     IOF1(1)=dot(e1,p);
123
124     IOF2(1)=e1'*(D+W-eye(2)*(p'*D*p)-T)*p;
125
126     UOF1(1)=dot(e1,u);
127
128     UOF2(1)=e1'*(D+W-eye(2)*(u'*D*u)-T)*u;
129
130     for n=2:tmax/dt+1
131
132         Lp=L;
133
134         RK1=interp1(valU,R(n-1));
135
136         RK2=interp1(valU,R(n-1)+0.5*RK1);
137
138         RK3=interp1(valU,R(n-1)+0.5*RK2);
139
140         RK4=interp1(valU,R(n-1)+0.5*RK3);
141
142         R(n)=R(n-1)+dt*(RK1+2*RK2+2*RK3+RK4)/6;
143
144         L=(1/R(n)^2)*[-f 0 ; fp f];
145
146         D=0.5*(L+L');
147
148         W=0.5*(L-L');
149
150         DD=(1/R(n)^4)*[2*f^2 -f*fp ; -f*fp -2*f^2];
151
152         T=(DD*D-D*DD)/(2*sum(sum(D.*D)));
153
154         MNSR(n)=sqrt(sum(sum(D.*D))/2);
155
156         w(n)=sum(sum([0 -0.5 ; 0.5 0].*W));
157
158         tw(n)=sum(sum([0 -0.5 ; 0.5 0].*T));
159
160         NSR(n)=p'*D*p;
161
162         [ϕ,ϕ,e1]=PD2v2(D);
163

```

```

164         [r,r,r,SOP(n)]=vec_prop(e1,[1 0]);
165
166         dx(:,n)=(dt*(L+Lp)/2)*dx(:,n-1)+dx(:,n-1);
167
168         [ds(n),p,r,SOI(n)]=vec_prop(dx(:,n),[1 0]);
169
170
171         u=[1 ; 0];
172
173         IOF1(n)=dot(e1,p);
174
175         IOF2(n)=e1'*(D+W-T-eye(2)*(p'*D*p))*p;
176
177         UOF1(n)=dot(e1,u);
178
179         UOF2(n)=e1'*(D+W-T-eye(2)*(u'*D*u))*u;
180
181     end
182
183     FProfile=F(:,1);
184
185     Time=linspace(0,tmax,tmax/dt+1);
186
187 end

```

C.2.3 ODE45 Equation Module

```

1 function [dy] = Flow2_CODE.Routine_2(t,y)
2
3     global Re alpha
4
5     dy=zeros(3,1);
6
7     dy(1)=y(2);
8
9     dy(2)=y(3);
10
11     dy(3)=-4*alpha^2*y(2)-2*alpha*Re*y(1)*y(2);
12
13 end

```

C.3 Lid Driven Cavity

C.3.1 Master Code

```

1 %
2 %   Title:      New Measures for the Study of Distributive Mixing
3 %              in Continuous Creeping Flows

```

```

4  %
5  %   Author:      Jason Nixon
6  %
7  %   Code:       Lid Driven Cavity Material Tracking Module
8  %
9
10 clc; clear; close all; format long;
11
12 global FDPParam PSI Ux Uy x0 tmax dt orient0
13
14 y0=[0.23 0.45];
15
16 x0=7.5;
17
18 tmax=80;
19
20 dt=0.05;
21
22 orient0=[ 0 ; 1 ];
23
24 FDPParam=dlmread('Flow3_DATA.FlowfieldParameters');
25
26 PSI=dlmread('Flow3_DATA.StreamFunction');
27
28 Ux=dlmread('Flow3_DATA.VelocityX');
29
30 Uy=dlmread('Flow3_DATA.VelocityY');
31
32 Nt=tmax/dt+1;
33
34 Nr=numel(y0);
35
36 RunParameters=zeros(Nt,Nr);
37 StreamFunctionPercentError=zeros(Nt,Nr);
38 Time=zeros(Nt,Nr);
39 CoordinateX=zeros(Nt,Nr);
40 CoordinateY=zeros(Nt,Nr);
41 MagnitudeVelocity=zeros(Nt,Nr);
42 MagnitudeTwirl=zeros(Nt,Nr);
43 MaterialStretch=zeros(Nt,Nr);
44 SquareOrientationVelocity=zeros(Nt,Nr);
45 SquareOrientationInteface=zeros(Nt,Nr);
46 SquareOrientationEigenvector=zeros(Nt,Nr);
47 NormalizedStretchingRate=zeros(Nt,Nr);
48 MaximumNormalizedStretchingRate=zeros(Nt,Nr);
49 MaximumNormalizedStretchingRateDerivative=zeros(Nt,Nr);
50 FlowEfficiency=zeros(Nt,Nr);
51 LineEfficiency=zeros(Nt,Nr);
52 EfficiencyOfMixing=zeros(Nt,Nr);
53 FirstInterfaceOrientationFactor=zeros(Nt,Nr);
54 SecondInterfaceOrientationFactor=zeros(Nt,Nr);
55 FirstVelocityOrientationFactor=zeros(Nt,Nr);
56 SecondVelocityOrientationFactor=zeros(Nt,Nr);
57 StreamlineCurvature=zeros(Nt,Nr);

```



```

58
59 for n=1:Nr
60
61 [ RunParameters,...
62   StreamFunctionPercentError(:,n),...
63   Time(:,n),...
64   CoordinateX(:,n),...
65   CoordinateY(:,n),...
66   MagnitudeVelocity(:,n),...
67   MagnitudeTwirl(:,n),...
68   MaterialStretch(:,n),...
69   SquareOrientationVelocity(:,n),...
70   SquareOrientationInteface(:,n),...
71   SquareOrientationEigenvector(:,n),...
72   NormalizedStretchingRate(:,n),...
73   MaximumNormalizedStretchingRate(:,n),...
74   MaximumNormalizedStretchingRateDerivative(:,n),...
75   FlowEfficiency(:,n),...
76   LineEfficiency(:,n),...
77   EfficiencyOfMixing(:,n),...
78   FirstInterfaceOrientationFactor(:,n),...
79   SecondInterfaceOrientationFactor(:,n),...
80   FirstVelocityOrientationFactor(:,n)...
81   SecondVelocityOrientationFactor(:,n),...
82   StreamlineCurvature(:,n)]=...
83   Flow3_CODE_Routine_2(y0(n));
84
85 end
86
87 dlmwrite('Flow3_DATA.RunParameters',...
88   RunParameters,'precision','%15.13f')
89 dlmwrite('Flow3_DATA.StreamFunctionPercentError',...
90   StreamFunctionPercentError,'precision','%15.13f')
91 dlmwrite('Flow3_DATA.Time',...
92   Time,'precision','%15.13f')
93 dlmwrite('Flow3_DATA.CoordinateX',...
94   CoordinateX,'precision','%15.13f')
95 dlmwrite('Flow3_DATA.CoordinateY',...
96   CoordinateY,'precision','%15.13f')
97 dlmwrite('Flow3_DATA.MagnitudeVelocity',...
98   MagnitudeVelocity,'precision','%15.13f')
99 dlmwrite('Flow3_DATA.MagnitudeTwirl',...
100   MagnitudeTwirl,'precision','%15.13f')
101 dlmwrite('Flow3_DATA.MaterialStretch',...
102   MaterialStretch,'precision','%15.13f')
103 dlmwrite('Flow3_DATA.SquareOrientationVelocity',...
104   SquareOrientationVelocity,'precision','%15.13f')
105 dlmwrite('Flow3_DATA.SquareOrientationInteface',...
106   SquareOrientationInteface,'precision','%15.13f')
107 dlmwrite('Flow3_DATA.SquareOrientationEigenvector',...
108   SquareOrientationEigenvector,'precision','%15.13f')
109 dlmwrite('Flow3_DATA.NormalizedStretchingRate',...
110   NormalizedStretchingRate,'precision','%15.13f')
111 dlmwrite('Flow3_DATA.MaximumNormalizedStretchingRate',...

```

```

112     MaximumNormalizedStretchingRate, 'precision', '%15.13f')
113 dlmwrite('Flow3_DATA.MaximumNormalizedStretchingRateDerivative',...
114     MaximumNormalizedStretchingRateDerivative, 'precision', '%15.13f')
115 dlmwrite('Flow3_DATA.FlowEfficiency',...
116     FlowEfficiency, 'precision', '%15.13f')
117 dlmwrite('Flow3_DATA.LineEfficiency',...
118     LineEfficiency, 'precision', '%15.13f')
119 dlmwrite('Flow3_DATA.EfficiencyOfMixing',...
120     EfficiencyOfMixing, 'precision', '%15.13f')
121 dlmwrite('Flow3_DATA.FirstInterfaceOrientationFactor',...
122     FirstInterfaceOrientationFactor, 'precision', '%15.13f')
123 dlmwrite('Flow3_DATA.SecondInterfaceOrientationFactor',...
124     SecondInterfaceOrientationFactor, 'precision', '%15.13f')
125 dlmwrite('Flow3_DATA.FirstVelocityOrientationFactor',...
126     FirstVelocityOrientationFactor, 'precision', '%15.13f')
127 dlmwrite('Flow3_DATA.SecondVelocityOrientationFactor',...
128     SecondVelocityOrientationFactor, 'precision', '%15.13f')
129 dlmwrite('Flow3_DATA.StreamlineCurvature',...
130     StreamlineCurvature, 'precision', '%15.13f')

```

C.3.2 Velocity Field Generation Module

```

1  %
2  %   Title:      New Measures for the Study of Distributive Mixing
3  %               in Continuous Creeping Flows
4  %
5  %   Author:     Jason Nixon
6  %
7  %   Code:       2D Steady State High Aspect Ratio Low Reynolds
8  %               Number Lid Driven Cavity Velocity Solution
9  %
10
11 clc; clear; close all;
12
13 % Cavity Geometry
14     Dx1=15;                % cavity length
15     Dx2=1;                % cavity height
16     U=1;                  % top-wall speed
17
18 % Fluid Material Properties
19     Re=0.1;                % reynolds number
20     rho=1000;              % density
21     mu=10000;              % dynamic viscosity
22
23 % Simulation Properties
24     sp=200;                % divisions per unit length
25     iter_run=65000;        % number of iterations
26     R=1;                   % under-relaxation parameter
27
28 % Simulation Parameters
29     nx=Dx1*sp+1;           % number of nodes in x1

```

```

30     ny=Dx2*sp+1;                               % number of nodes in x2
31     h=1/sp;                                     % mesh spacing
32     hs=h^2;                                    % square mesh spacing
33
34 % Zero Matrix Definitions
35     psi=zeros(ny,nx);
36     omega=zeros(ny,nx);
37     u1=zeros(ny,nx);
38     u2=zeros(ny,nx);
39
40 for iter=1:iter_run
41
42     %top and bottom boundary nodes
43     for i=2:(nx-1)
44         omega_node_b1=-2*psi(2,i)/hs;
45         omega(1,i)=omega(1,i)+R*(omega_node_b1-omega(1,i));
46         psi(1,i)=0;
47
48         omega_node_b3=-2*(psi(ny-1,i)+U*h)/hs;
49         omega(ny,i)=omega(ny,i)+R*(omega_node_b3-omega(ny,i));
50         psi(ny,i)=0;
51     end
52
53     %left and right boundary nodes
54     for j=2:(ny-1)
55         omega_node_b2=-2*psi(j,2)/hs;
56         omega(j,1)=omega(j,1)+R*(omega_node_b2-omega(j,1));
57         psi(j,1)=0;
58
59         omega_node_b4=-2*psi(j,nx-1)/hs;
60         omega(j,nx)=omega(j,nx)+R*(omega_node_b4-omega(j,nx));
61         psi(j,nx)=0;
62     end
63
64     %internal Nodes
65     for i=2:(nx-1)
66
67         for j=2:(ny-1)
68
69             A=omega(j,i-1);
70             B=omega(j-1,i);
71             C=omega(j,i);
72             D=omega(j+1,i);
73             E=omega(j,i+1);
74             F=psi(j,i-1);
75             G=psi(j-1,i);
76             H=psi(j,i);
77             I=psi(j+1,i);
78             J=psi(j,i+1);
79
80             %calculates the current-step nodal vorticity value
81             omega_node_i=(A+B+D+E+Re*( (F-J)*(B-D)-(G-I)*(A-E) )/4)/4;
82
83             %applies the vorticity value relaxation scheme

```

```

84         omega(i,j)=C+R*(omega_node_i-C);
85
86         %calculates the current-step nodal stream value
87         psi_node_i=(F+G+I+J+hs*C)/4;
88
89         %applies stream value relaxation scheme
90         psi(j,i)=H+R*(psi_node_i-H);
91     end
92
93 end
94
95 end
96
97 % Assigns the top boundary velocity value
98 u1(ny,1:nx)=1;
99
100 % Calculates the interior nodal velocity values
101 for i=2:(nx-1)
102     for j=2:(ny-1)
103         F=psi(j,i-1);
104         G=psi(j-1,i);
105         I=psi(j+1,i);
106         J=psi(j,i+1);
107         u1(j,i)=(I-G)/(2*h);
108         u2(j,i)=-(J-F)/(2*h);
109     end
110 end
111
112 dlmwrite('Flow3_DATA.FlowfieldParameters',...
113         [Dx1 Dx2 U sp Re rho mu], 'precision', '%8.6f')
114 dlmwrite('Flow3_DATA.StreamFunction',...
115         psi, 'precision', '%8.6f')
116 dlmwrite('Flow3_DATA.Vorticity',...
117         omega, 'precision', '%8.6f')
118 dlmwrite('Flow3_DATA.VelocityX',...
119         u1, 'precision', '%8.6f')
120 dlmwrite('Flow3_DATA.VelocityY',...
121         u2, 'precision', '%8.6f')

```

C.3.3 Material Tracking Module

```

1 function [paraRUN, SFPE, Time, X, Y, MagnitudeVelocity, ...
2         MagnitudeTwirl, ds, SOU, SOI, SOD, NSR, MNSR, MNSRD, eF, eL, eM...
3         IOF1, IOF2, UOF1, UOF2, K] = Flow3_CODE_Routine_2(y0)
4
5 global FDPParam PSI Ux Uy x0 tmax dt orient0
6
7 PaCL=FDPParam(1); % specifies cavity length
8 PaCH=FDPParam(2); % specifies cavity height
9 PaU=FDPParam(3); % specifies Wall speed
10 PaSP=FDPParam(4); % specifies node spacing parameter

```

```

11 PaRN=FDParam(5); % specifies Reynold number
12 PaD=FDParam(6); % specifies fluid density
13 PaV=FDParam(7); % specifies fluid viscosity
14
15 paraRUN=[PaCL PaCH PaU PaSP PaD PaV PaRN x0 y0 tmax dt];
16
17 nx=PaCL*PaSP+1;
18 ny=PaCH*PaSP+1;
19
20 [dU_dx, dU_dy]=gradient(Ux,1/PaSP);
21 [dV_dx, dV_dy]=gradient(Uy,1/PaSP);
22
23 D11f=dU_dx;
24 D12f=0.5*(dU_dy+dV_dx);
25 D21f=0.5*(dV_dx+dU_dy);
26 D22f=dV_dy;
27
28 [dD11f_dx, dD11f_dy]=gradient(D11f,1/PaSP);
29 [dD12f_dx, dD12f_dy]=gradient(D12f,1/PaSP);
30 [dD21f_dx, dD21f_dy]=gradient(D21f,1/PaSP);
31 [dD22f_dx, dD22f_dy]=gradient(D22f,1/PaSP);
32
33 X(2:tmax/dt+1)=0;
34 Y(2:tmax/dt+1)=0;
35 PSIC(tmax/dt+1)=0;
36 SFPE(tmax/dt+1)=0;
37 MagnitudeVelocity(tmax/dt+1)=0;
38 dx=zeros(2,tmax/dt+1);
39 ds(tmax/dt+1)=0;
40 NSR(tmax/dt+1)=0;
41 MNSR(tmax/dt+1)=0;
42 MNSRD(tmax/dt+1)=0;
43 SOU(tmax/dt+1)=0;
44 SOD(tmax/dt+1)=0;
45 SOI(tmax/dt+1)=0;
46 eM(tmax/dt+1)=0;
47 eF(tmax/dt+1)=0;
48 eL(tmax/dt+1)=0;
49 MagnitudeTwirl(tmax/dt+1)=0;
50 MagnitudeVorticity(tmax/dt+1)=0;
51 IOF1(tmax/dt+1)=0;
52 IOF2(tmax/dt+1)=0;
53 UOF1(tmax/dt+1)=0;
54 UOF2(tmax/dt+1)=0;
55
56 dx(:,1)=orient0;
57
58 X(1)=x0;
59
60 Y(1)=y0;
61
62 Xn=X(1)*(nx-1)/PaCL+1;
63
64 Yn=Y(1)*(ny-1)/PaCH+1;

```

```

65
66 % Defines the velocity gradient components
67 L11=interp2 (dU_dx,Xn,Yn, 'Spline');
68 L12=interp2 (dU_dy,Xn,Yn, 'Spline');
69 L21=interp2 (dV_dx,Xn,Yn, 'Spline');
70 L22=interp2 (dV_dy,Xn,Yn, 'Spline');
71
72 L=[ L11 L12 ; L21 L22 ];
73
74 D=(L+L')/2;
75
76 W=(L-L')/2;
77
78 MNSR(1)=sqrt (sum (sum (D.*D))/2);
79
80 vecU=[interp2 (Ux,Xn,Yn) interp2 (Uy,Xn,Yn)];
81
82 MagnitudeVelocity(1)=sqrt (dot (vecU(:,1),vecU(:,1)));
83
84 ds(1)=sqrt (dot (dx(:,1),dx(:,1)));
85
86 p=dx(:,1)/ds(1);
87
88 MNSR(1)=sqrt (sum (sum (D.*D))/2);
89
90 NSR(1)=0;
91
92 eM(1)=NSR(1)/sqrt (sum (sum (D.*D)));
93
94 eL(1)=NSR(1)/MNSR(1);
95
96 eF(1)=eM(1)/eL(1);
97
98 [n, n, d1]=PD2v2 (D);
99
100 PSIr=interp2 (PSI,Xn,Yn);
101
102 PSIC(1)=interp2 (PSI,Xn,Yn);
103
104 SFPE(1)=abs (2*(PSIr-PSIC(1))/(PSIr+PSIC(1)))*100;
105
106 u=vecU'/sqrt (dot (vecU,vecU));
107
108 IOF1(1)=dot (p,d1);
109
110 IOF2(1)=d1'* (D+W-(p'*D*p)*eye (2)-zeros (2))*p;
111
112 UOF1(1)=dot (u,d1);
113
114 UOF2(1)=d1'* (D+W-(u'*D*u)*eye (2)-zeros (2))*u;
115
116 for n=2:tmax/dt+1
117
118

```

```

119     [ X(n),Y(n) ] = Flow3_CODE_Routine_3(X(n-1),Y(n-1));
120
121     Xn=X(n) * (nx-1)/PaCL+1;
122
123     Yn=Y(n) * (ny-1)/PaCH+1;
124
125     PSIC(n)=interp2(PSI,Xn,Yn);
126
127     SFPE(n)=abs(2*(PSIr-PSIC(n))/(PSIr+PSIC(n)))*100;
128
129     vecU=[interp2(Ux,Xn,Yn) interp2(Uy,Xn,Yn)];
130
131     [MagnitudeVelocity(n),~,~,SOU(n)]=vec_prop(vecU,[1;0]);
132
133     Lp=L;
134
135     L11=interp2(dU_dx,Xn,Yn,'Spline');
136
137     L12=interp2(dU_dy,Xn,Yn,'Spline');
138
139     L21=interp2(dV_dx,Xn,Yn,'Spline');
140
141     L22=interp2(dV_dy,Xn,Yn,'Spline');
142
143     L=[ L11 L12 ; L21 L22 ]; %defines the 2D velocity ...
        gradient tensor
144
145     D=(L+L')/2; %defines the rate of deformation tensor
146
147     W=(L-L')/2; %defines the spin tensor
148
149     %defines the D gradient components in each axis
150     dD11_dx=interp2(dD11f_dx,Xn,Yn,'Spline');
151     dD11_dy=interp2(dD11f_dy,Xn,Yn,'Spline');
152     dD12_dx=interp2(dD12f_dx,Xn,Yn,'Spline');
153     dD12_dy=interp2(dD12f_dy,Xn,Yn,'Spline');
154     dD21_dx=interp2(dD21f_dx,Xn,Yn,'Spline');
155     dD21_dy=interp2(dD21f_dy,Xn,Yn,'Spline');
156     dD22_dx=interp2(dD22f_dx,Xn,Yn,'Spline');
157     dD22_dy=interp2(dD22f_dy,Xn,Yn,'Spline');
158
159     %defines the each element of the D_dot array
160     D_dot_11=vecU(1)*dD11_dx+vecU(2)*dD11_dy;
161     D_dot_12=vecU(1)*dD12_dx+vecU(2)*dD12_dy;
162     D_dot_21=vecU(1)*dD21_dx+vecU(2)*dD21_dy;
163     D_dot_22=vecU(1)*dD22_dx+vecU(2)*dD22_dy;
164
165     %assembles the D_dot tensor
166     D_dot=[D_dot_11 D_dot_12 ; D_dot_21 D_dot_22];
167
168     TW=(D_dot*D-D*D_dot)/(2*sum(sum(D.*D)));
169
170     dx(:,n)=dt*(L+Lp)/2*dx(:,n-1)+dx(:,n-1);
171

```

```

172     [ds(n), p, r, SOI(n)] = vec_prop(dx(:, n), [1; 0]);
173
174     [r, r, dl] = PD2v2(D);
175
176     [r, r, r, SOD(n)] = vec_prop(dl, [1; 0]);
177
178     MNSR(n) = sqrt(sum(sum(D.*D))/2);
179
180     MNSRD(n) = sum(sum(D.*D_dot))/(2*MNSR(n));
181
182     NSR(n) = 2*(ds(n)-ds(n-1))/((ds(n)+ds(n-1))*dt);
183
184     MagnitudeTwirl(n) = sum(sum([0 -0.5 ; 0.5 0].*TW));
185
186     MagnitudeVorticity(n) = sum(sum([0 -0.5 ; 0.5 0].*W));
187
188     eM(n) = NSR(n)/sqrt(sum(sum(D.*D)));
189
190     eL(n) = NSR(n)/MNSR(n);
191
192     eF(n) = eM(n)/eL(n);
193
194     u = vecU'/sqrt(dot(vecU, vecU));
195
196     IOF1(n) = dot(p, dl);
197
198     IOF2(n) = dl'*(D+W-(p'*D*p)*eye(2)-TW)*p;
199
200     UOF1(n) = dot(u, dl);
201
202     UOF2(n) = dl'*(D+W-(u'*D*u)*eye(2)-TW)*u;
203
204     end
205
206     Time = linspace(0, tmax, tmax/dt+1);
207
208     K = Flow3_CODE_Routine_4(X, Y);
209
210     end

```

C.3.4 Runge-Kutta Module

```

1 function [ Xp , Yp ] = Flow3_CODE_Routine_3( X , Y )
2
3     global Ux Uy dt FDPParam
4
5     S = FDPParam(4);
6
7     K1 = interp2(Ux, X*S+1, Y*S+1);
8
9     J1 = interp2(Uy, X*S+1, Y*S+1);

```



```

10
11     K2=interp2(Ux, (X+0.5*dt*K1)*S+1, (Y+0.5*dt*J1)*S+1);
12
13     J2=interp2(Uy, (X+0.5*dt*K1)*S+1, (Y+0.5*dt*J1)*S+1);
14
15     K3=interp2(Ux, (X+0.5*dt*K2)*S+1, (Y+0.5*dt*J2)*S+1);
16
17     J3=interp2(Uy, (X+0.5*dt*K2)*S+1, (Y+0.5*dt*J2)*S+1);
18
19     K4=interp2(Ux, (X+dt*K3)*S+1, (Y+dt*J3)*S+1);
20
21     J4=interp2(Uy, (X+dt*K3)*S+1, (Y+dt*J3)*S+1);
22
23     Xp=X+dt*(K1+2*K2+2*K3+K4)/6;
24
25     Yp=Y+dt*(J1+2*J2+2*J3+J4)/6;
26
27 end

```

C.3.5 Streamline Curvature Module

```

1 function [ K ] = Flow3_CODE_Routine_4(X,Y)
2
3     global dt tmax
4
5     K=zeros(size(X));
6
7     A=gradient(X,dt);
8
9     B=gradient(Y,dt);
10
11     C=gradient(A,dt);
12
13     D=gradient(B,dt);
14
15     for j=1:tmax/dt+1
16
17         K(j)=abs(A(j)*D(j)-B(j)*C(j))/((A(j)^2+B(j)^2)^(3/2));
18
19     end
20
21 end

```

References

- [1] H. Aref. Stirring by chaotic advection. *Journal of Fluid Mechanics*, 143:1–21, 1984.
- [2] G. K. Batchelor. *An Introduction to Fluid Dynamics*. Cambridge University Press, 2000.
- [3] A. Brothman, G. N. Wollan, and S. M. Feldman. New analysis provides formula to solve mixing problems. *Chemical and Metal Engineering*, 52:102–106, 1945.
- [4] R. Chella and J. M. Ottino. Fluid mechanics of mixing in a single screw extruder. *Industrial Engineering and Chemistry Fundamentals*, 24(2):170–180, 1985.
- [5] R. Chella and J. M. Ottino. Stretching in some classes of fluid motions and asymptotic mixing efficiencies as a measure of flow classification. *Archive for Rational Mechanics and Analysis*, 90(1):15–42, 1985.
- [6] W. L. Chien, H. Rising, and J. M. Ottino. Laminar mixing and chaotic mixing in several cavity flows. *Journal of Fluid Mechanics*, 170:355–377, 1986.
- [7] P. V. Danckwerts. The definition and measurement of some characteristics of mixtures. *Applied Scientific Research, Section A*, 3(4):279–296, 1952.
- [8] L. Erwin. Theory of laminar mixing. *Polymer Engineering and Science*, 18(13):1044–1048, 1978.
- [9] L. Erwin. Theory of mixing sections in single screw extruders. *Polymer Engineering and Science*, 18(7):572–576, 1978.
- [10] L. Erwin. An upper bound on the performance of a plane strain mixer. *Polymer Engineering and Science*, 18(9):738–740, 1978.
- [11] L. Erwin and K. Y. Ng. Illustrations of mixing in laminar flow. Technical report, University of Wisconsin Madison, 1979.
- [12] Z. Guo. Spin and rotation velocity of the stretching frame continuum. *Applied Mathematics and Mechanics*, 9(12):1109–1112, 1988.
- [13] Z. Guo and H. Liang. Absolute representation of spins of principal frames in a continuum. *Applied Mathematics and Mechanics*, 12(1):41–47, 1991.
- [14] G. A. Holzapfel. *Nonlinear Solid Mechanics: A Continuum Approach for Engineering*. John Wiley and Sons LTD, 1 edition, 2000.
- [15] C. W. Leong and J. M. Ottino. Experiments on mixing due to chaotic advection in a cavity. *Journal of Fluid Mechanics*, 209:463–499, 1989.
- [16] L. E. Malvern. *Introduction to the Mechanics of a Continuous Media*. Prentice Hall, 1 edition, 1969.

- [17] Ica Manas-Zloczower. *Mixing and Compounding of Polymers*. Hanser, 2009.
- [18] W. D. Mohr, R. L. Saxton, and C. H. Jepson. Mixing in laminar-flow systems. *Industrial Engineering and Chemistry Fundamentals*, 49(11):1855–1856, 1957.
- [19] W. D. Mohr, R. L. Saxton, and C. H. Jepson. Theory of mixing in the single-screw extruder. *Industrial Engineering and Chemistry Fundamentals*, 49(11):1857–1862, 1957.
- [20] J. M. Ottino. Scientific american. *The Mixing of Fluids*, 260:56–67, 1989.
- [21] J. M. Ottino. Mixing, chaotic advection, and turbulence. *Annual Review of Fluid Mechanics*, 22(207-253), 1990.
- [22] J. M. Ottino and R. Chella. Laminar mixing in polymeric liquids - a brief reivew and recent theoretical developments. *Polymer Engineering and Science*, 23(7):357–379, 1983.
- [23] J. M. Ottino, W. E. Ranz, and C. W. Macosko. A lamellar model for analysis of liquid-liquid mixing. *Chemical Engineering and Science*, 34(6):877–890, 1979.
- [24] J. M. Ottino, W. E. Ranz, and C. W. Macosko. A framework for description of mechanical mixing of fluids. *American Institute of Chemical Engineers Journal*, 27(4):565–577, 1981.
- [25] R. L. Panton. *Incompressible Flow*. John Wiley and Sons LTD, 3 edition, 2005.
- [26] P. N. Shankar and M. D. Deshpande. Fluid mechanics in the driven cavity. *Annual Review of Fluid Mechanics*, 32:93–136, 2000.
- [27] R. S. Spencer and R. M. Wiley. The mixing of very viscous liquids. *Journal of Colloid Science*, 6(2):133–145, 1951.
- [28] Z. Tadmor and C. G. Gogos. *Principles of Polymer Mixing*. Wiley-Interscience, 2nd edition, 2006.
- [29] Epameinondas Trivilos. Performance and flow regimes in plane 2-d diffusers with exit channels at low reynolds numbers. Master’s thesis, Naval Postgraduate School, 2003.
- [30] M. Vincent and J. F. Aggasant. Experimental and theoretic study of short-fibre orientation in diverging flows. *Rheological Acta*, 24(6):603–610, 1985.